

LEVEL

12

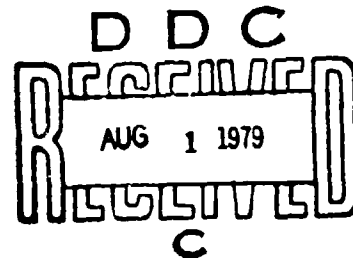
AFML-TR-79-4042

ADA072121

DETERMINATION OF CONSTITUTIVE EQUATIONS FOR HIGH STRENGTH ALUMINUM AND TITANIUM ALLOYS APPLICABLE TO SHEET METAL FORMABILITY

JOSEPH F. THOMAS, JR.

Department of Engineering
Wright State University
Dayton, Ohio 45435



April 1979

TECHNICAL REPORT AFML-TR-79-4042
Final Technical Report for the
Period 23 Sept. 1977 - 23 Sept. 1978

DDC FILE COPY

Prepared for ONRRR
The Ohio State University
Research Center
1314 Kinnear Road
Columbus, Ohio 43212

Approved for public release; distribution unlimited

AIR FORCE MATERIALS LABORATORY
AIR FORCE WRIGHT AERONAUTICAL LABORATORIES
AIR FORCE SYSTEM COMMAND
WRIGHT-PATTERSON AIR FORCE BASE, OHIO 45433

79 07 30 005

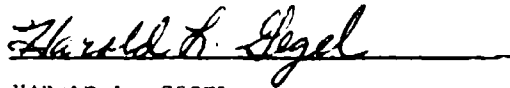
**Best
Available
Copy**

NOTICE

When Government drawings, specifications, or other data are used for any purpose other than in connection with a definitely related Government procurement operation, the United States Government thereby incurs no responsibility nor any obligation whatsoever; and the fact that the government may have formulated, furnished, or in any way supplied the said drawings, specifications, or other data, is not to be regarded by implication or otherwise as in any manner licensing the holder or any other person or corporation, or conveying any rights or permission to manufacture, use, or sell any patented invention that may in any way be related thereto.

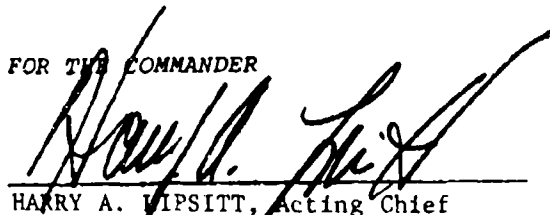
This report has been reviewed by the Information Office (OI) and is releasable to the National Technical Information Service (NTIS). At NTIS, it will be available to the general public, including foreign nations.

This technical report has been reviewed and is approved for publication.



HAROLD L. GEDEL
PROJECT ENGINEER

FOR THE COMMANDER



HARRY A. MIPSITT, Acting Chief
Processing and High Temperature Materials Branch
Metals and Ceramics Division

"If your address has changed, if you wish to be removed from our mailing list, or if the addressee is no longer employed by your organization please notify AFML/LLM, W-PAFB, OH 45433 to help us maintain a current mailing list".

Copies of this report should not be returned unless return is required by security considerations, contractual obligations, or notice on a specific document.

SECURITY CLASSIFICATION OF THIS PAGE (When Data Entered)

REPORT DOCUMENTATION PAGE		READ INSTRUCTIONS BEFORE COMPLETING FORM
1. REPORT NUMBER AFML-TR-79-4042	2. GOVT ACCESSION NO.	3. REPORTING CATALOG NUMBER
4. TITLE (and Subtitle) DETERMINATION OF CONSTITUTIVE EQUATIONS FOR HIGH STRENGTH ALUMINUM AND TITANIUM ALLOYS APPLICABLE TO SHEET METAL FORMABILITY.	5. TYPE OF REPORT & PERIOD COVERED Final Technical Report 23 Sep 77 - 23 Sep 78	
6. AUTHOR(s) Joseph F. Thomas, Jr.	7. CONTRACT OR GRANT NUMBER(s) F33615-77-C-5260	
8. PERFORMING ORGANIZATION NAME AND ADDRESS Wright State University Department of Engineering Dayton, Ohio 45435	9. PROGRAM ELEMENT, PROJECT, TASK AREA & WORK UNIT NUMBERS 2306P704	
10. CONTROLLING OFFICE NAME AND ADDRESS Air Force Materials Laboratory (LL) Wright Patterson AFB, Ohio 45433	11. REPORT DATE Apr 1979	
12. MONITORING AGENCY NAME & ADDRESS (if different from Controlling Office) ONRRR, The Ohio State University Research Center 1314 Kinnear Road, Columbus, Ohio 43212	13. NUMBER OF PAGES 1	
14. DISTRIBUTION STATEMENT (of this Report) Approved for public release; distribution unlimited		15. SECURITY CLASS. (of this report) Unclassified
16. DECLASSIFICATION/DOWNGRADING SCHEDULE		
17. DISTRIBUTION STATEMENT (of the abstract entered in Block 20, if different from Report)		
18. SUPPLEMENTARY NOTES		
19. KEY WORDS (Continue on reverse side if necessary and identify by block number) Sheet Metal Forming Aluminum Alloys Formability Titanium Alloys Forming Limit Curve Strain Hardening Constitutive Relation Strain Rate Sensitivity		
20. ABSTRACT (Continue on reverse side if necessary and identify by block number) The formability of sheet metal can be investigated by the calculation of a forming limit curve (FLC) which gives the locus of principal strains beyond which failure is expected. For failure by plastic instability, the FLC depends upon material formability indices including the strain hardening coefficient and strain rate sensitivity. If a yield surface can be assumed, the material parameters needed to calculate the FLC can be obtained from uniaxial tensile data. This approach has been adopted to investigate the		

formability of certain high strength aerospace sheet alloys.

Constant extension rate tests vs. strain rate and temperature and load relaxation tests vs. temperature have been performed on 2024-0 aluminum sheet and annealed Ti-6Al-4V sheet and round bar tensile specimens. Load-elongation and load-time data were recorded digitally for direct determination of characteristic derivative plots such as $d\sigma/d\epsilon$ (γ) vs. σ and σ vs. $\dot{\epsilon}$ where σ , ϵ , and $\dot{\epsilon}$ are the stress, non-elastic strain and strain rate respectively. Thus the strain hardening coefficient and strain rate sensitivity are obtained as functions of stress, strain rate, and temperature. The plastic anisotropy of the sheet materials has also been investigated.

FLC's can be calculated from constitutive equation parameters determined directly from the derivative plots. From the dependence $\gamma(\sigma)$, it was found that the Swift equation models the strain hardening behavior exactly at high strains ($\epsilon \geq 0.05$ for 2024-0 Al; $\epsilon \geq 0.02$ for Ti-6Al-4V). At 25°C, the strain rate dependence $\sigma(\dot{\epsilon})$ could be modelled by an equation suggested by Hart for low homologous temperatures. For 2024-0 Al at 25°C, the strain rate sensitivity was small enough to be neglected.

For 2024-0 aluminum at 25°C, the FLC calculated from Hill's theory of localized necking (strain-rate independent) was in good agreement with an experimental in-plane forming limit diagram (FLD). However, both the calculated FLC and in-plane FLD were significantly lower than the standard out-of-plane FLD determined from punch-stretch tests. For 2024-0 aluminum at 163°C (325°F) and Ti-6Al-4V, an FLC based on a strain-rate dependent model will be required for comparison to experimental limit strains.

FOREWORD

This report is submitted by Wright State University. It is the final technical report for Contract F33615-77-C-5260. The principal investigator was Joseph F. Thomas, Jr., Associate Professor in the Departments of Physics and Engineering. The project engineer for the Air Force Materials Laboratory was Harold L. Gegel, Senior Scientist, LLM.

Other individuals supported by this contract were P. Jeffrey Moore, a graduate student in the Department of Physics and Stephen T. Leffler and Devert W. Wicker, undergraduate students. The author is pleased to acknowledge thier contributions to this project.

The author would also like to acknowledge the support of AFOSR through grant no. 77-3252 (AFOSR/ASEE Minigrant Program) which supported the initiation of the work performed for this contract.

The work on this contract was coordinated with Contract F33615-77-C-5059 conducted by Battelle Columbus Laboratories and subcontractors. The author acknowledges the cooperative efforts of T. Altan and V. Nagpal (Battelle), B. Shabel (ALCOA), and H. Conrad (University of Kentucky).

Accession For	
NTIS GRA&I	<input checked="checked" type="checkbox"/>
DDC TAB	<input type="checkbox"/>
Unannounced	<input type="checkbox"/>
Justification	
By	
Distribution/	
Availability Codes	
Dist	Avail and/or special
A	

79 07 30 005

TABLE OF CONTENTS

	<u>Page</u>
1. INTRODUCTION	1
1.1 Sheet Metal Formability	1
1.2 Formability Indices	1
1.3 Scope of the Program	2
1.4 Relation to Other Air Force Programs	3
2. CONSTITUTIVE RELATIONS	5
2.1 Strain Hardening Relationships	5
2.2 Hart's Phenomenological Approach	6
3. FORMING LIMITS	8
3.1 Experimental Forming Limit Diagrams	8
3.2 Theoretical Forming Limit Curves	9
4. EXPERIMENTAL TEST PROGRAM	12
4.1 Materials and Test Specimens	12
4.2 Tensile Test Procedures	14
4.3 Automatic Data Acquisition System	15
5. RESULTS FOR 2024-O ALUMINUM	20
5.1 Constant Extension Rate Tests	20
5.2 Load Relaxation Tests	37
6. RESULTS FOR Ti-6Al-4V	45
6.1 Constant Extension Rate Tests	45
6.2 Load Relaxation Tests	62
7. COMPARISON OF THEORETICAL AND EXPERIMENTAL FORMING LIMITS	69
8. CONCLUSIONS	74
9. REFERENCES	76
10. APPENDIX A. SUMMARY OF SOME ANISOTROPIC PLASTICITY RELATIONSHIPS . .	80
11. APPENDIX B. AUTOMATIC DATA ACQUISITION SYSTEM CONTROL PROGRAMS . . .	84

LIST OF ILLUSTRATIONS

<u>Figure</u>		<u>Page</u>
1.	Pin-Loaded Sheet Tensile Specimen	13
2.	Block Diagram of the Automatic Data Acquisition System	16
3.	Flow Chart for the Automatic Data Acquisition System Program DVM RUN	18
4.	Flow Chart for the Automatic Data Acquisition System Program DVM DATA	19
5.	Load vs. Elongation and Change in Thickness vs. Elongation for 2024-0 Aluminum at 25°C and 10^{-3} sec^{-1}	21
6.	Tensile True Stress - True Strain Curves for 2024-0 Aluminum at 163°C vs. Strain Rate	25
7.	Tensile True Stress - True Strain Curves for 2024-0 Aluminum at 10^{-2} sec^{-1} vs. Temperature	26
8.	Strain Hardening Behavior Presented as γ vs. Effective Stress $\bar{\sigma}$ for 2024-0 Aluminum at 163°C and 10^{-3} sec^{-1}	31
9.	Strain Hardening Behavior Presented as Log γ vs. Log $\bar{\sigma}$ for 2024-0 Aluminum at 163°C and 10^{-3} sec^{-1}	32
10.	Effective Stress - Strain Curve with Swift Equation Fit for 2024-0 Aluminum at 163°C and 10^{-3} sec^{-1} . . .	34
11.	Strain Hardening Behavior vs. Strain Rate for 2024-0 Aluminum at 163°C. Curves are for (L to R) 10^{-5} , 10^{-4} , 10^{-3} , 10^{-2} sec^{-1}	36
12.	Comparison of an Extrapolated Tensile Effective Stress-Strain Curve with Bulge Test Data for 2024-0 Aluminum at 25°C	38

<u>Figure</u>		<u>Page</u>
13.	Comparison of Extrapolated Tensile Strain Hardening Behavior with the Bulge Test for 2024-0 Aluminum at 25°C	39
14.	Stress Relaxation Hardness Curve $\log \sigma$ vs. $\log \dot{\epsilon}$ for 2024-0 Aluminum at 25°C	41
15.	Stress Relaxation Hardness Curves vs. Temperature for 2024-0 Aluminum	42
16.	Stress Relaxation Hardness Curve for 2024-0 Aluminum at 163°C	44
17.	Load vs. Elongation and Change in Thickness vs. Elongation for Ti-6Al-4V Sheet at 25°C and 10^{-3} sec^{-1}	46
18.	Tensile True Stress - True Strain Curves for Ti-6Al-4V Sheet at 25°C vs. Strain Rate	47
19.	True Stress - True Strain Curves for Ti-6Al-4V Sheet vs. Temperature at 10^{-2} sec^{-1} . From [4] . . .	49
20.	True Stress - True Strain Curves for Ti-6Al-4V Sheet vs. Temperature at 10^0 and 10^{-4} sec^{-1} . From [4] . .	50
21.	Load vs. Elongation for Ti-6Al-4V Bar at 25°C and 10^{-2} sec^{-1}	52
22.	Tensile True Stress - True Strain Curves for Ti-6Al-4V Bar at 10^{-2} sec^{-1} vs. Temperature	53
23.	Strain Hardening Behavior Presented as $\log \gamma$ vs. $\log \sigma$ for Ti-6Al-4V Bar at 25°C and 10^{-2} sec^{-1}	56
24.	True Stress - True Strain Curve with Swift Equation Fit for Ti-6Al-4V Bar at 25°C and 10^{-2} sec^{-1}	57

<u>Figure</u>		<u>Page</u>
25.	Strain Hardening Behavior Presented as Log γ vs. Log σ for Ti-6Al-4V Bar at 500°C and 10^{-2} sec^{-1}	59
26.	Strain Hardening Behavior Presented as Log γ vs. Log σ for Ti-6Al-4V Sheet at 25°C and 10^{-4} sec^{-1}	60
27.	True Stress - True Strain Curve with Swift Equation Fit for Ti-6Al-4V Sheet at 25°C and 10^{-4} sec^{-1} . . .	61
28.	Stress-Relaxation Hardness Curves vs. Temperature (25°C - 500°C) for Ti-6Al-4V Bar	63
29.	Stress-Relaxation Hardness Curves vs. Temperature (200°C - 425°C) for Ti-6Al-4V Bar	64
30.	Stress-Relaxation Hardness Curves with Hart's Low Temperature Equation Fit for Ti-6Al-4V Bar at 25°C .	66
31.	Stress-Relaxation Hardness Curve with Hart's Low Temperature Equation Fit and Comparison to Rate Dependent Yield Stresses for Ti-6Al-4V Sheet at 25°C	67
32.	In-Plane and Out-of-Plane FLD's for 2024-0 Aluminum at 25°C — Reynolds Lot. - - - - ALCOA lot. From [4]	70
33.	Theoretical Hill FLC for 2024-0 Aluminum at 25°C with Comparison to Experimental FLD's	71
34.	Experimental FLD's for Ti-6Al-4V at 24°C, 538°C, and 677°C. From [4]	73

LIST OF TABLES

<u>Tables</u>	<u>Page</u>
1. Tensile Test Parameters for 2024-0 Aluminum at 25°C	22
2. Tensile Test Parameters for 2024-0 Aluminum at 163°C.	23
3. Tensile Test Parameters for 2024-0 Aluminum at 10^{-2} sec $^{-1}$	24
4. R-Values for 2024-0 Aluminum at 25°C	27
5. Effective Stress - Effective Strain Conversion Factors at 25°C	28
6. Effective Stress vs. Effective Strain for 2024-0 Aluminum Tensile and Bulge Tests at 25°C.	29
7. Swift Equation Parameters for 2024-0 Aluminum at 25°C	33
8. Swift Equation Parameters for 2024-0 Aluminum at 163°C.	35
9. Tensile Test Parameters for Ti-6Al-4V Sheet at 25°C	48
10. Tensile Test Parameters for Ti-6Al-4V Bar at 10^{-2} sec $^{-1}$	51
11. R-Values for Ti-6Al-4V Sheet at Room Temperature. From [4].	54
12. Swift Equation Parameters for Ti-6Al-4V Sheet at 25°C	62
13. Hardness Curve Parameters for Ti-6Al-4V at 25°C . . .	65

I. INTRODUCTION

1.1 Sheet Metal Formability

The formability of sheet metal is dependent upon certain plastic properties of the material identified as formability indices. These indices affect formability in two distinct ways. On one hand, they determine the limiting states of strain which a sheet can provide in a forming process without an intervening failure. In addition, they affect the way strain is distributed in a sheet during forming and, hence, partially determine the maximum strains that will be imposed. Hence, it is necessary to identify and determine these formability indices for input to both formability and process models.

Several material properties are widely accepted as important sheet formability indices. These include the strain hardening coefficient and strain rate sensitivity. It is less widely recognized that these indices can show a significant dependence on strain-rate, temperature, and some measure of plastic hardness due to prestrain. It follows that, in order to include these parameters into analytical formability or process models, it is important to have an analytical material model or constitutive equation which can be used to express these dependencies.

Recently, Thomas, Geggel, and Teutonico [1] presented a systematic approach to assessing sheet metal formability based upon analytical material constitutive equations and calculated forming limit curves. The forming limit curve (FLC), which gives the locus of principal strains beyond which failure is expected, is based on a specific failure mode and corresponding set of material properties. The constitutive equation is used to input these properties, including their dependence on strain, strain-rate, and temperature, into the FLC analysis. When combined with numerical sheet metal process simulation models, an integrated CAD/CAM program for sheet metal forming can be developed.

1.2 Formability Indices

It is usually assumed that the most important failure criteria for sheet forming are related to plastic instability since plastic instability

usually precedes fracture. In this case the relevant sheet metal formability indices can be taken to be

- (1) The strain hardening coefficient $\gamma = (\partial \ln \sigma / \partial \epsilon)_{\dot{\epsilon}}$ where σ is the flow stress, ϵ is the non-elastic strain, and $\dot{\epsilon}$ is the non-elastic strain rate,
- (2) The strain rate sensitivity $\nu = (\partial \ln \sigma / \partial \ln \dot{\epsilon})_{\epsilon}$,
- (3) One or more history dependent parameters describing plastic hardness which evolve during deformation and which also partially determine γ and ν , and
- (4) Parameters needed to describe plastic anisotropy of the candidate sheet material.

The functional dependences of the indices (1) and (2) on stress σ and strain rate $\dot{\epsilon}$ and the index list (3) will depend on the form of the constitutive equation.

The indices (4) describing plastic anisotropy are taken to be the plastic strain ratios r_0 , r_{90} , and r_{45} measured on tensile specimens cut from the sheet at 0° , 90° , and 45° to the rolling direction respectively. In formability calculations which depend on normal anisotropy only [1], an effective $\bar{r} = 1/4 (r_0 + r_{90} + 2r_{45})$ is used. In calculations which account for planar anisotropy [2], the yield function depends explicitly on all three measured strain ratios.

1.3 Scope of the Program

The objective of this program has been to determine and experimentally verify material analytical models or constitutive relations applicable to the formability and processing of high strength aluminum and titanium alloy sheet materials. The constitutive relations will be used in related Air Force programs on modeling sheet formability and sheet forming processes.

The candidate materials selected for the test program were 2024-0 aluminum and the titanium alloy Ti-6Al-4V. The 2024 aluminum is usually formed in the "O" or soft temper and then heat treated to high strength. Ti-6Al-4V is the most widely used titanium alloy for aircraft structural parts.

The experimental test program has been restricted to uniaxial tensile tests. These include both constant extension rate tests used to determine strain hardening behavior and load relaxation tests used to determine strain rate sensitivity. The tests have been conducted on commercial sheet materials at temperatures representative of typical forming operations. The plastic anisotropy of the sheet has been considered. A digital data acquisition system has been developed. Data in digital form is required for accurate determination of required derivatives and for convenient mathematical modeling.

The uniaxial tensile test configuration has been selected because it provides a uniform stress state and is widely used. The advantages of being able to characterize the formability of a sheet material in terms of a few simple tensile tests is obvious. However, several potential limitations of the tensile test are widely recognized. These include (1) limited strain range due to necking instabilities, (2) limited strain rate range below most forming rates, and (3) lack of information on stress state dependence. In general, these limitations have not had a negative impact on the testing program, and this is discussed in detail where appropriate in the report. In regard to (3) above, it has been possible to compare the uniaxial test results with some biaxial tests obtained in related programs.

The constitutive relations determined can be used to calculate theoretical forming limit curves (FLC). The FLC has been calculated based upon Hill's [3] condition for localized necking. The limitations of the calculation will be discussed.

1.4 Relation to Other Air Force Programs

This program has been conducted in close cooperation with two other Air Force programs concerning sheet metal formability and sheet forming processes.

- (1) Work on the analytical determination of forming limit curves was conducted by Dr. Louis J. Teutonico as a visiting scientist and consultant to the Air Force Materials Laboratory. The forming limit curve analysis used here was developed under this effort. Dr. Teutonico's work has continued as part of contract F33615-

78-R-5025 entitled "Research to Develop Process Models for Producing a Dual Property Titanium Alloy Compressor Disk" with Battelle Columbus Laboratories as prime contractor.

- (2) A program entitled "Mathematical Modeling of Sheet Metal Formability Indices and Sheet Metal Forming Processes" is being conducted under contract F33615-77-C-5059 by Battelle Columbus Laboratories as part of the Air Force ICAM Program. ALCOA Laboratories, University of Kentucky, University of California (Berkeley), and McDonnell Aircraft Company are subcontractors. The tensile test matrix performed here has been coordinated with this program. Experimental forming limit diagrams (FLD's) on 2024-0 Al (by ALCOA) and on Ti-6Al-4V (by UK) are available for comparison to theoretical predictions. The tensile test results and FLD's referenced in this report are described in detail in the first annual report for the Battelle contract [4]. Bulge test results on 2024-0 Al by ALCOA completed after the annual report date have been transmitted to the author as a private communication [5].

2. CONSTITUTIVE RELATIONS

2.1 Strain Hardening Relationships

In most metal forming calculations, the constitutive relations employed are empirical equations which relate flow stress to strain or strain rate but usually not both. When strain and strain rate are considered together, it is often in terms of an empirical strain hardening law with a superposed power law creep strain rate factor $\dot{\epsilon}^m$.

The most ubiquitous empirical strain hardening relationship is the power law suggested by Holloman [6],

$$\sigma = k \epsilon^n. \quad (2-1)$$

The parameter n is the strain hardening exponent which is the cornerstone of many metal forming calculations. However, Eq. (2-1) is usually an oversimplification in that the strain hardening exponent is not a constant but depends upon strain and strain rate. This leads to a strain hardening law of a different form than Eq. (2-1).

Other strain hardening laws have been proposed. Those discussed most often are by Ludwik[7],

$$\sigma = \sigma_0 + k \epsilon^n, \quad (2-2)$$

by Swift [8],

$$\sigma = k (\epsilon_0 + \epsilon)^n, \quad (2-3)$$

and by Voce [9, 10],

$$\sigma = \sigma_s - (\sigma_s - \sigma_0) \exp(-\epsilon/\eta). \quad (2-4)$$

The main advantage of the Ludwik and Swift laws over the power law is simply that they include three parameters rather than two and, hence, may account for a wider range of strain hardening behavior such as a finite yield stress or effects of a prestrain ϵ_0 . However, it should be noted that the Swift equation will appear in the analysis in this report from a somewhat different perspective.

The Voce equation includes not only a finite yield stress σ_0 , but also a saturation stress σ_s . For this reason among others, Kocks [11] employed the Voce equation to describe the strain rate dependent strain

hardening behavior of high purity aluminum and type 304 stainless steel. In order to fit the Voce equation, he neglected the high strain portion of the tensile data. The strain hardening behavior to be reported here, particularly for 2024-O Al, does not support the concept of a saturation stress and suggests that Kocks' approximation in neglecting the high strain tensile data may not have been justified.

An important feature of our analysis of strain hardening behavior will be an emphasis on the strain hardening derivative and, in particular, on log-log plots of the strain hardening coefficient γ vs. α . A similar approach has been suggested by Reed-Hill et al. [12] who plot $\log (d\sigma/d\epsilon)$ vs. $\log \alpha$. For nickel 270 stress-strain curves obtained at 300K, they observe stages where $\log (d\sigma/d\epsilon)$ decreases linearly with $\log \alpha$ which is similar to the results to be reported here.

Our experimental results show clearly that the strain hardening coefficient γ and strain rate sensitivity v depend, in general, on both strain and strain rate. Hence, strain rate independent strain hardening relationships are not sufficient to model the plastic behavior. A more general approach is required to guide the development of constitutive relations.

2.2 Hart's Phenomenological Approach

The overall requirements for material constitutive relations applicable to sheet metal formability have led us to the phenomenological approach developed by E.W. Hart [13] and recently summarized by Hart et al. [14]. This is a flow theory in which the flow stress is expressed as a function of strain rate, absolute temperature, and one or more explicitly history-dependent parameters which characterize the current structure of the material and evolve with continuing deformation. These structure parameters partially determine the current mechanical properties and can be used, for example, to describe lot-to-lot variations. Strain hardening can be described in terms of the evolution of the structure parameters with accumulated plastic strain. Another important feature of this approach is that the two most important formability indices, the strain hardening coefficient γ and the strain rate sensitivity v , appear as state functions

such that their dependence on stress, strain rate, and temperature can be specified. This implies that the incremental stress-strain relationship

$$d\sigma = \gamma d\epsilon + \nu d\ln \dot{\epsilon} \quad (2-5)$$

can be integrated for any known deformation path.

An analytical form for the rate dependence of the flow stress has recently been proposed by Hart [15], namely

$$\sigma = \sigma^* \exp \left[- \left(\frac{\dot{\epsilon}}{\dot{\epsilon}^*} \right)^{\lambda} \right] + \sigma_0 \dot{\epsilon}^{1/M} \quad (2-6)$$

This equation represents non-elastic grain matrix deformation only with the first term describing thermally-activated flow and the second term describing dislocation glide. The parameters λ and M are material constants and σ^* , $\dot{\epsilon}^*$, and σ_0 represent the current mechanical state. The evolutionary parameters σ^* and $\dot{\epsilon}^*$ are related so Eq. (2-6) includes two independent parameters. The equation should be applicable at all temperatures below about 0.4 times the melting temperature above which grain-boundary sliding must also be considered.

The problem of developing an analytical form to describe strain hardening in terms of the evolution of the history-dependent parameters in Eq. (2-6) is not as well developed. It is expected that the extensive experimental data on strain hardening vs. temperature and strain rate obtained in this program will contribute to a solution to this problem.

3. FORMING LIMITS

3.1 Experimental Forming Limit Diagrams

The forming limit diagram (FLD) approach to assessing limiting strains to failure in a sheet metal process was introduced by S.P. Keeler [16] in 1965. The FLD presents a locus of principal strains (e_1, e_2) in the plane of a sheet beyond which failure is expected. By definition, e_1 is the largest principal strain, and we are concerned with failure related to thinning ($e_3 < 0$). Hence, the FLD covers strain states from pure shear (true strain $\epsilon_2 = -\epsilon_1$) through plane strain ($e_2 = 0$) to balanced biaxial tension ($e_1 = e_2$).

The FLD is determined experimentally by laboratory tests on gridded blanks which produce the appropriate range of principal strain ratios e_2/e_1 . Keeler's original work [16] employed biaxial stretching experiments to produce tension-tension strain states to determine the right-hand side ($e_2 > 0$) of the diagram. Goodwin [17] extended this work to the left-hand side ($e_2 < 0$) using various types of cup and tension tests for tension-compression strain states. The FLD is defined in terms of the major and minor strains measured on a grid of deformed circles at the onset of visible, localized necking. It is drawn to fall below the strains in necked and fracture-affected zones and above the strains found just outside these zones. The original Keeler-Goodwin FLD was presented as a narrow band which helped account for the experimental uncertainty in identifying the forming limits.

The techniques currently being used to generate experimental FLD's can be divided into two groups, in-plane and out-of-plane. For in-plane techniques, the sheet is not bent, and there are usually no surface (frictional) forces or normal pressures. These techniques involve modified tensile specimens and punch-stretching of a reduced thickness patch [18]. The more standard out-of-plane techniques usually follow the modified punch-stretch test routine suggested by Hecker [19]. In these tests, a gridded sheet is clamped securely at the periphery and stretched to failure over a hemispherical punch. Failures are generated over a range of strain ratios e_2/e_1 by increasing the lubrication on the positive side

($\epsilon_2 > 0$) and decreasing the blank width on the negative side ($\epsilon_2 < 0$). The deformation modes in the out-of-plane tests of course correspond more closely to actual sheet metal processes.

While there are some cases for which in-plane and out-of-plane FLD's agree, it is generally found that the out-of-plane limits are appreciably higher than the in-plane limits. This has been discussed by Ghosh and Hecker [20] and, more recently, by Ghosh [21]. The differences are attributed to variations in strain path and in the process of strain localization which is much slower for out-of-plane tests.

3.2 Theoretical Forming Limit Curves

Although the FLD is a basic and useful way to assess formability, it would be difficult to determine the explicit dependence of limit strains on material properties or even identify which properties had the most direct affect. Hence, an important complimentary technique to the FLD is the theoretical forming limit curve (FLC). The FLC represents a specific failure criterion and, hence, a specific set of relevant properties.

Plastic Instability Criteria. The most important failure criteria for sheet forming describe some mode of plastic instability. Swift [8] discussed the onset of diffuse necking and showed that it can begin when the strain hardening coefficient γ reduces to a critical value which depends on the strain ratio (ϵ_2/ϵ_1). For an isotropic sheet deformed by uniaxial stress $\epsilon_2/\epsilon_1 = -1/2$ and the critical value is $\gamma = 1$. However, the onset of diffuse necking is not readily observable, and, hence, the Swift criterion is not a relevant failure criterion for sheet metal.

Plastic instability leads to failure only when a localized neck forms. Hill [3] presented the condition for the onset of a localized neck in a thin sheet. Again, the condition is stated in terms of a critical γ . For an isotropic sheet deformed by uniaxial stress it is $\gamma = 1/2$. However, the Hill condition applies only to the left hand side of the FLC for which $\epsilon_2 < 0$. Also, it does not account for strain rate dependence.

To account for localization of deformation for strain states with $\epsilon_2 > 0$, two approaches have been taken. The first, due to Marciniak and

Kuczynski [22] (M-K) and extended by Hutchinson and Neale [23], postulates the existence of an initial non-homogeneity in the form of a thickness groove across the sheet. As the sheet deforms, the strain becomes localized to this groove. The second approach, first proposed by Stören and Rice [24] and later modified by Hutchinson and Neale [23], incorporates a deformation theory of plasticity into a classical bifurcation analysis. The bifurcation mode corresponds to localized deformation in a narrow band, as in Hill's analysis. Only the first approach will be discussed further.

The M-K analysis was based upon a von Mises yield function incorporating normal anisotropy and Swift's strain hardening relation, Eq. (2-3). Strain rate effects were not included. The M-K approach was also investigated by Sowerby and Duncan [25] who discussed the dependence of forming limits on material properties and by Lee and Kobayashi [2] who extended the calculation to the left-hand side ($\dot{\epsilon}_2 < 0$) and discussed planar anisotropy and strain path dependence.

Strain rate effects were first introduced by Marciniak, Kuczynski, and Pokora [26] (M-K-P) and discussed more recently by Hutchinson and [23]. The strain rate dependence is introduced through the constitutive relation by including a power law creep factor, $\dot{\epsilon}^m$. It is shown that quite small values of the strain rate sensitivity ($m \approx 0.01$) can have a large positive effect on the forming limits. The strain rate dependent calculations have been developed by Ghosh [21] who found good agreement between calculated and experimental forming limits for A-K steel. The rate sensitivity provided nearly a 50 percent enhancement in the calculated plane-strain forming limit.

There are two problems with the M-K and M-K-P analyses which deserve mention. One is the requirement for an initial inhomogeneity. This is usually expressed in terms of a thickness ($f = \Delta t/t$) or strength ($f = \Delta k/k$, k from Eq. (2-3)) defect or combination of both. The calculated forming limits are quite sensitive to the assumed size of the initial inhomogeneity. Ghosh [21] finds agreement between theory and experiment for $f = 0.002 - 0.010$ which he justifies as being reasonable values. Still f is not directly measureable and must be viewed at present as an adjustable parameter. The

other problem involves the extension of the analysis to the left-hand side of the FLC. On the right-hand side, the groove should be taken perpendicular to the axis of the largest principal strain. For the left-hand side this is not the case. Hutchinson and Neale [23] discuss the problem of optimizing the angle between the groove and the principle strain direction so as to obtain the lowest forming limit. For the strain rate independent case, it is probably a good approximation to take the groove (defect) at the Hill [27] angle though for the strain rate dependent case this may not be justified [28]. Since these problems have not been resolved, the FLC calculations in this report will be based on the Hill condition. Unfortunately, this means that strain rate effects are not included.

Hill's Condition for Localized Necking. The derivation of the FLC based on Hill's theory of localized necking is described in reference [1]. It will be reviewed briefly here. Hill's condition is [3],

$$\gamma \geq \left(\frac{\partial f}{\partial \epsilon_1} + \frac{\partial f}{\partial \epsilon_2} \right) / \frac{\partial f}{\partial \epsilon}, \quad (3-1)$$

where f is the yield function as defined in Appendix A. Other assumptions are plane stress, normal isotropy, and proportional straining. Using Eqs. (A4, A5, A20) of Appendix A, it can be shown that the FLC is given by

$$\epsilon_1 + \epsilon_2 = \gamma \bar{\epsilon}. \quad (3-2)$$

The right hand side in Eq. (3-2) can be determined from the constitutive relation as a function of strain ratio (ϵ_2/ϵ_1).

To plot the FLC, we use a parametric form determined from Eqs. (A4, A5). For the Swift strain hardening relation, Eq. (2-3), the effective strain $\bar{\epsilon}$ is related to the critical γ by

$$\gamma = n / (\epsilon_0 + \bar{\epsilon}). \quad (3-3)$$

4. EXPERIMENTAL TEST PROGRAM

4.1 Materials and Test Specimens

The 2024-0 aluminum and titanium -6Al-4V sheet materials used in this project were supplied through Battelle Columbus Laboratories from lots obtained for their sheet metal forming project (see sec. 1.4). Both sheet materials were 0.050 in (1.27 mm) thick.

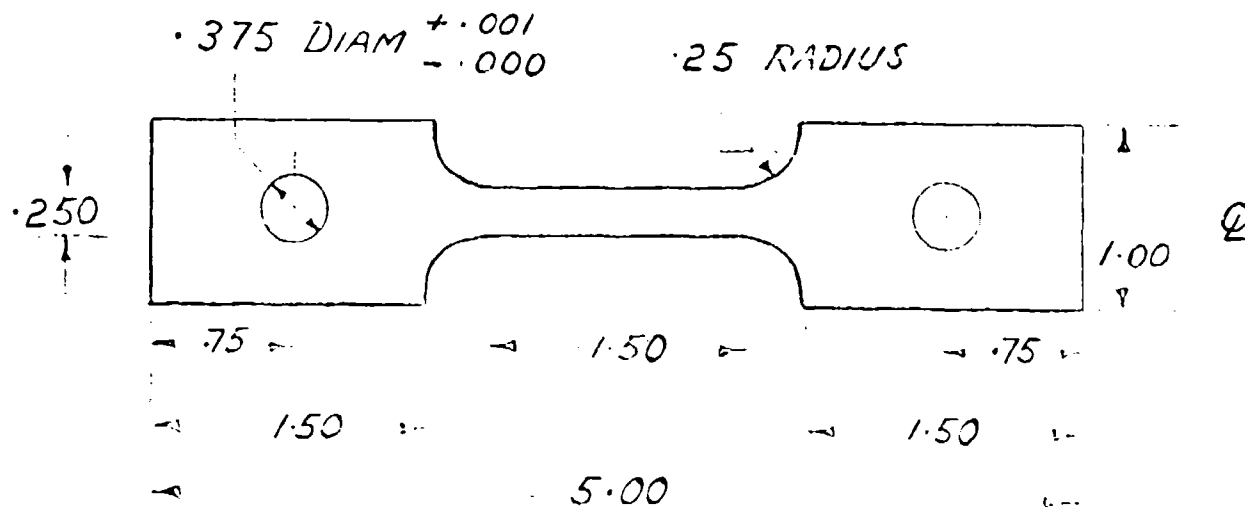
The 2024-0 Al sheet was fabricated by Reynolds Metals Company and supplied according to MIL specification MIL-QQA-250/4. It was not clad. The grain size, determined by ALCOA [4], was a relatively large ASTM 3.5.

The Ti-6Al-4V sheet was fabricated by RMI Company and supplied according to MIL specification MIL-I-9046, type III, composition C in the annealed condition (1450°F for 15 min. + A.C.). Metallographic examination in our laboratory, at the University of Kentucky [4], and at Battelle [4] indicated that:

1. The microstructure is characterized by a fine grain size of 2-5 μ m.
2. The material was not fully (recrystallized) annealed. This is consistent with the MIL specification and industry practice.
3. Some plastic work, as evidenced by apparent grain elongation along the rolling direction, remained in the material.

The crystallographic texture of the Ti-6Al-4V sheet was also determined using X-ray pole figures by Boeing Technology Services, Seattle, Washington, and reported by Battelle [4]. Interpretation of the (0002) pole figure indicated that three textural components were dominant, (1) basal poles aligned with the transverse direction, (2) basal poles rotated approximately 15° from the sheet normal toward the rolling direction, and (3) basal poles aligned with the rolling direction. Neither component was particularly strong with intensities of approximately 2x random. This is a common commercial Ti-6Al-4V texture and leads to r-values > 1.

The sheet materials were cut into test specimen blanks which were machined into pin-loaded tensile specimens of 1.50 in (38.1 mm) gauge length. The specimen design is shown in Fig. 1. All dimensional ratios correspond to the pin-loaded sheet specimen in ASTM specification E-8.



NOTES:

1. Width of reduced section must be accurate to ± 0.002 and uniform to ± 0.0005 within 1.50 in reduced length.
2. Holes must be on Q of reduced section to ± 0.0001 .

FIGURE 1. PIN-LOADED SHEET TENSILE SPECIMEN

Before cutting the sheets, maps and specimen codes were prepared so that the location of each specimen in the sheet could be subsequently determined. Tensile specimens were cut from the sheet in three different orientations, at 0° (L), 90° (T), and 45° (F) to the rolling direction.

It is clear from the results in Sec. 6 of this report that the Ti-6Al-4V sheet material has very limited strain hardening capacity. It is thought that this is due to the fact that it was only partially annealed and retains a structure influenced by the retention of previous plastic work. Hence, for the study of the strain hardening behavior of Ti-6Al-4V, some experiments have been performed on button-head tensile specimens machined from fully annealed Ti-6Al-4V round bar stock available from a previous study [29]. This material had been supplied according to MIL specification MIL-T-9047 and had been annealed at 1450°F for 2 hours plus air cooled.

4.2 Tensile Test Procedures

Both constant extension rate and load relaxation tests were carried out using a 25 kN Instron 1123 screw-driven tester. The crosshead speed could be varied, essentially continuously, from 500 mm/min to below 5×10^{-3} mm/min. This allowed initial strain rates of 10^{-1} to 10^{-5} sec⁻¹ to be obtained.

For load relaxation tests, the loading strain rate was chosen to be 10^{-2} sec⁻¹. Load relaxation data was recorded after stopping the Instron crosshead at a predetermined extension as continued plastic strain in the specimen replaced elastic strain in both the specimen and load train.

For tests above room temperature, specimen temperatures were maintained using a 3-zone split tube furnace with a special high stability Eurotherm three mode controller. For load relaxation tests and for tensile tests at a strain rate of 10^{-2} sec⁻¹ which lasted up to 10 hours, temperatures were controlled to better than $\pm 0.5^\circ\text{C}$.

The determination of plastic strain ratios was carried out by two different methods. (1) Direct width (w) and thickness (t) measurements were made after interrupted tests and compared to initial values. In this case,

$$r = \frac{\epsilon_w}{\epsilon_t} = \frac{\ln(w/w_0)}{\ln(t/t_0)} \quad (4-1)$$

(2) For room temperature tests, an Instron transverse strain sensor was used to record the decrease in thickness continuously. In this case, assuming constant volume during plastic deformation,

$$r = \frac{d\epsilon_w}{d\epsilon_t} = - \frac{d\epsilon_t}{d\epsilon_t} = -1. \quad (4.2)$$

The factor $d\epsilon_w/d\epsilon_t$ can be determined from the slope of the transverse strain sensor output.

4.3 Automatic Data Acquisition System

For both constant extension rate and load relaxation tests, load-time data was obtained digitally using a Hewlett-Packard (HP 3052A) automatic data acquisition system. Digital data acquisition is a necessary component of the testing program in order to provide sufficiently rapid data acquisition at the highest strain rates and sufficient load resolution at the lowest strain rates in load relaxation tests and near the maximum load in constant rate tests. The resolution is necessary to be able to calculate accurate derivatives needed to investigate strain hardening and load relaxation.

The HP 3052A data acquisition system consists of a scanner, digital voltmeter (DVM), timing generator, and plotter controlled by a calculator through a common interface bus. A block diagram of the system is shown in Fig. 2. Data and programs can be displayed on a line printer or stored on a magnetic tape cassette both of which are components of the calculator/controller. Output can also be sent to a teletype (TTY) through a serial interface (ROM) module. The system, as assembled, has 15,036 bytes of read/write memory, and problems due to limited storage can usually be overcome by using the tape cassettes.

A program (DVM RUN) has been developed which enables the calculator to control the scanner and DVM reading sequence. The channels scanned, reading

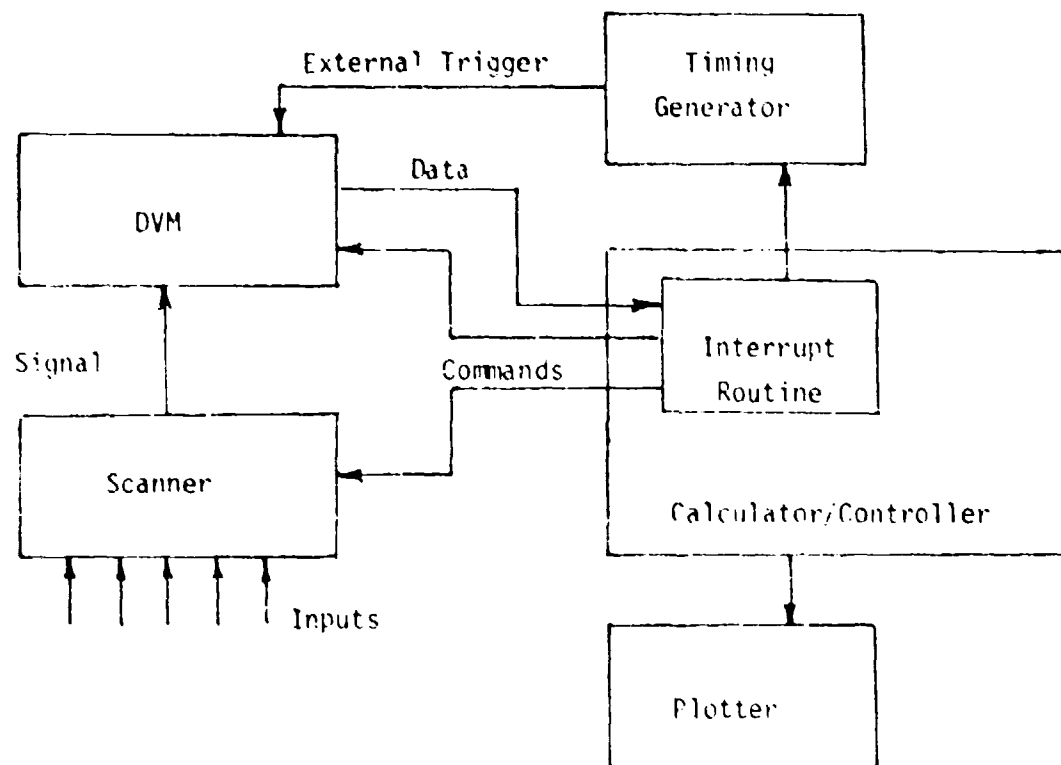


FIGURE 2. BLOCK DIAGRAM OF THE AUTOMATIC DATA ACQUISITION SYSTEM

intervals, and output devices, including changes in these instrument settings, can be preselected for a particular experiment. A flow chart for the DVM RUN program is shown in Fig. 3. The main program accepts a data sequence matrix, triggers the timing generator, sets up data storage and output. Each timing generator pulse initiates an interrupt routine (CSI) which either stores a DVM reading or changes the instrument settings. The maximum reading rate depends somewhat on the data sequence but is approximately 15 sec^{-1} . Since the system has a buffered output capability (limited by the 15k core size), the reading rate is not affected by the speed of the output device.

The DVM readings are stored in a data string (D\$). Interpretation of the DVM readings by channel (load, strain, etc.) and time (after $t=0$) is accomplished by a second program, DVM DATA, which identifies the DVM readings (D\$) according to the data sequence matrix (S\$) and stores voltage-time data pairs by channel in (C\$). The flow chart for DVM DATA is shown in Fig. 4.

At present, the program DVM DATA assumes that up to two channels will be used, but this could easily be increased. In addition, some of the information in (S\$) is also stored in (D\$), redundancy that was convenient during program development.

Listings of the programs DVM RUN and DVM DATA are presented in Appendix B. The language is a modified form of Basic.

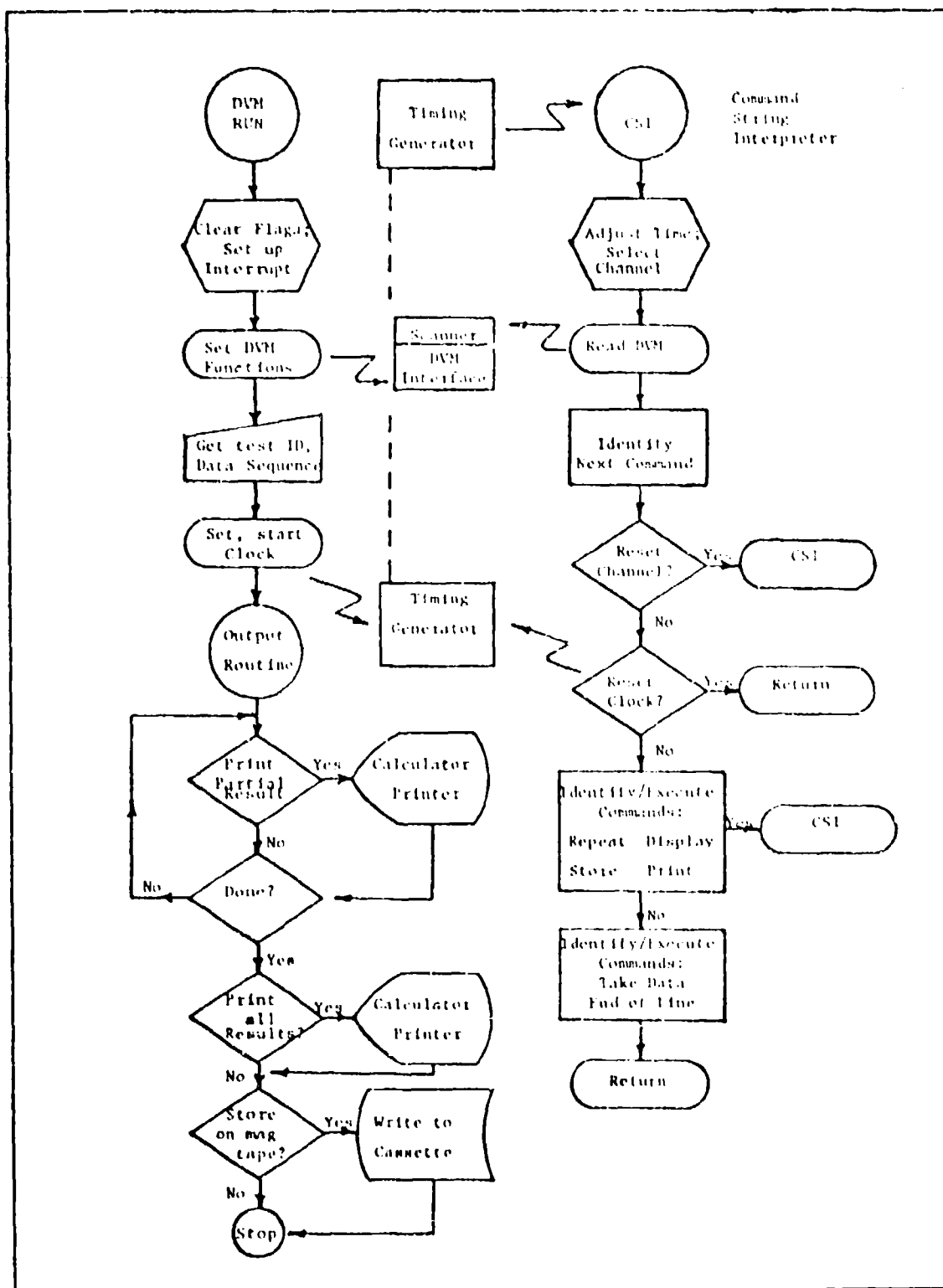


FIGURE 3. FLOW CHART FOR THE AUTOMATIC DATA ACQUISITION SYSTEM PROGRAM DVM RUN

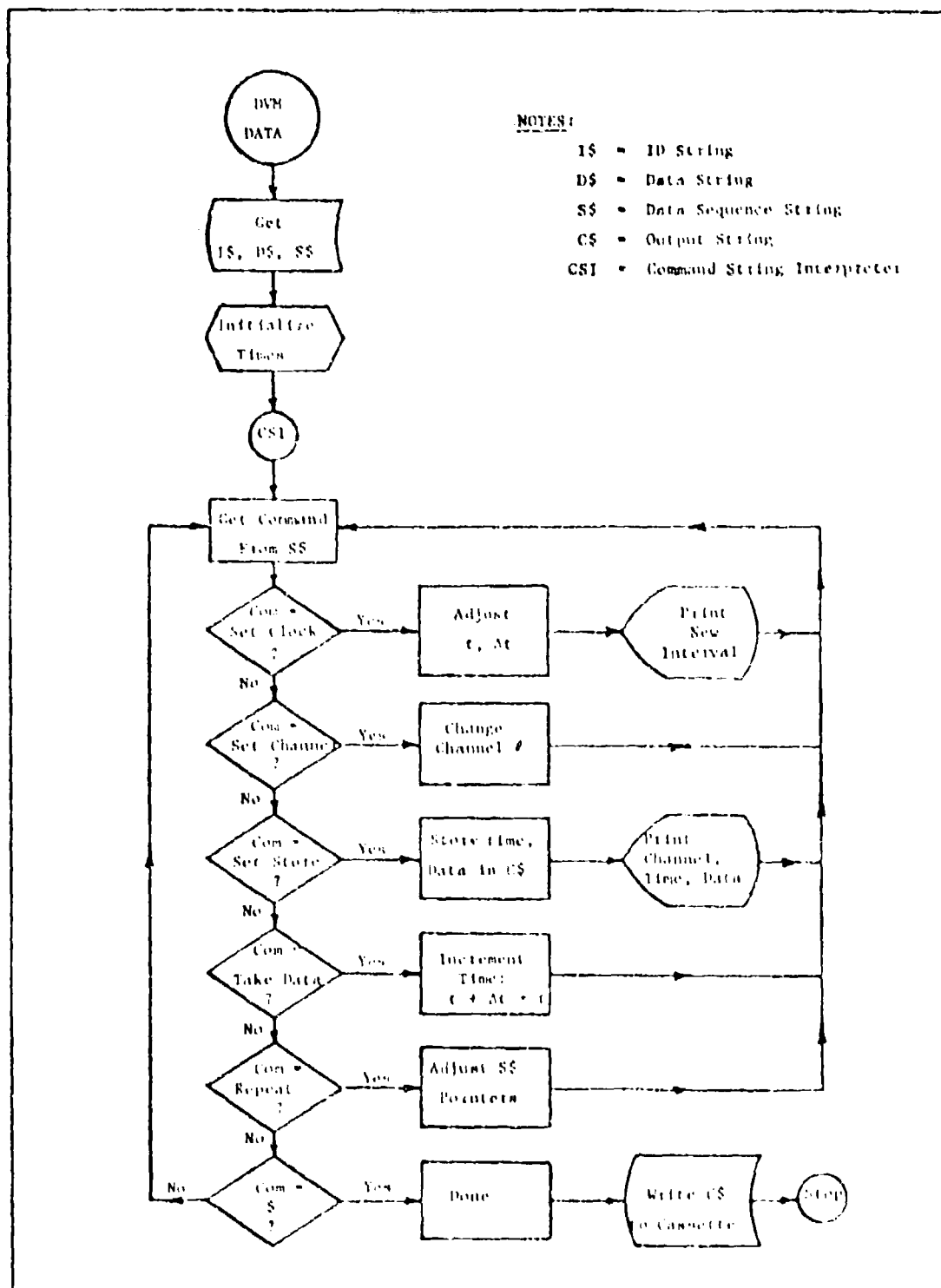


FIGURE 4. FLOW CHART FOR THE AUTOMATIC DATA
ACQUISITION SYSTEM PROGRAM DVM DATA

5. RESULTS FOR 2024-O ALUMINUM

5.1 Constant Extension Rate Tests

Stress-strain curves and tensile test parameters. Constant extension rate tensile tests were performed on the 2024-O aluminum test specimens at temperatures of 25°, 100°, 163° and 225°C. The 163°C (325°F) temperature was selected to represent a typical warm forming temperature for this alloy.

At 25°C, tensile tests were performed on 0°(L), 90°(T), and 45°(F) specimens at strain rates of 10^{-5} to 10^{-1} sec $^{-1}$. For these tests, the Instron transverse strain sensor was used to monitor the decrease in specimen thickness. A typical Instron chart record, obtained at a strain rate of 10^{-3} sec $^{-1}$, is shown in Fig. 5. At strain rates of 10^{-2} sec $^{-1}$ and below, the 25°C load-elongation curves showed strong load serrations (Portevin-LeChatelier effect), and the thickness - elongation curves showed highly non-uniform flow characteristic of Lüders band propagation. The load serrations only began after a critical strain which increased with increasing strain rate. At 10^{-1} sec $^{-1}$, the critical strain was high enough that only one or two serrations were observed. While these effects are well-known in aluminum copper alloys [30] and have recently been reported for 2024 aluminum in particular [31], use of the thickness strain transducer appears to have produced a unique and exceptionally clear picture of the band propagation phenomenon. In spite of the localized deformation, the material appears to strain-harden in a normal manner, and, for the purpose of studying formability, we can consider an averaged, or smoothed, load-elongation curve.

The load-elongation curves have been used to compute a number of standard tensile test parameters. These are summarized for the 25°C tests in Table 1. In this and subsequent tables, σ_y is the engineering stress at 0.2 percent non-elastic strain, σ_{UTS} is the engineering stress at maximum load, ϵ_{unif} is the true non-elastic strain at maximum load, and ϵ_{tot} is the engineering strain at fracture (1.50 in gauge length).

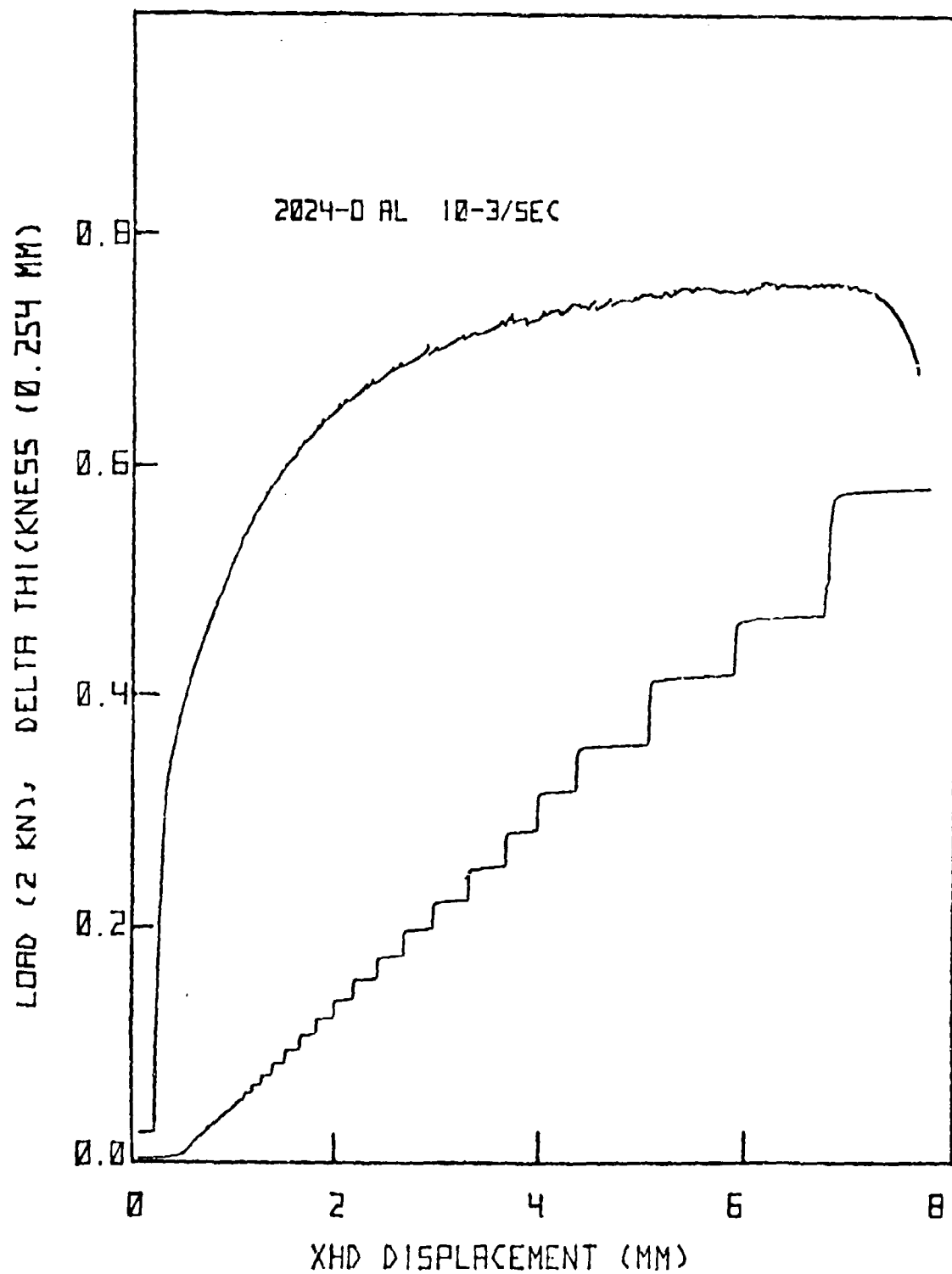


FIGURE 5. LOAD vs. ELONGATION AND CHANGE IN THICKNESS vs. ELONGATION FOR 2024-O ALUMINUM AT 25°C AND 10^{-3} sec^{-1}

TABLE 1. TENSILE TEST PARAMETERS FOR
2024-0 ALUMINUM AT 25°C

Specimen	Rate (sec ⁻¹)	σ_y (MPa)	σ_{UTS} (MPa)	ϵ_{unif}	$\epsilon_{tot}(\%)$
19L	10 ⁻¹	90.5	181.5	0.138	17.7
17L	10 ⁻²	91.5	182.1	0.153	20.4
15L	10 ⁻³	88.6	182.7	0.147	18.3
16L	10 ⁻⁴	92.0	186.9	0.151	19.2
18L	10 ⁻⁵	91.1	191.0	0.160	20.5
20T	10 ⁻¹	91.7	171.0	0.141	17.4
13T	10 ⁻³	89.7	172.4	0.157	18.8
14T	10 ⁻⁵	92.3	179.1	0.149	18.7
12F	10 ⁻¹	89.9	171.3	0.150	18.9
10F	10 ⁻³	85.4	173.1	0.157	19.4
11F	10 ⁻⁵	90.3	180.9	0.156	20.9

In Table 1, the stress σ_y appears to be independent of strain rate for each orientation. The small variations obtained may be due to problems in correcting for the effect of load-train compliance. The ϵ_{unif} and ϵ_{tot} values show some scatter but also seem independent of strain rate. However, the σ_{UTS} values appear to show a small, yet monotonic and probably significant decrease with increasing strain rate. This is believed to be simply another feature of the mechanism which produced the localized plastic deformation illustrated in Fig. 5. In effect, the flow stress is determined by the strain rate characteristic of the band propagation, which is different from and not simply related to, the rate imposed by the testing machine.

For tests at any one strain rate, the σ_{UTS} values for the T and F

specimens are nearly equal and significantly less than those for the L orientation. This will be discussed in more detail below in terms of plastic anisotropy. The σ_{UTS} values reported here are in excellent agreement with those obtained by ALCOA [4] (L:182 MPa, T:172 MPa) at a strain rate of $5 \times 10^{-3} \text{ sec}^{-1}$ on specimens obtained from the same Reynolds 2024-O aluminum lot.

At 163°C, tensile tests were also performed on L, T, and F specimens at strain rates of 10^{-5} to 10^{-1} sec^{-1} . The load-elongation curves were smooth with no visible indication of localized flow. The variation of tensile test parameters with strain rate and orientation is summarized in Table 2.

TABLE 2. TENSILE TEST PARAMETERS FOR
2024-O ALUMINUM AT 163°C

Specimen	Rate (sec^{-1})	σ_y (MPa)	σ_{UTS} (MPa)	ϵ_{unif}	$\epsilon_{tot}(\%)$
51L	10^{-1}	87.2	164.0	0.120	16.2
46L	10^{-2}	83.7	162.6	0.127	21.6
45L	10^{-3}	82.6	155.0	0.127	33.3
49L	10^{-4}	81.2	138.9	0.112	30.5
50L	10^{-5}	81.4	131.4	0.121	21.9
24T	10^{-1}	79.7	157.3	0.122	16.2
23T	10^{-2}	81.4	156.3	0.135	21.0
19T	10^{-3}	83.9	152.3	0.130	32.8
18T	10^{-4}	80.6	136.3	0.134	34.8
40F	10^{-1}	81.5	154.9	0.124	17.2
13F	10^{-2}	80.8	154.5	0.145	24.7
25F	10^{-3}	81.4	147.0	0.137	34.4
28F	10^{-4}	79.0	133.9	0.135	35.0

Again σ_y and ϵ_{unif} appear to be effectively independent of strain rate. However, the σ_{UTS} values now indicate a clearly positive strain rate sensitivity, and the ϵ_{tot} values are strongly strain rate dependent with a maximum near 10^{-3} or 10^{-4} sec^{-1} . It has been shown [32] that the post-uniform elongation ($\epsilon_{tot} - \epsilon_{unif}$) in a tensile test is determined predominantly by the strain rate sensitivity. Hence, the variation in ϵ_{tot} in Table 2 indicates a rate dependent strain rate sensitivity that is largest near 10^{-3} or 10^{-4} sec^{-1} .

The variation in tensile properties with strain rate at 163°C is also illustrated in Fig. 6 by the true stress - true strain curves (up to ϵ_{unif}) for the five L specimens of Table 2. This figure also suggests that the influence of strain rate is largest between 10^{-3} and 10^{-4} sec^{-1} .

Tensile tests at 100°C and 225°C were conducted only on L specimens at a strain rate of 10^{-2} sec^{-1} . The true stress-true strain curves (up to ϵ_{unif}) for the L specimens at 10^{-2} sec^{-1} for all four test temperatures are shown in Fig. 7, and the tensile properties are summarized in Table 3. The σ_y , σ_{UTS} , and ϵ_{unif} values all decrease with increasing temperature. The large ϵ_{tot} value at 225°C is an indication of a large strain rate sensitivity for that test.

TABLE 3. TENSILE TEST PARAMETERS FOR
2024-O ALUMINUM AT 10^{-2} sec^{-1}

Specimen	Temperature ($^\circ\text{C}$)	σ_y (MPa)	σ_{UTS} (MPa)	ϵ_{unif}	$\epsilon_{tot}(\%)$
17L	25	91.5	182.1	0.153	20.4
73L	100	88.2	175.5	0.151	18.7
46L	163	83.7	162.6	0.127	21.6
72L	225	70.6	103.1	0.088	61.5

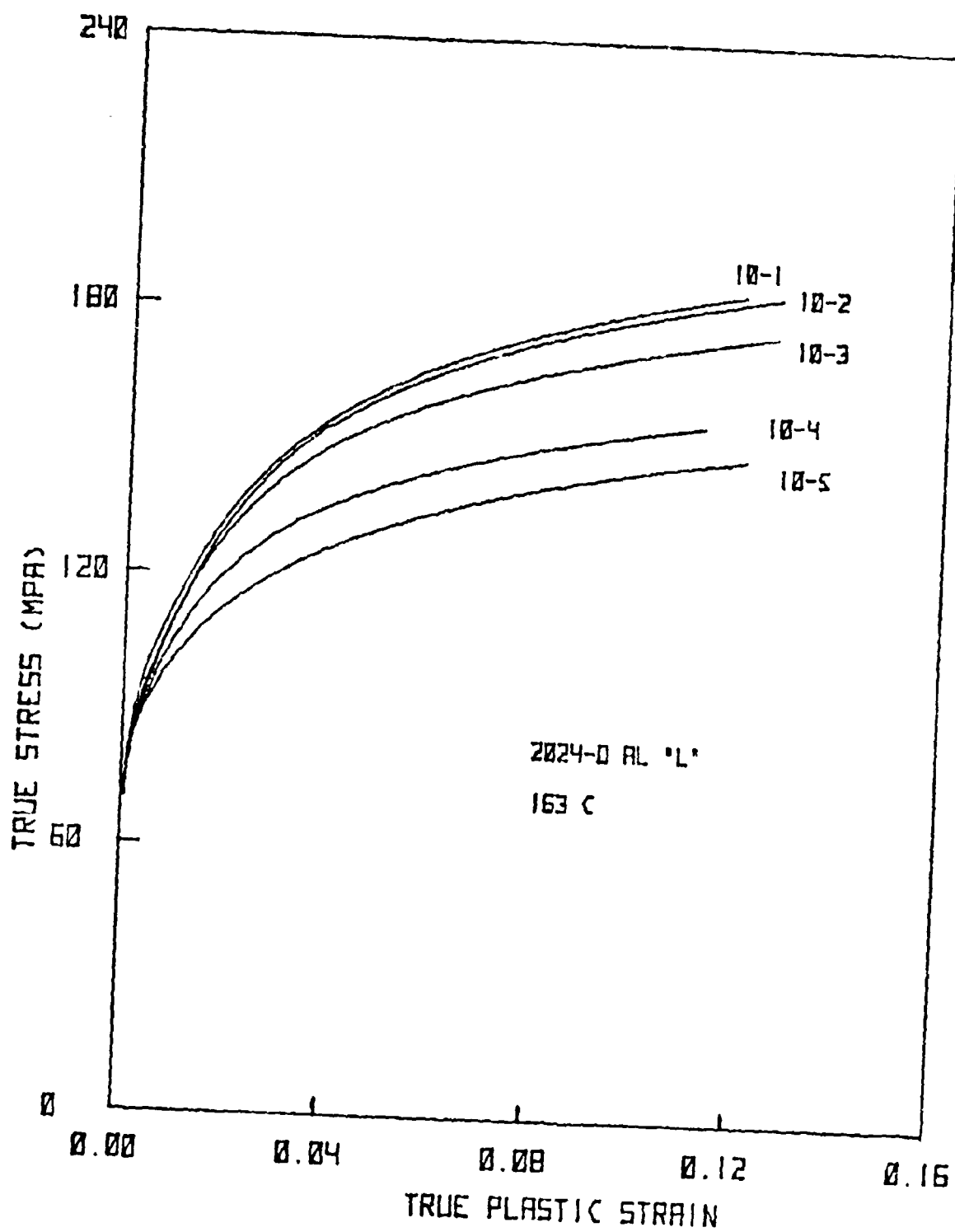


FIGURE 6. TENSILE TRUE STRESS - TRUE STRAIN CURVES FOR 2024-O ALUMINUM AT 163°C vs. STRAIN RATE

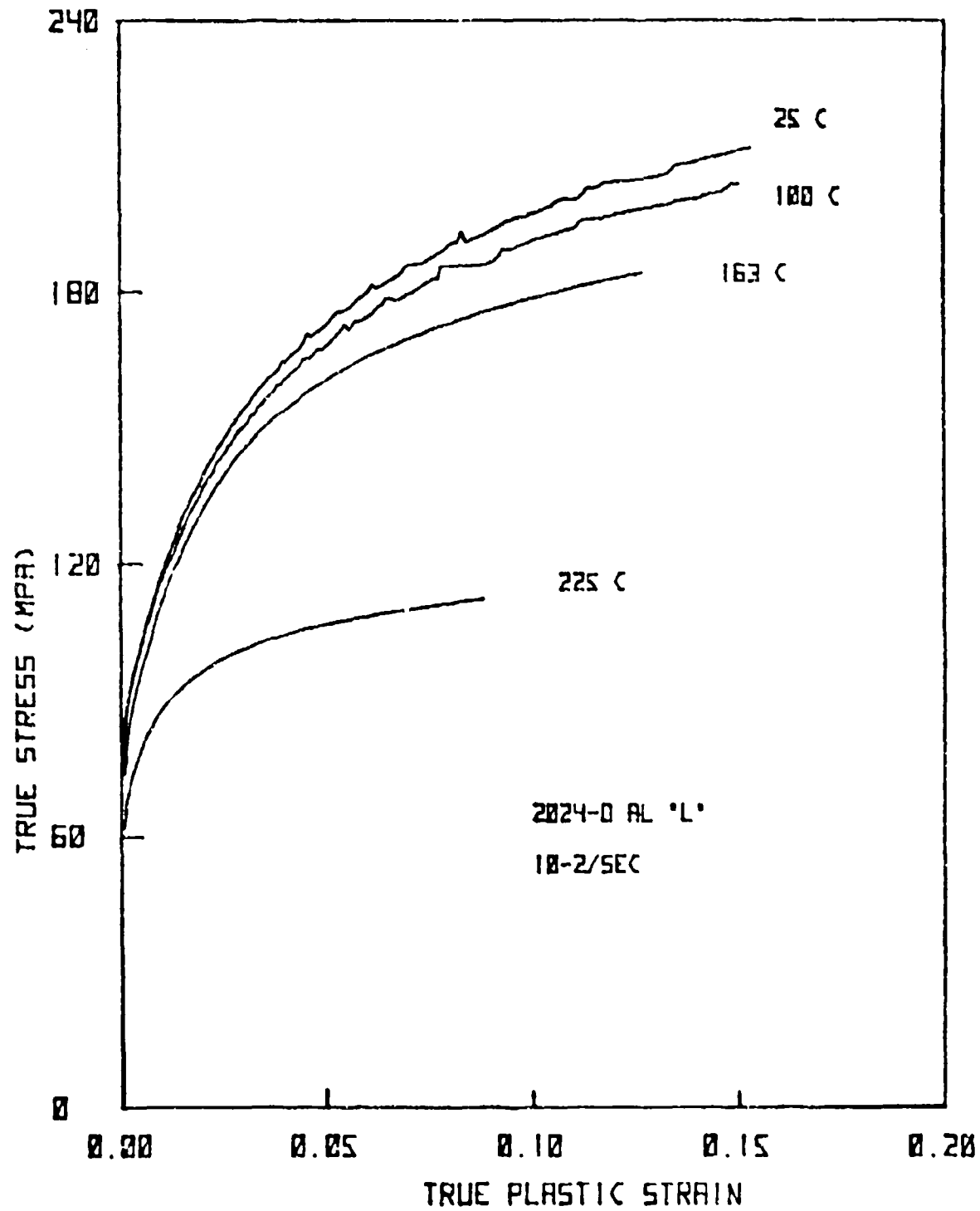


FIGURE 7. TENSILE TRUE STRESS - TRUE STRAIN CURVES FOR 2024-O ALUMINUM AT 10^{-2} sec⁻¹ vs. TEMPERATURE

Plastic Anisotropy. The plastic anisotropy of the aluminum sheet is characterized by the plastic strain ratios $r = \epsilon_w / \epsilon_t$ measured for specimens cut at 0° (L), 90° (T), and 45° (F) to the rolling direction. The r -values were determined from direct width and thickness measurements according to Eq. (4-1). Measurements were made during interrupted tests conducted at 25°C and a strain rate of 10^{-3} sec^{-1} and at strains of approximately 2, 3, 5, and 10 percent. No significant variation with strain was observed. The measured values of r_0 , r_{90} , and r_{45} are given in Table 4 along with values determined by Battelle (at 10^{-2} sec^{-1}) [4] and ALCOA (at $5 \times 10^{-3} \text{ sec}^{-1}$) [4].

TABLE 4. R-VALUES FOR 2024-O ALUMINUM
AT 25°C

Orientation	This Investigation (at 10^{-3} sec^{-1})	Battelle [4] (at 10^{-2} sec^{-1})	ALCOA [4] (at $5 \times 10^{-3} \text{ sec}^{-1}$)
r_0	0.74	0.45-0.62	0.74
r_{90}	0.64	0.51-0.57	0.56
r_{45}	0.77	0.62-0.80	--

It should also have been possible to determine the r -values from the slopes of the transverse strain sensor output (see Fig. 5), at least for strains below the onset of unstable flow. However, the transverse strain sensor output generally indicated larger changes in thickness and, hence, smaller r -values than those measured directly. This discrepancy is not understood, and the directly measured r -values are preferred. However, the linear form of the transverse strain sensor output, exclusive of the "staircase" behavior in the localized flow regime, also indicates that the r -values do not depend significantly on strain. In addition, the transverse strain sensor slopes did not vary noticeably with strain rate so we expect that the strain rate dependence of the r -values is small.

The σ_{UTS} values in Table 1 show that the tensile flow stress is dependent upon the orientation of the test specimen. At a strain rate of 10^{-3} sec^{-1} , the σ_{UTS} values for T and F orientations are approximately equal

but are about 6 percent less than that for the L orientation. This dependence can be discussed in terms of Hill's [27] theory of planar plastic anisotropy. The relevant yield function and definition of effective stress are presented in Appendix A. In particular, expressions for the ratios of the effective stress $\bar{\sigma}$ to the tensile stress σ_T in terms of the measured r-values are given by Eqs. (A13-A15). The corresponding relationships between the effective strain $\bar{\epsilon}$ and tensile strain ϵ_T are given by Eq. (A17). The same formulation can be used to relate effective stress and strain to the stress σ_B and strain ϵ_B measured in a hydraulic bulge test. These ratios are given in Eqs. (A16) and (A18) and are based on the assumption of balanced biaxial stress. These stress ratios and strain ratios have been calculated for the measured r-values and are summarized in Table 5.

TABLE 5. EFFECTIVE STRESS - EFFECTIVE STRAIN
CONVERSION FACTORS AT 25°C

Test	Orientation	$\bar{\sigma}/\sigma$	$\bar{\epsilon}/\epsilon$
Tensile	0°(L)	0.949	1.053
Tensile	90°(T)	0.991	1.009
Tensile	45°(F)	0.994	1.006
Bulge	--	1.057	0.946

In order to compare the stress-strain curves vs. orientation, the effective stresses at effective strains of 0.05, 0.10, and 0.15 are given in Table 6 for the three 10^{-3} sec^{-1} runs of Table 1. In addition, bulge test results reported by ALCOA [5] on specimens obtained from the same Reynolds 2024-0 lot are also included. The bulge test stresses are average values from four different tests. It is clear from Table 6 that the effective stress-effective strain curves determined for the three tensile orientations are effectively coincident. The bulge test results are not as close and differ from the tensile results by about 10 percent. Considering the approximate manner by which hydraulic pressure and change in thickness are converted to true stress - true strain for the bulge test [5], the agreement is considered satisfactory. However, it does not lend support to the anisotropy correction factors as the tensile

TABLE 6. EFFECTIVE STRESS VS. EFFECTIVE STRAIN FOR 2024-0 ALUMINUM TENSILE AND BULGE TESTS AT 25°C.

Test	Specimen	Effective Stress $\bar{\sigma}$ at $\bar{\epsilon} =$		
		0.05	0.10	0.15
Tensile	15L (0°)	163.5	186.4	199.5
Tensile	13T (90°)	164.0	185.2	198.0
Tensile	10F (45°)	163.1	185.1	198.9
Bulge	ALCOA [5]	187.0	206.2	217.8

results do. Similar comparison between tensile and bulge test results for aluminum alloys have previously been reported by several investigators [33, 34].

It is concluded that Hill's theory of planar anisotropy together with r -values determined from measured strain ratios can be used to account for the plastic anisotropy of 2024-0 aluminum.

Strain Hardening Behavior. Since the true stress - true strain curves for the L, T, and F orientations at 25°C can be brought into coincidence using Hill's theory of planar anisotropy, the discussion of the strain hardening behavior will be restricted to a single (L) orientation. Referring to Tables 1 and 2 it is seen that the dependence of σ_{UTS} on orientation is roughly the same at 163°C as for 25°C, with σ_{UTS} for the L orientation greater than that for T and F. So it will be assumed that the r -values measured at 25°C can also be used at 163°C and the tensile data at both temperatures will be reduced to effective stress - effective strain using the factors in Table 5.

The strain hardening behavior will be investigated in terms of the dependence of the derivative

$$\gamma = \left(\partial \ln \sigma / \partial \epsilon \right)_c \quad (5-1)$$

on stress at various strain rates $\dot{\epsilon}$. The choice of variables, $\gamma = \gamma(\sigma, \dot{\epsilon})$, is based on Hart's concept [15] that these are state variables which partially describe the current structure (and future response) of the material. Although the experiments are at constant extension rate and not constant strain rate as implied in the definition of γ , the derivatives of the stress-strain curve can

be identified as γ with negligible error. For a constant extension rate test [35],

$$d \ln \sigma / d \epsilon = \gamma - (\partial \ln \sigma / \partial \ln \dot{\epsilon})_{\epsilon} = \gamma - \nu. \quad (5-2)$$

For the results presented here, $\gamma > 1$ and $\nu < 0.1$. Hence, the strain rate sensitivity ν makes a negligible contribution to the total derivative.

Figure 8 shows a plot of γ vs $\bar{\sigma}$ for the 2024-0 aluminum test run at 163°C and 10^{-3} sec^{-1} . This is a smooth curve over the entire range of data (equivalent to $5 \times 10^{-3} \leq \bar{\epsilon} < \bar{\epsilon}_{\text{unif}}$) and provides no obvious clue as to how to model the strain hardening. It is more instructive to examine a plot of $\log \gamma$ vs $\log \bar{\sigma}$. This plot is shown in Fig. 9 for the same test as Fig. 8. Regions of different curvature in Fig. 8 now appear as regions of different slope in Fig. 9. The most distinctive feature is the linear decrease in $\log \gamma$ with $\log \bar{\sigma}$ at large stresses. Reference to the stress strain data shows that the linear portion begins at a strain of approximately $\bar{\epsilon} = 0.05$. Since we are interested in the large strain behavior for predicting formability, it is sufficient to model the strain hardening for $\bar{\epsilon} > 0.05$ phenomenologically by assuming

$$\ln \gamma = \ln A - B \ln \bar{\sigma} \quad (5-3)$$

where A and B are constants which can be determined by linear regression from the strain hardening data. This straight line is shown in Fig. 9.

Integrating Eq. (5-3) we obtain an expression for the stress-strain curve,

$$\bar{\sigma} = (AB)^{1/B} \left[\sigma_0^B / AB + \bar{\epsilon} \right]^{1/B} \quad (5-4)$$

where σ_0 is the stress at $\bar{\epsilon} = 0$. Although A and B can be determined from the strain hardening data, σ_0 must be determined using the stress-strain data. While there are several ways to do this, we have used a linear regression analysis of $\bar{\sigma}^B$ vs $\bar{\epsilon}$.

It is to be noted that Eq. (5-4) is the same form as that originally proposed by Swift [8],

$$\sigma = k (\epsilon_0 + \epsilon)^n. \quad (5-5)$$

However, in our application, $n = 1/B$ is determined from the dependence of γ on stress, and $\epsilon_0 = \sigma_0^B / AB$ need not be interpreted as a prestrain. In fact, it will be seen that for 2024-0 aluminum, ϵ_0 will come out negative. This

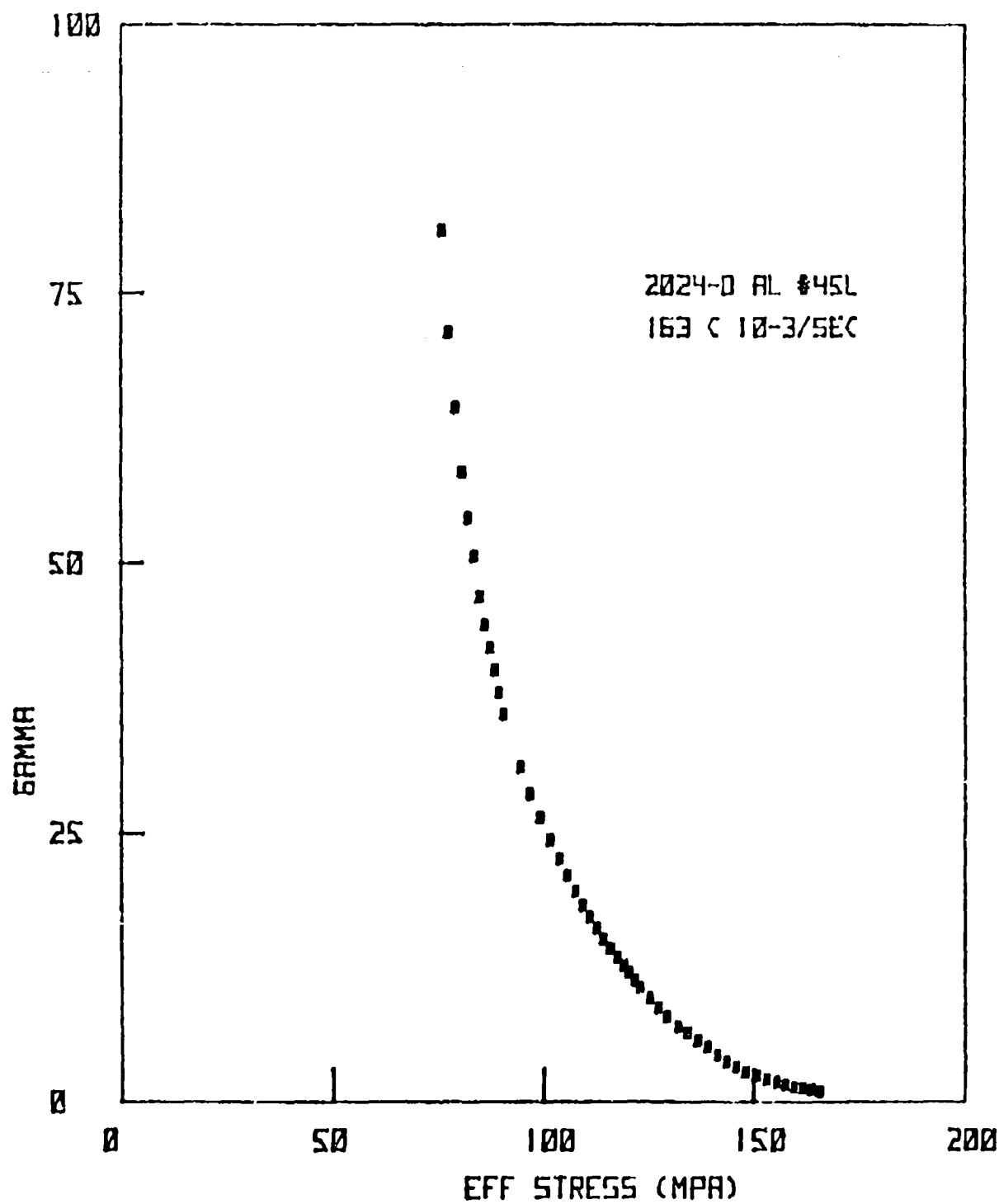


FIGURE 8. STRAIN HARDENING BEHAVIOR PRESENTED AS γ vs. EFFECTIVE STRESS σ FOR 2024-O ALUMINUM AT 163°C and 10⁻³ sec⁻¹

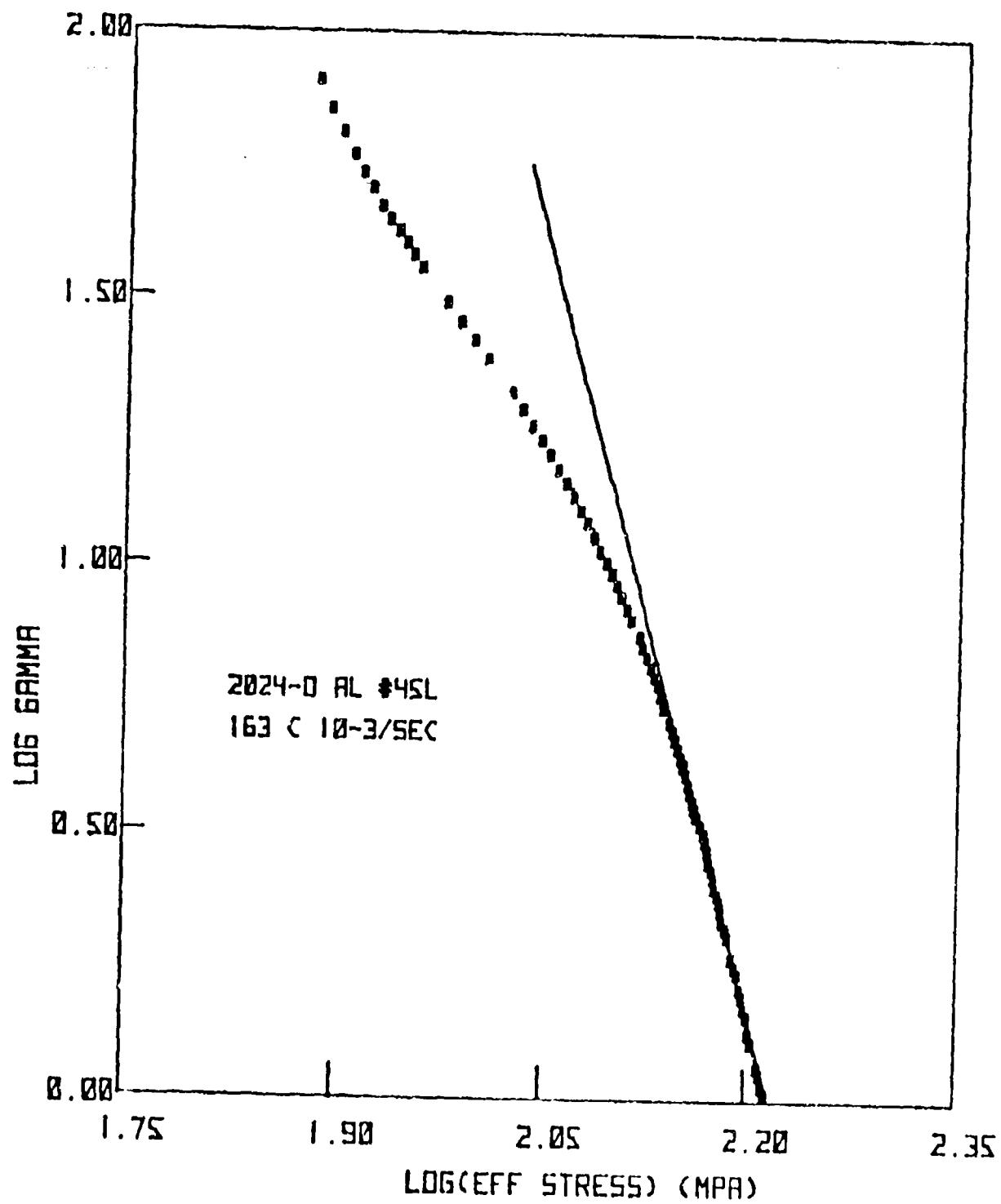


FIGURE 9. STRAIN HARDENING BEHAVIOR PRESENTED AS LOG γ vs. LOG $\bar{\sigma}$
FOR 2024-O ALUMINUM AT 163°C AND 10⁻³ sec⁻¹

simply represents the fact that the straight line fit in Fig. 8 extrapolates to higher derivatives $\dot{\gamma}$ at low stress than those actually measured. Hence, the fitted Swift equation will curve below the experimental points at small strains. The small strain regime can be ignored or modeled separately, as required by the application.

Using the $\log \dot{\gamma}$ vs. $\log \bar{\sigma}$ and $\bar{\sigma}$ vs. $\bar{\epsilon}$ data, the Swift equation parameters have been determined vs. strain rate for the five L specimens tested at 25°C (see Table 1) and at 163°C (see Table 2). These are summarized in Tables 7 and 8 respectively along with a comparison between the calculated maximum uniform strain

$$\epsilon_{unif} = n - \epsilon_0 \quad (5-6)$$

and the measured (effective) value $\bar{\epsilon}_{unif}$.

The success of this fitting procedure is illustrated by the effective stress-strain curve and Swift equation fit for the 163°C, 10^{-3} sec^{-1} test in Fig. 10. It is especially significant that the fitting procedure presented here produces an excellent match between calculated and experimental slopes. It is the slope of the stress strain curve which directly determines the formability when failure occurs by plastic instability.

TABLE 7. SWIFT EQUATION PARAMETERS FOR
2024-O ALUMINUM AT 25°C.

Specimen	Rate (sec^{-1})	n	ϵ_0	k(MPa)	n- ϵ_0	$\bar{\epsilon}_{unif}$
19L	10^{-1}	0.147	-0.015	266.8	0.162	0.145
17L	10^{-2}	0.134	-0.023	262.5	0.157	0.161
15L	10^{-3}	0.144	-0.017	266.7	0.161	0.155
16L	10^{-4}	0.116	-0.032	259.6	0.148	0.159
18L	10^{-5}	0.129	-0.030	273.1	0.159	0.168
average values		0.134	-0.023	265.7	0.157	0.158

In Table 7, none of the parameters n, ϵ_0 , or k for the 25°C tests show a smooth or significant variation with strain rate. The same is true for the

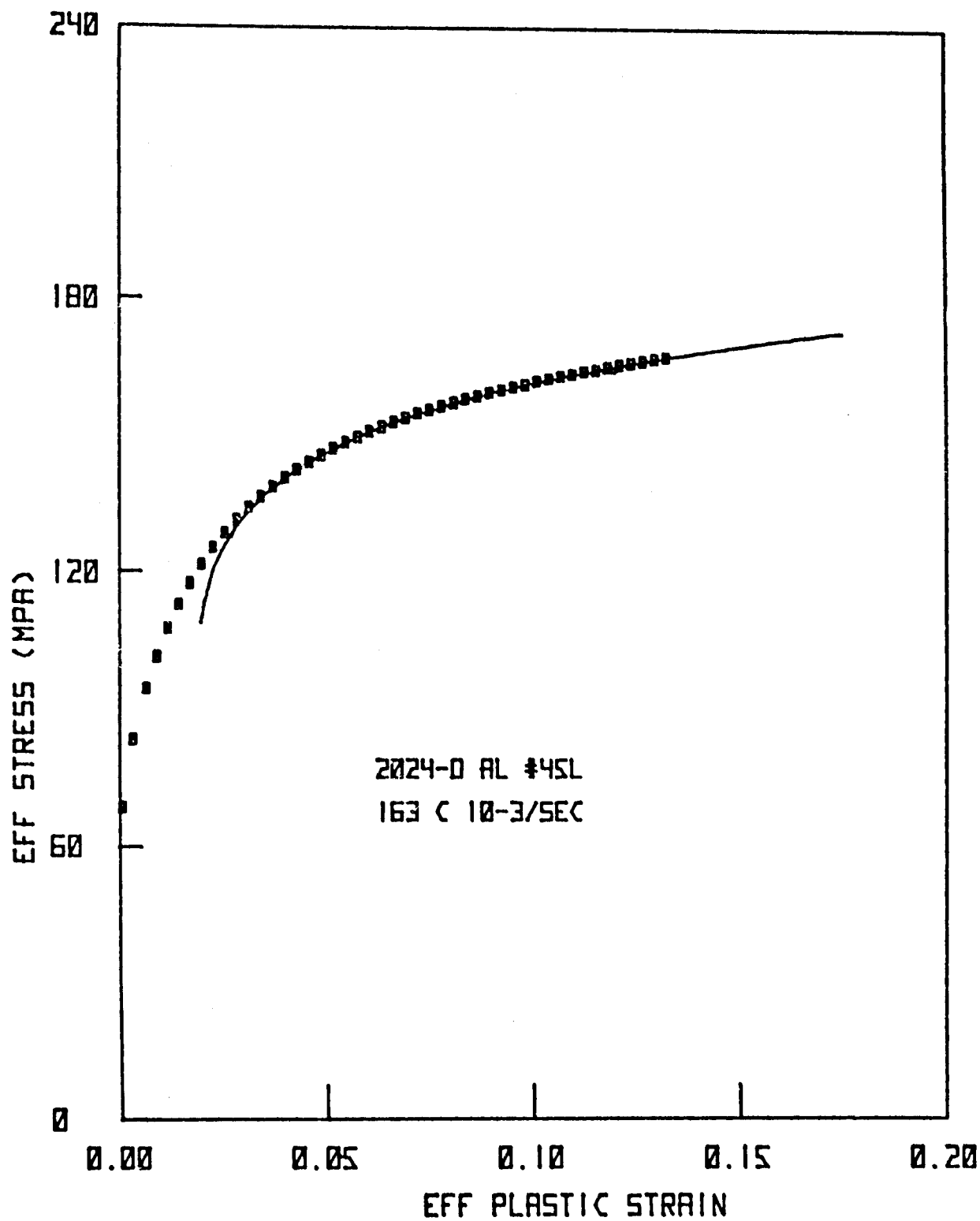


FIGURE 10. EFFECTIVE STRESS-STRAIN CURVE WITH SWIFT EQUATION FIT
FOR 2024-O ALUMINUM AT 163°C AND 10⁻³ sec⁻¹

uniform strains. Hence it is concluded that the high strain, strain hardening behavior of 2024-O aluminum at 25°C is effectively independent of strain rate. For this reason, average values of the Swift equation parameters and uniform strains have been included. At 25°C, the constitutive equation based on these average values is

$$\bar{\sigma} \text{ (MPa)} = 265.7 (-0.023 + \bar{\epsilon})^{0.134} \quad (5.7)$$

For the individual runs, and particularly for the average values, we obtain excellent agreement between calculated and observed uniform strains.

TABLE 8. SWIFT EQUATION PARAMETERS FOR 2024-O ALUMINUM AT 163°C.

Specimen	Rate (sec ⁻¹)	n	ϵ_0	k(MPa)	n- ϵ_0	$\bar{\epsilon}_{unif}$
51L	10 ⁻¹	0.107	-0.022	223.6	0.129	0.126
46L	10 ⁻²	0.109	-0.021	222.3	0.130	0.134
45L	10 ⁻³	0.104	-0.018	209.1	0.122	0.133
49L	10 ⁻⁴	0.098	-0.016	184.5	0.114	0.118
50L	10 ⁻⁵	0.107	-0.018	178.3	0.125	0.127
average values		0.105	-0.019	--	0.124	0.128

For the 163°C tests in Table 8, neither n, ϵ_0 , or the uniform strains show a significant variation with strain rate and average values have been presented. However, k increases significantly and non-uniformly with increasing strain rate. Hence, a simple constitutive equation like Eq. (5-7) will not be presented for the 163°C strain hardening behavior. The strain rate dependence of the strain hardening behavior is further illustrated in Fig. 11 which shows (from left to right) the log γ plots for strain rates of 10⁻⁵, 10⁻⁴, 10⁻³, and 10⁻² sec⁻¹. The 10⁻¹ sec⁻¹ plot has been omitted since it is essentially coincident with the 10⁻² sec⁻¹ plot. Figure 11 shows that, although the n-values are constant and k-values strain rate dependent for the high strain behavior, essentially the opposite is the case for the low strain behavior. The slight upward curvature at very low strains, also

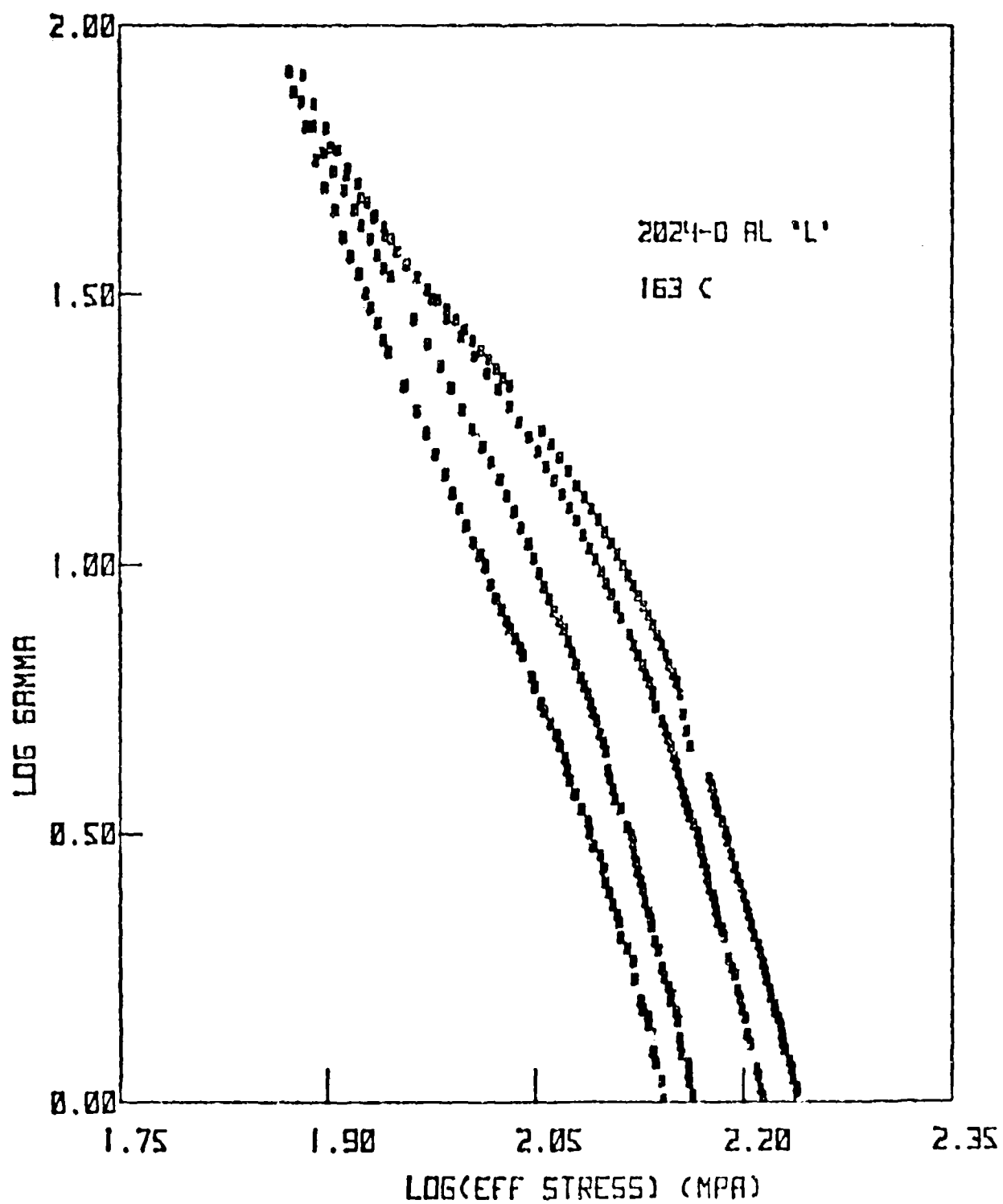


FIGURE 11. STRAIN HARDENING BEHAVIOR vs. STRAIN RATE FOR 2024-O ALUMINUM AT 163°C. CURVES ARE FOR (L to R) 10^{-5} , 10^{-4} , 10^{-3} , 10^{-2} sec $^{-1}$

evident in Fig. 9, represents a transient strain which appears to saturate by $\bar{\epsilon} \approx 5 \times 10^{-3}$. The strain rate dependence of the strain hardening behavior is largest near a strain rate of 10^{-3} or 10^{-4} sec^{-1} which is, of course, consistent with the high strain tensile test results presented in sec. 5.1. In summary, the stress and strain rate dependence of γ shown in Fig. 11 indicates that the strain hardening behavior of 2024-0 aluminum at 163°C cannot be modeled by a strain rate independent constitutive equation. The explicit dependence on strain rate will have to be taken into account.

Comparison Between Tensile and Bulge Tests. In Table 6, the tensile effective stress-effective strain data is compared to bulge tests results on the same 2024-0 lot reported by ALCOA [5]. This comparison is made within the range of tensile strains, $\bar{\epsilon} < \bar{\epsilon}_{\text{unif}}$. Since one important objective of the development of constitutive equations is the ability to extrapolate outside the range of tensile data, comparison will also be made to the bulge tests results at the larger strains achievable in that test.

Figure 12 shows a comparison between the Swift equation fit to the high strain tensile data for the 25°C , 10^{-1} sec^{-1} test and several bulge test data points. The comparison is similar to that indicated in Table 6. The values of effective stress determined from the bulge test are about 10 percent above the extrapolated tensile data. The strain hardening behavior (slopes) appear very similar.

The strain hardening behaviors are compared further in Fig. 13 which shows $\log \gamma$ vs. $\log \bar{\sigma}$ for (a) tensile data obtained at 25°C , 10^{-1} sec^{-1} , (b) the average Swift equation for the 25°C results from Eq. (5-7), and (c) bulge test data. It is seen that the bulge test data agree well with the linear extrapolation of the decrease in $\log \gamma$ vs. $\log \bar{\sigma}$ based on the high strain tensile data.

In sec. 7, it will be seen that the calculation of the theoretical FLC for plastic instability is based entirely on γ values less than one. In order to use constitutive equation parameters determined from tensile data, extrapolation to values of γ at $\bar{\epsilon} > \bar{\epsilon}_{\text{unif}}$ is required. The comparison to the ALCOA bulge test data supports such extrapolation if the procedures developed here for modeling the tensile strain hardening behavior are employed.

5.2 Load Relaxation Tests.

Load relaxation tests were used to investigate the dependence of the flow

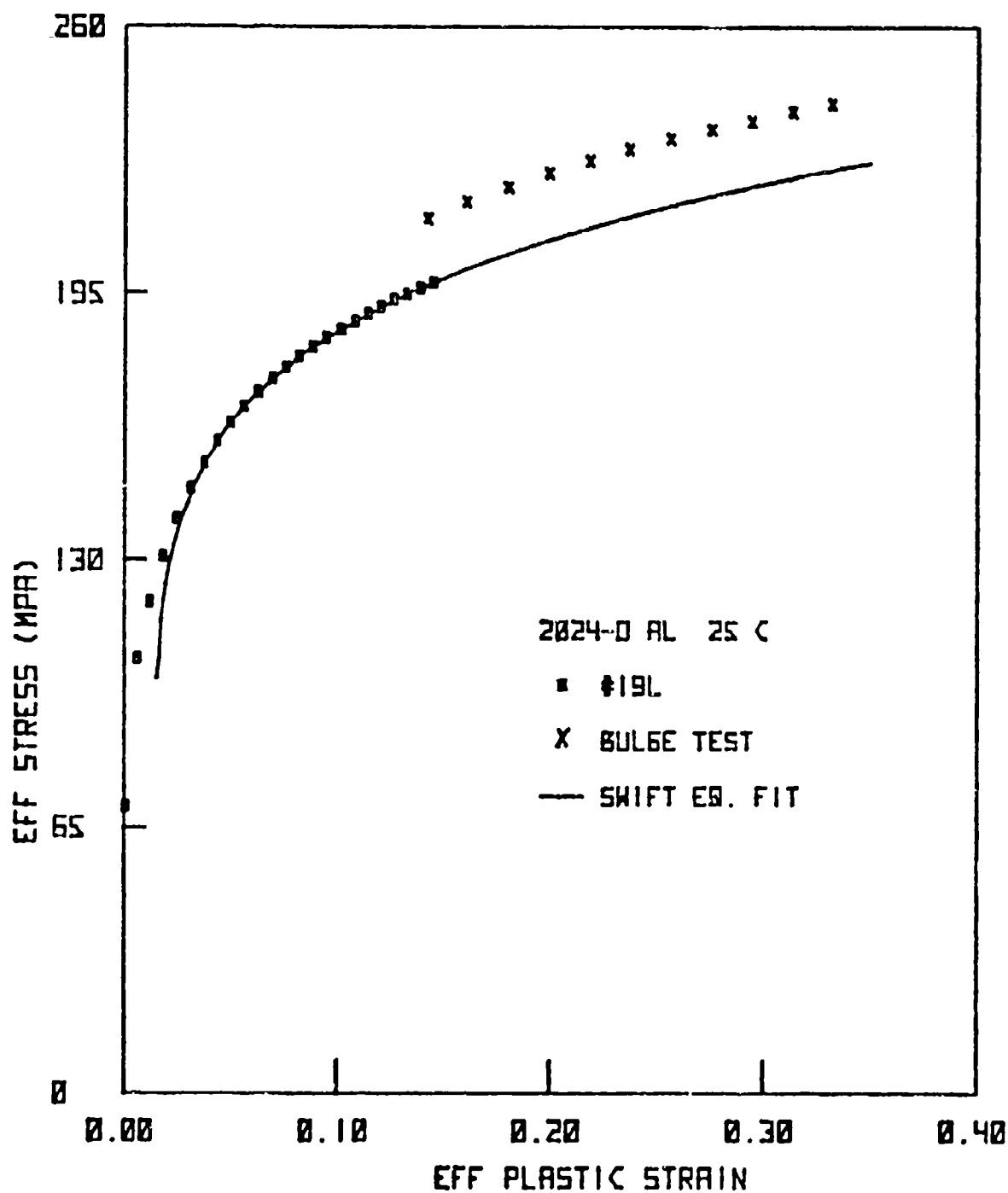


FIGURE 12. COMPARISON OF AN EXTRAPOLATED TENSILE EFFECTIVE STRESS-STRAIN CURVE WITH BULGE TEST DATA FOR 2024-O ALUMINUM AT 25°C

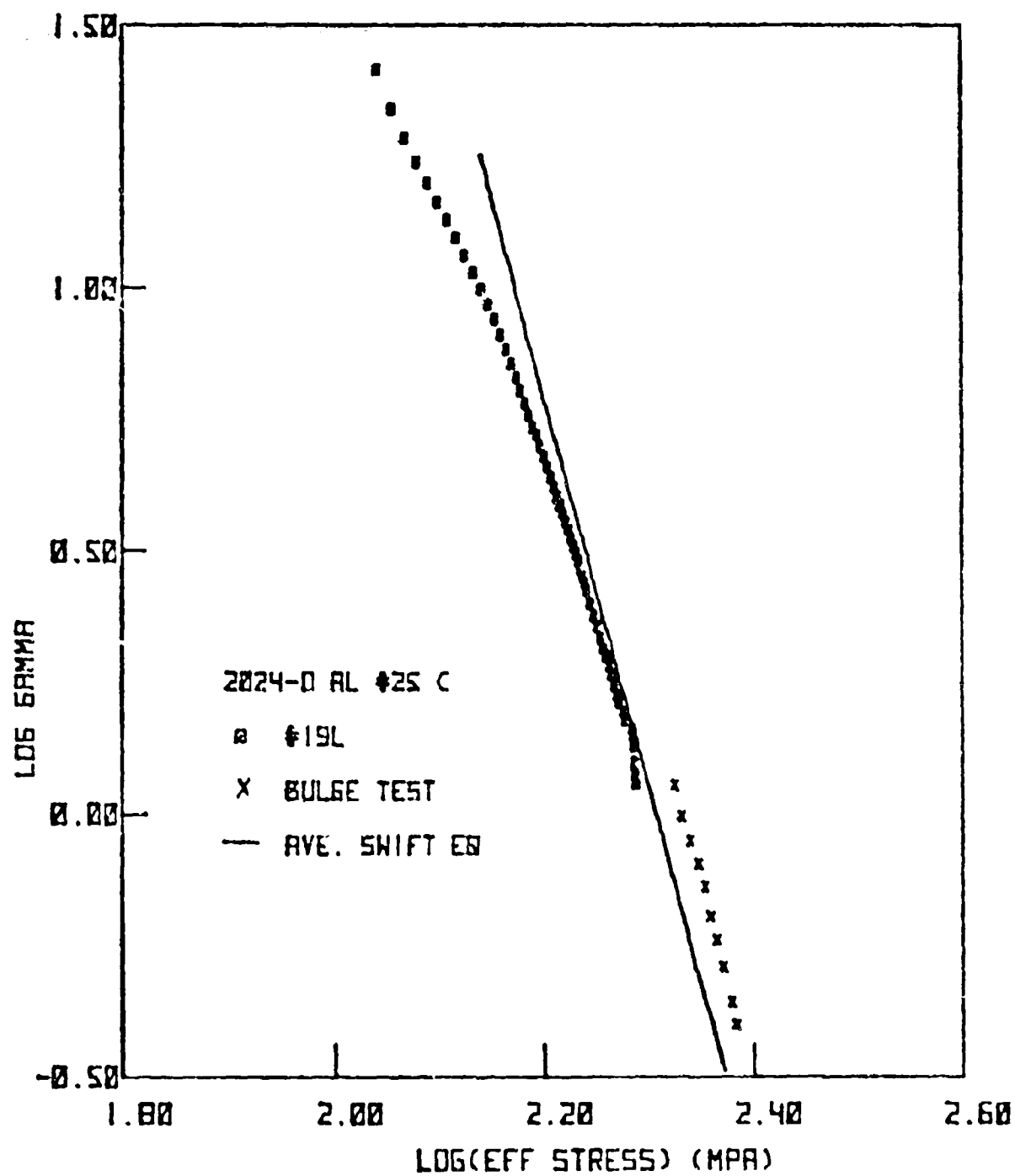


FIGURE 13. COMPARISON OF EXTRAPOLATED TENSILE STRAIN HARDENING BEHAVIOR WITH THE BULGE TEST FOR 2024-O ALUMINUM AT 25°C

stress σ and the strain rate sensitivity

$$v = (\partial \ln \sigma / \partial \ln \dot{\epsilon})_T \quad (5-7)$$

on strain rate and temperature. For the load relaxation tests, the specimen was loaded to a plastic strain of approximately 1% at a strain rate of 10^{-2} sec^{-1} . During loading and initial relaxation, load readings were taken at a rate of approximately 15 per second. The data acquisition system was programmed to reduce this rate incrementally during the tests which lasted from 2 to 5 hours. The load-time data was processed to calculate true stress $\bar{\sigma}$ and strain rate $\dot{\epsilon}$ at a subset of load intervals separated by approximately equal load increments. The results are presented as $\log \bar{\sigma}$ vs. $\log \dot{\epsilon}$ plots termed hardness curves. Since the strain accumulated during a load relaxation test is very small, the hardness curve represents a specimen at essentially constant structure, and the slope of the hardness curve is the strain rate sensitivity v .

The hardness curve for a 2024-0 aluminum sample obtained at 25°C is shown in Fig. 14. The slope of the hardness curve is essentially independent of strain rate and gives a strain rate sensitivity $v = 3 \times 10^{-3}$. This small value of v is in general agreement with the lack of strain rate dependence of the flow stress determined for the constant extension rate tests at 25°C. For example, if a factor $\dot{\epsilon}^v$ had been included in Eq. (5-7), its variation over the strain rate range of 10^{-5} to 10^{-1} sec^{-1} would be only 2 percent.

Hardness curves determined on another 2024-0 specimen at 4 different temperatures are shown in Fig. 15. These tests were all run on the same specimen at decreasing temperatures. Approximately 1 to 2 percent plastic strain was accumulated for each test prior to the relaxation. Hence, each hardness curve may represent a different hardness state and the shapes, rather than the relative stress levels, provide the useful information. It is seen that, in general, the strain rate sensitivity v increases with increasing temperature and decreasing strain rate. At 163°C and 225°C, the hardness curves have an inflection point, and the strain rate sensitivity decreases with strain rate below a strain rate of approximately 10^{-6} sec^{-1} . These temperatures represent approximately 0.48 and 0.54 of the melting point of the alloy, respectively, which is a temperature range where one expects grain boundary sliding to contribute to the deformation. Previous studies [36,37] have shown that

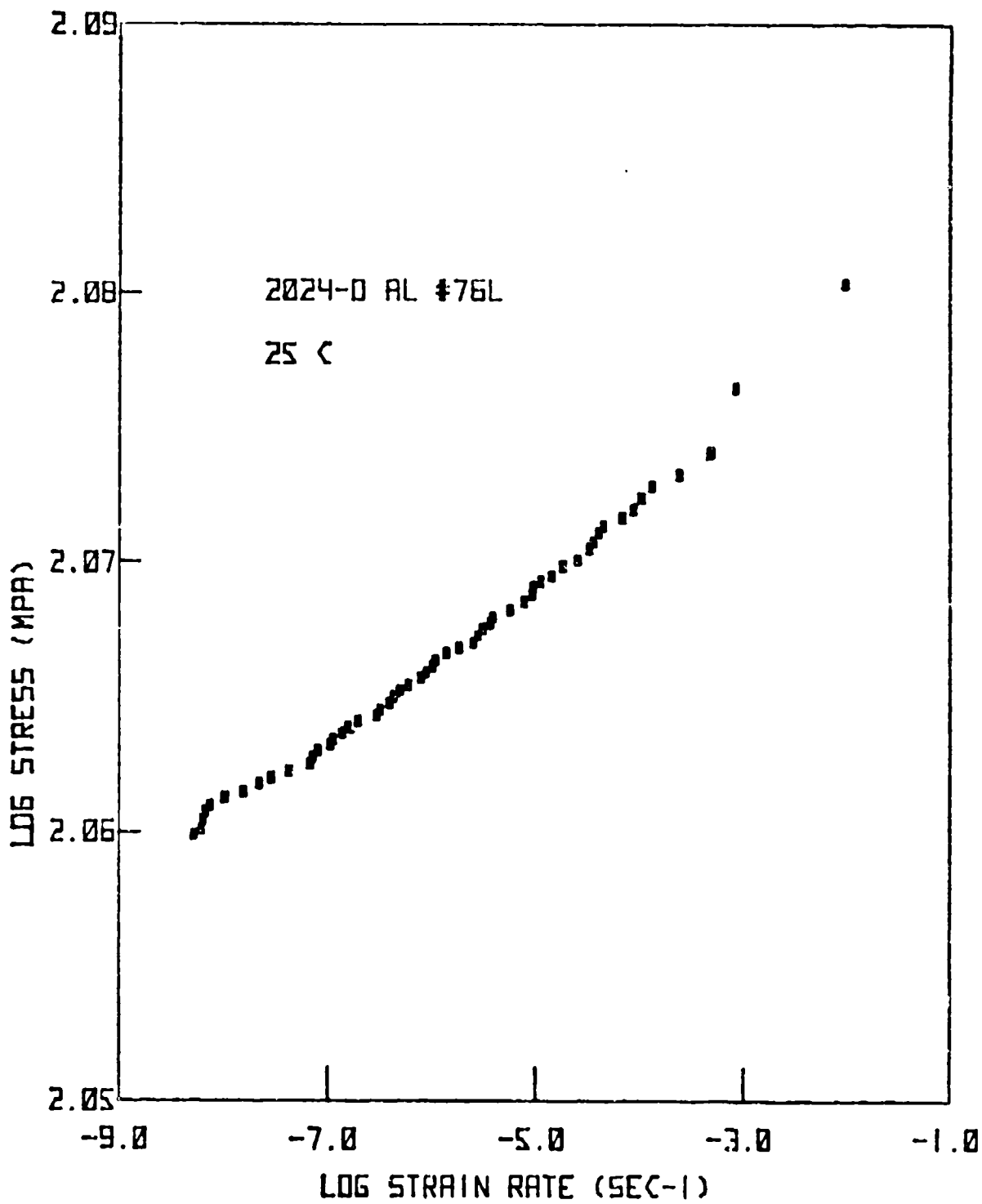


FIGURE 14. STRESS RELAXATION HARDNESS CURVE LOG σ vs. LOG $\dot{\epsilon}$
FOR 2024-O ALUMINUM AT 25°C

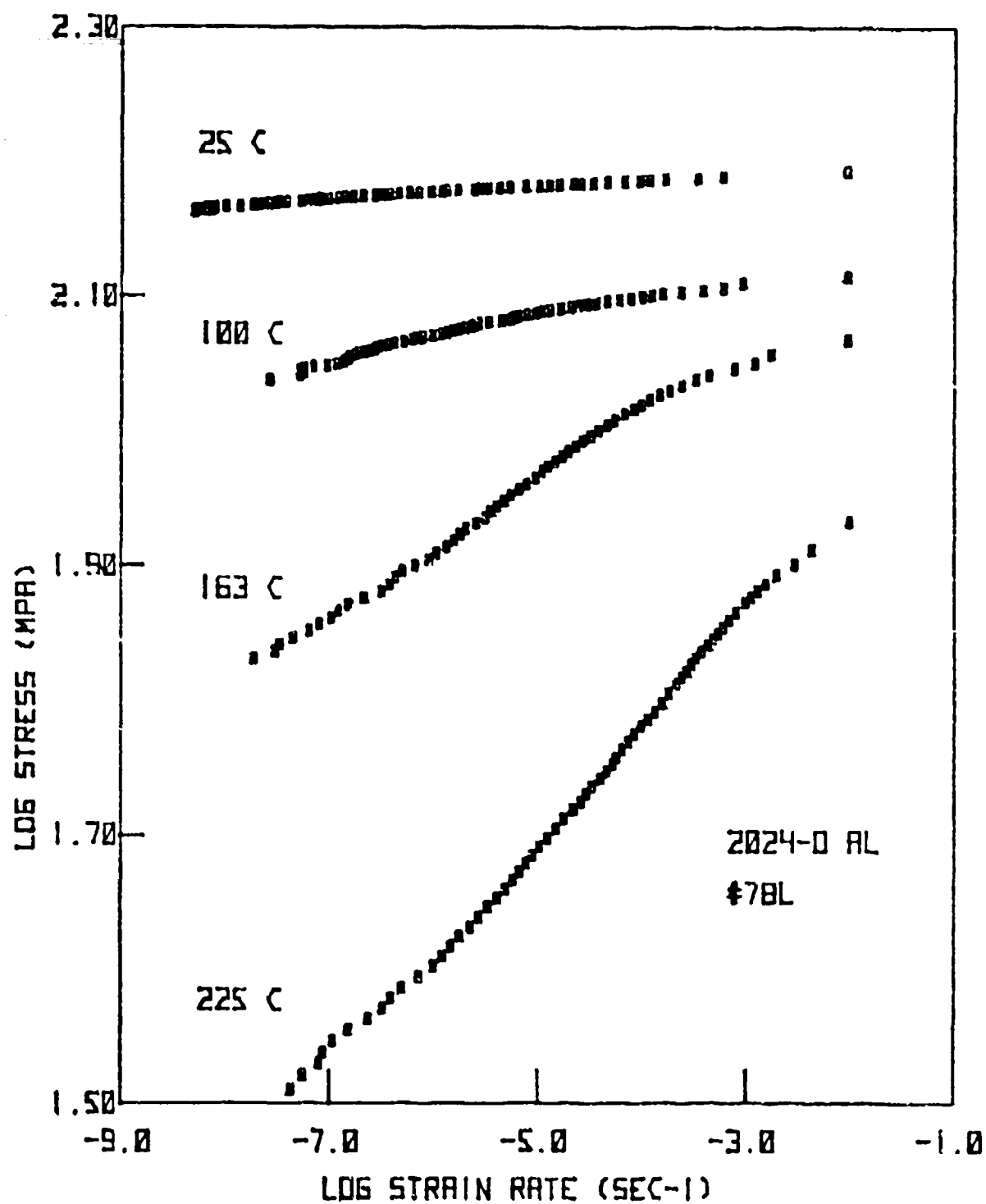


FIGURE 15. STRESS RELAXATION HARDNESS CURVES vs. TEMPERATURE
FOR 2024-O ALUMINUM

grain boundary sliding can lead to a hardness curve with an inflection point at intermediate strain rates, and it is thought that grain boundary sliding determines the dependence of the strain rate sensitivity on strain rate at 163°C and 225°C for 2024-O aluminum.

Since the hardness curve at 163°C is of interest in regard to the interpretation of the strain hardening data at this temperature, it is shown expanded in Fig. 16. The maximum strain rate sensitivity is $n = 6 \times 10^{-2}$ at $\dot{\epsilon} = 10^{-5} \text{ sec}^{-1}$, and n may decrease by up to a factor of 10 as the strain rate increases to 10^{-1} sec^{-1} . This is reminiscent of the strain rate dependence of the flow stress and strain hardening coefficient γ , but a detailed model is required to make the comparison quantitative. In summary, the load relaxation tests have provided interesting information on the strain rate dependence but further development of constitutive equations is required.

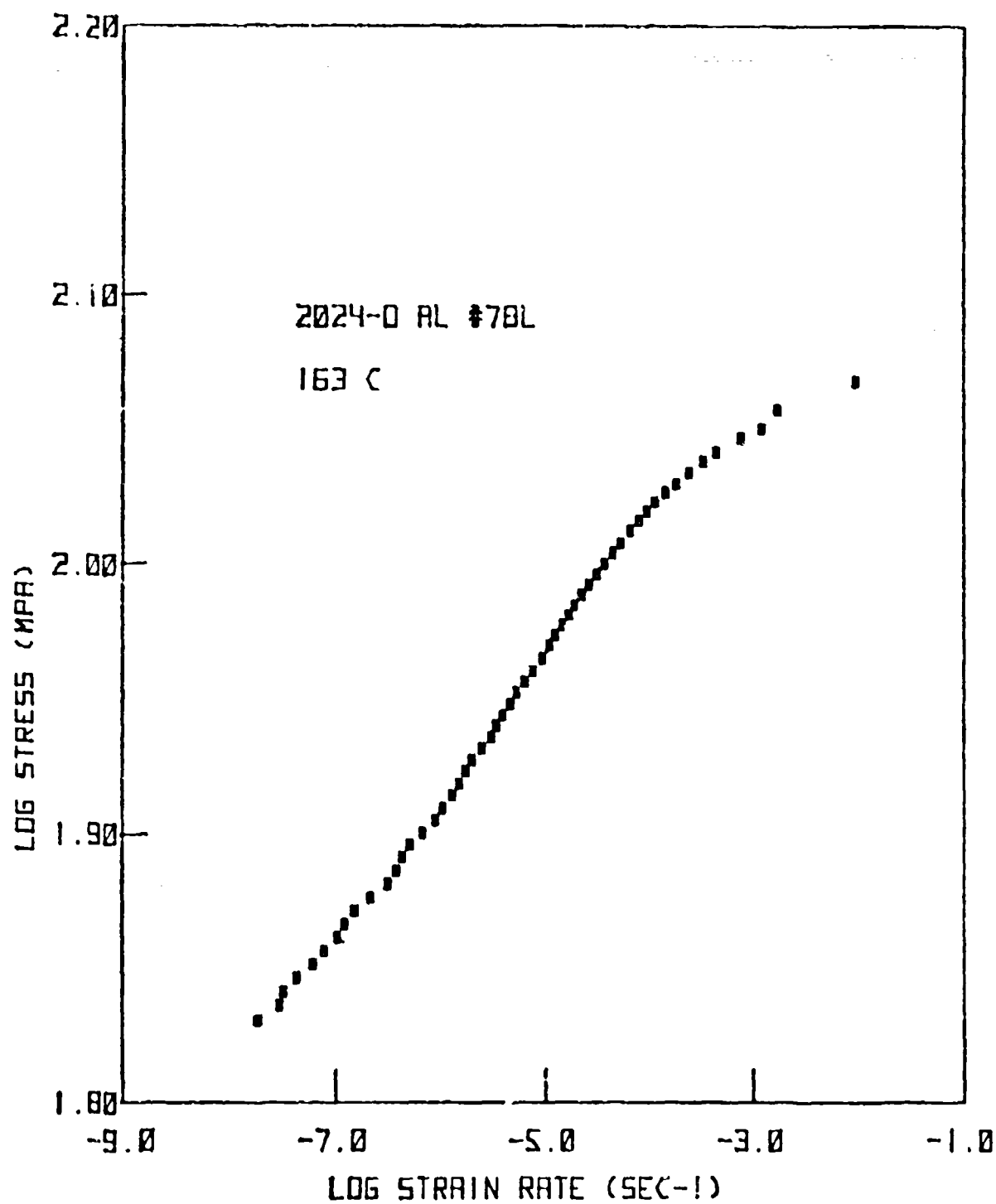


FIGURE 16. STRESS RELAXATION HARDNESS CURVE FOR 2024-O ALUMINUM AT 163°C

6. RESULTS FOR Ti-6Al-4V

6-1 Constant Extension Rate Tests

Stress-strain curves and tensile test parameters - sheet. Constant extension rate tests were performed on the Ti-6Al-4V test specimens cut from the RMI sheet described in sec. 4.1 at 25°C and strain rates of 10^{-5} to 10^{-1} sec^{-1} . In addition, some tensile test results were available from work performed at the University of Kentucky (UK) [4] at 25°C, 538°C (1000°F), and 677°C (1250°F). The 1250°F temperature is within the warm forming range for Ti-6Al-4V. However, some preforming is done at room temperature, and the 25°C tensile data is relevant for this application.

The 25°C tensile tests were performed on 0°(L) specimens at strain rates of 10^{-5} to 10^{-1} sec^{-1} and on 90°(T) and 45°(F) specimens at strain rates of 10^{-4} to 10^{-2} sec^{-1} . A typical Instron chart record obtained on an L specimen at 10^{-3} sec^{-1} is shown in Fig. 17. The load-elongation curve shows very little strain hardening. There is a mild yield point effect followed by a slight rise to a maximum load. In general, the strain hardening was largest at the lowest strain rates. At 10^{-2} sec^{-1} and above, the load tended to fall off continuously after yielding. The thickness strain transducer was used for these tests, and it is seen that the transducer output is smooth and nearly linear.

The load-elongation curves have been used to compute standard tensile test parameters vs. strain rate. These are presented in Table 9. The engineering stress at the yield point σ_y is recorded instead of a 0.2 percent yield stress. Both the yield point stress σ_y and the ultimate tensile stress σ_{UTS} increase steadily with strain rate. Both the uniform strain ϵ_{unif} and the total elongation ϵ_{tot} decrease with increasing strain rate in a manner such that the post-uniform elongation is nearly constant. The stress values are nearly independent of orientation with those for the F specimens being about 2 percent less than those for the L and T specimens. The σ_{UTS} values are in excellent agreement with average values determined by Batelle [4] (L: 1014 MPa T: 1005 MPa) at a strain rate of $1.67 \times 10^{-3} \text{ sec}^{-1}$.

The variation in tensile properties with strain rate is also illustrated in Fig. 18 by the true stress-true strain curves (up to ϵ_{unif}) for the four L specimens tested at strain rates $\dot{\epsilon} \leq 10^{-2} \text{ sec}^{-1}$. It is seen that the stress

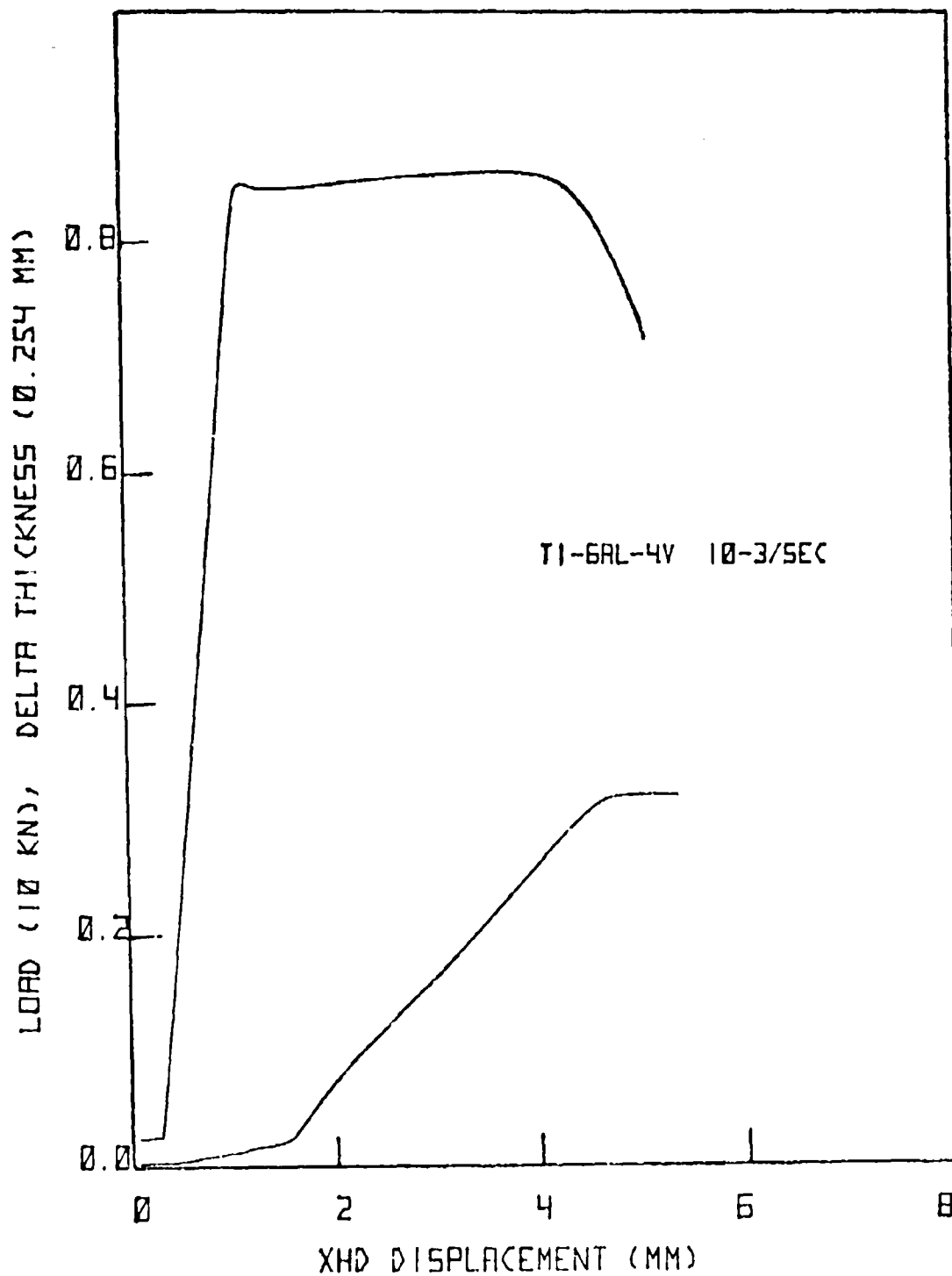


FIGURE 17. LOAD vs. ELONGATION AND CHANGE IN THICKNESS vs. ELONGATION FOR Ti-6Al-4V SHEET AT 25°C AND 10^{-3} sec^{-1}

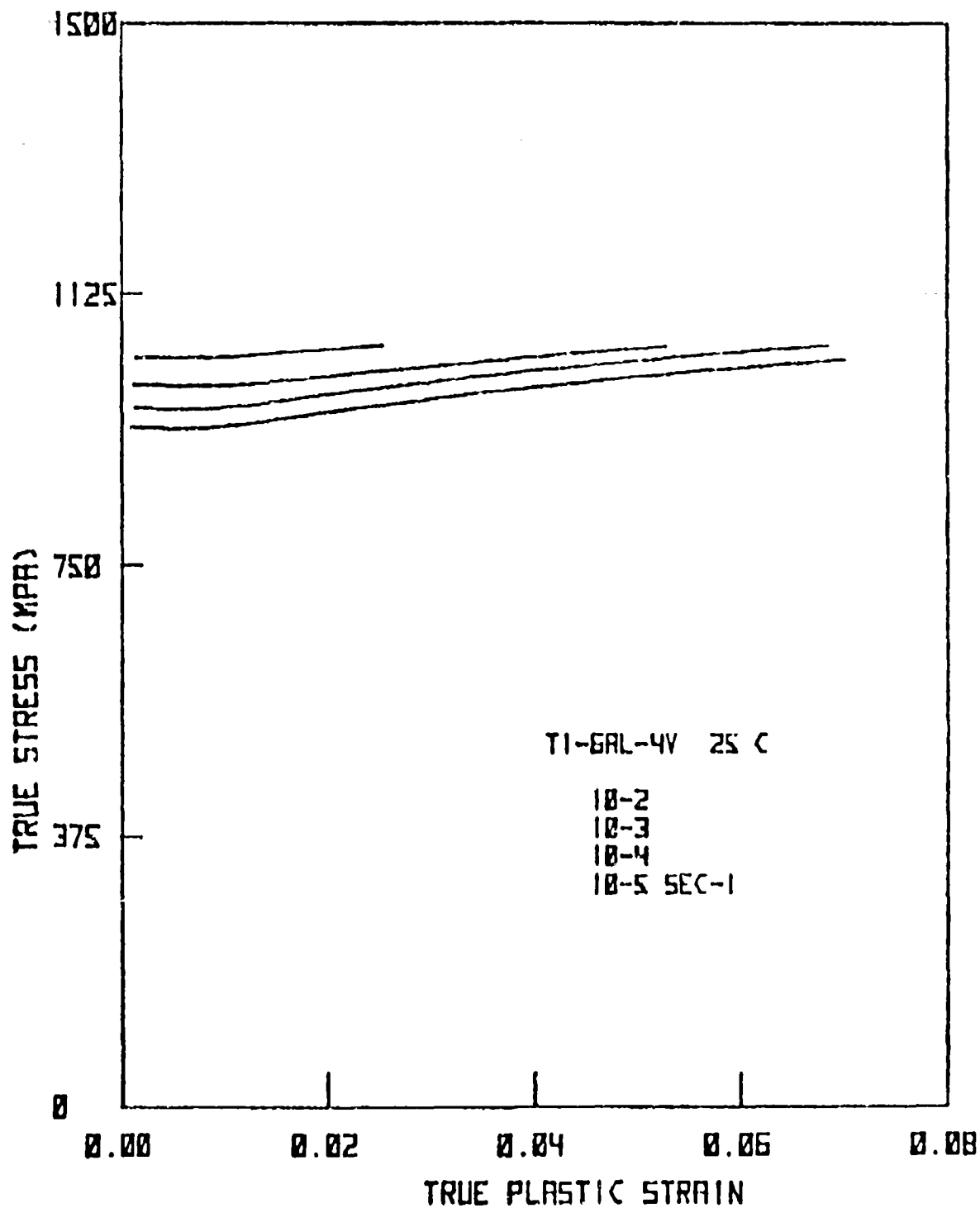


FIGURE 18. TENSILE TRUE STRESS - TRUE STRAIN CURVES FOR Ti-6Al-4V SHEET AT 25°C vs. STRAIN RATE

TABLE 9. TENSILE TEST PARAMETERS FOR
Ti-6Al-4V SHEET AT 25°C

Specimen	Rate (sec^{-1})	σ_u (MPa)	σ_{UTS} (MPa)	ϵ_{unif}	$\epsilon_{tot}(\%)$
24L	10^{-1}	1064.5	--	--	8.2
25L	10^{-2}	1035.6	1029.1	0.025	10.1
26L	10^{-3}	998.1	1000.0	0.053	12.4
27L	10^{-4}	965.6	985.7	0.069	12.7
28L	10^{-5}	938.1	965.5	0.070	13.4
17T	10^{-2}	1033.0	--	--	6.9
16T	10^{-3}	999.0	996.4	0.040	10.3
18T	10^{-4}	972.5	983.3	0.057	11.8
18F	10^{-2}	1018.7	--	--	9.5
17F	10^{-3}	987.6	978.1	0.025	13.2
19F	10^{-4}	956.8	960.0	0.049	13.1

strain curves are nearly parallel.

Tensile data on specimens cut from the same Ti-6Al-4V sheet has also been obtained at UK in a parallel study. Their true stress-true strain curves vs. temperature and strain rate are shown in Fig. 19 and Fig. 20 taken from reference [4]. In general, the flow stresses decrease and total elongations increase with increasing temperature and decreasing strain rate. The room temperature stress-strain curves at 10^{-2} and 10^0 sec^{-1} are considered anomalous.

Stress-strain curves and tensile test parameters - bar. Since the Ti-6Al-4V sheet work hardens very little, some tensile tests on Ti-6Al-4V

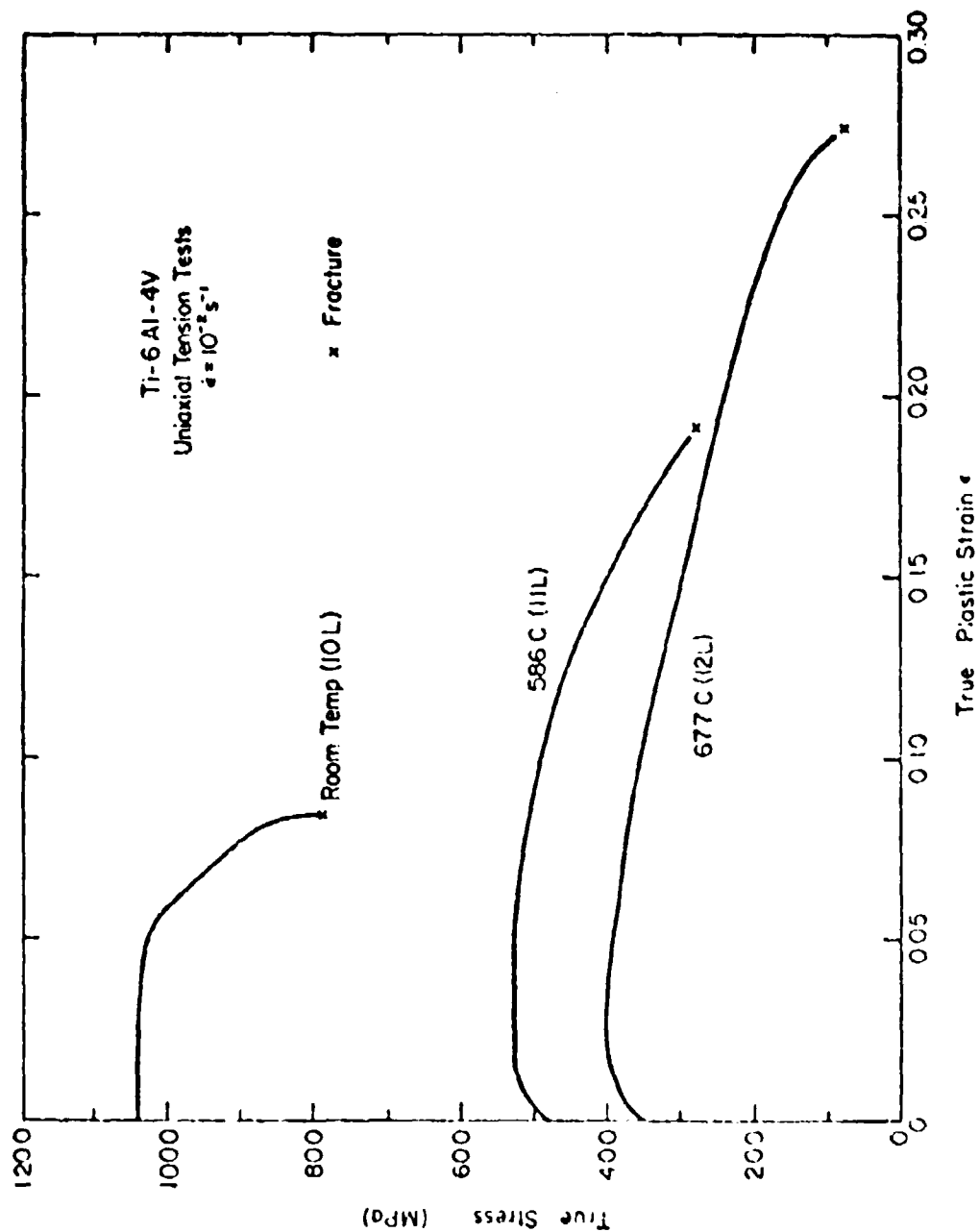


FIGURE 19. TRUE STRESS - TRUE STRAIN CURVES FOR Ti-6Al-4V SHEET VS. TEMPERATURE AT 10^{-2} sec^{-1} . FROM [4]

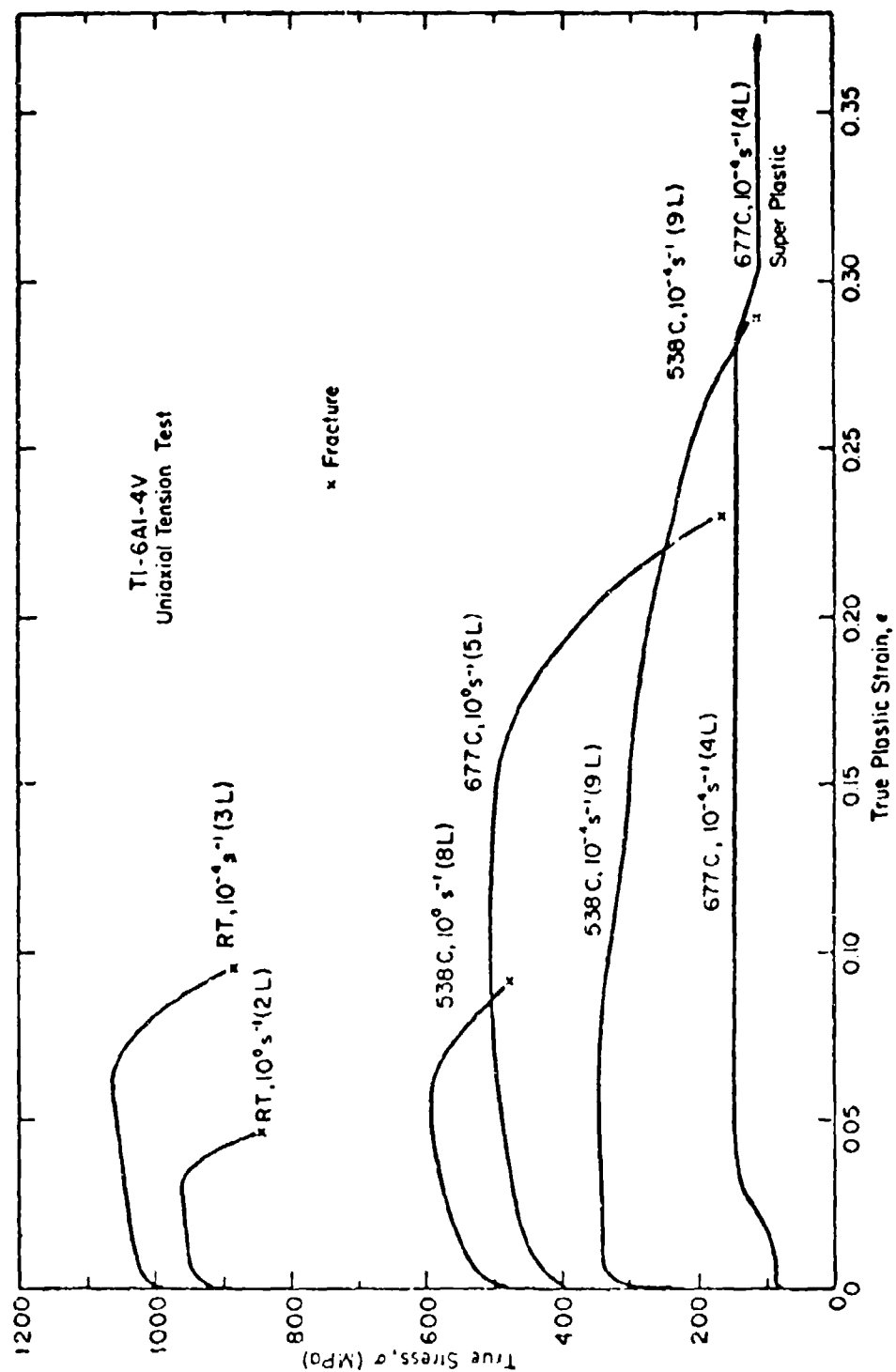


FIGURE 20. TRUE STRESS- TRUE STRAIN CURVES FOR Ti-6Al-4V SHEET VS. TEMPERATURE AT 10^0 AND 10^{-4} sec^{-1} . FROM [4]

bar performed for a previous study will be reexamined here. These tests were run on button-head specimens at a strain rate of 10^{-2} sec^{-1} and at temperatures of 25°, 200°, 350°, and 500°C. An Instron chart record obtained at 25°C showing load vs. elongation is shown in Fig. 21 and the true stress-true strain curves (up to ϵ_{unif}) for all four temperatures are shown in Fig. 22. It is seen that the strain hardening is significantly greater for the bar specimens than for the sheet specimens. In fact, the load-elongation curves for the sheet specimens look very much like those for bar specimens that have been subjected to a 1 or 2 percent tensile prestrain [29]. This is consistent with the observation that the sheet material has not been fully annealed.

The tensile test parameters for the bar specimens vs. temperature are shown in Table 10. At 25°C, the yield stress σ_y is smaller and the ultimate stress σ_{UTS} is larger than for the sheet material.

TABLE 10. TENSILE TEST PARAMETERS FOR
Ti-6Al-4V BAR AT 10^{-2} sec^{-1} .

Temperature	σ_y (MPa)	σ_{UTS} (MPa)	ϵ_{unif}	ϵ_{tot} (%)
25°C	932.2	1056.1	0.045	15.1
200°C	689.8	861.3	0.048	14.9
350°C	626.2	789.2	0.054	14.8
500°C	566.0	674.5	0.054	17.9

Plastic Anisotropy. In the parallel study on the Ti-6Al-4V sheet at UK [4], extensive work was done on measurement of r-values vs. orientation, strain, strain rate, and temperature. The r-values were determined by measuring changes in dimension of 0.05 inch square grids that had been etched on the flat surface of the tensile specimen prior to testing. The UK results at room temperature and 3 percent strain are shown as a function of orientation and strain rate in Table 11. The r-values range from 0.49 to 0.80. The scatter is quite large, and no definite patterns regarding dependence

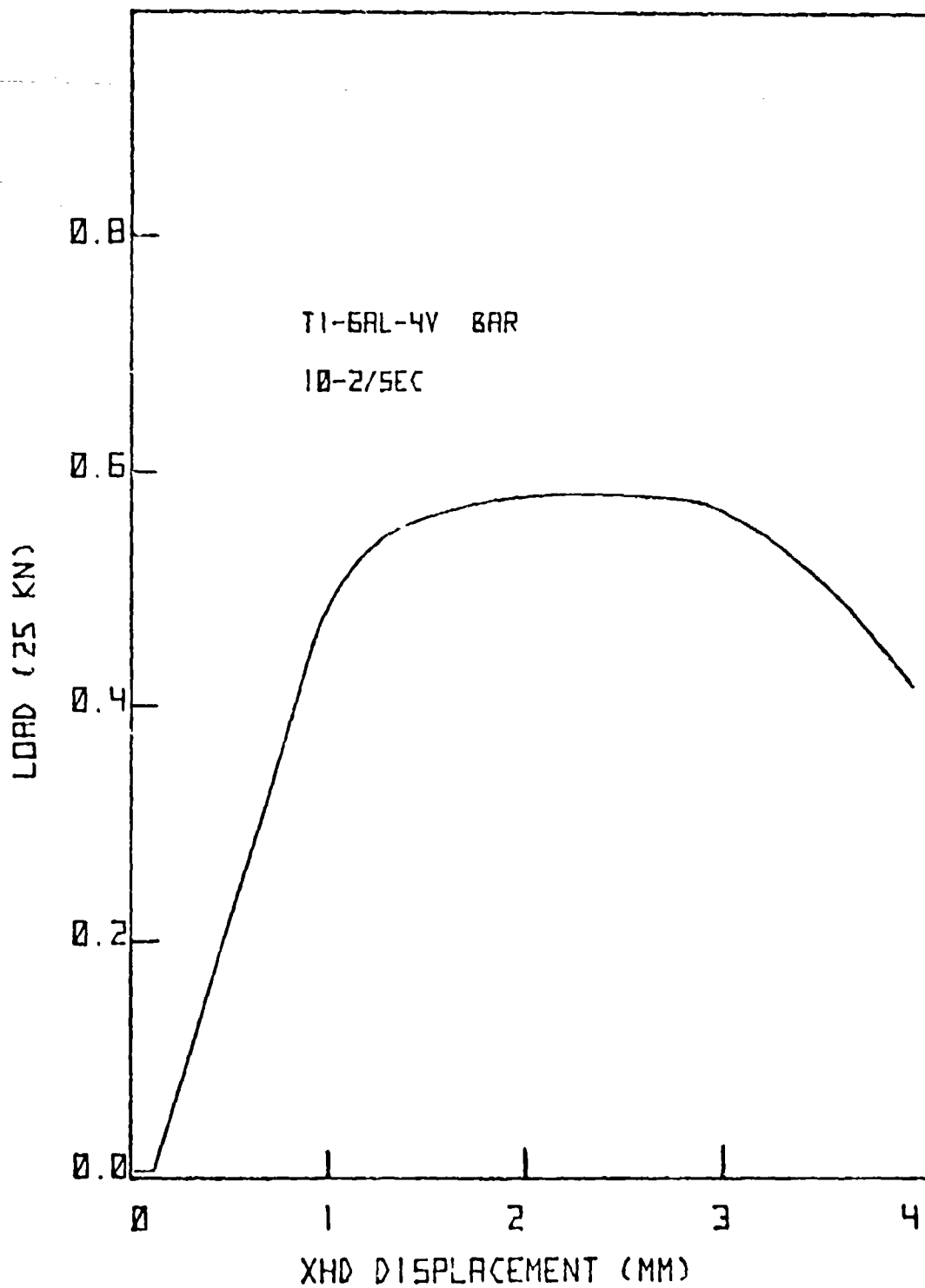


FIGURE 21. LOAD vs. ELONGATION FOR Ti-6Al-4V BAR AT 25°C
AND 10^{-2} sec^{-1}

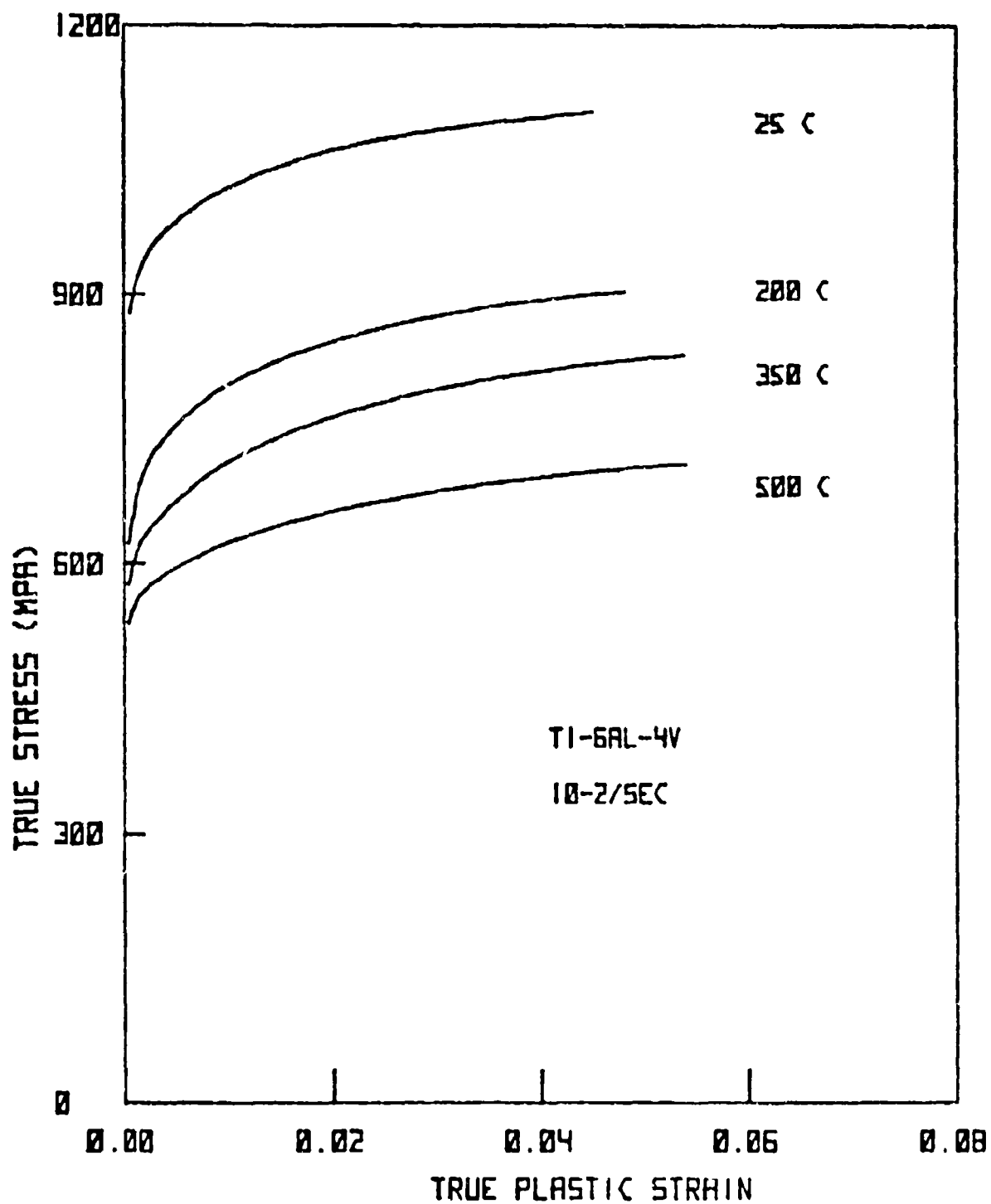


FIGURE 22. TENSILE TRUE STRESS - TRUE STRAIN CURVES FOR Ti-6Al-4V BAR AT 10^{-2} sec^{-1} vs. TEMPERATURE.

on strain rate or orientation emerge. However, it was shown that the r -values increased substantially with strain, increasing from ~ 0.3 at yield to ~ 1.0 at a true strain of 0.1.

TABLE 11. R -VALUES FOR Ti-6Al-4V SHEET
AT ROOM TEMPERATURE. FROM [4].

Orientation	at 10^0 (sec $^{-1}$)	at 10^{-2} (sec $^{-1}$)	at 10^{-4} (sec $^{-1}$)
r_0	0.51-0.55	0.58-0.69	0.60-0.64
r_{90}	0.51-0.52	0.52-0.54	0.50-0.51
r_{45}	0.59-0.80	0.70-0.73	0.49-0.58

Measurements in our laboratory based upon the transverse strain sensor output also showed significant scatter. Using Eq. 4-2, measured r -values ranged from 0.33 to 0.74 with no definite dependence on strain rate or orientation. It is interesting to note (Fig. 17) that the slope of the transverse strain sensor output decreases over the first ~ 1 percent plastic strain and then is nearly constant through the maximum load point. Eq. (4-2) can be written

$$r = \left(\frac{dt}{dc} \right)^{-1} \frac{t}{c} - 1 \quad (6-1)$$

where dt is the decrease in thickness and dc the increase in gauge length. The derivative dt/dc is the slope observed in Fig. 17. Eq. (6-1) together with the observed transverse strain sensor output imply that the r -value should increase over the first ~ 1 percent strain and then decrease as the ratio (t/c) decreases. This is contrary to the observations on the gridded specimens, and the discrepancy is not understood.

As a final comment, it is noted that the yield point stress σ_y and ultimate stress σ_{UTS} are nearly independent of orientation at fixed strain rate (Table 9), with the stresses for the F specimens slightly less (1.5 - 2.5 percent) than those for the L and T specimens. If the Hill

theory for anisotropy holds, this would imply that r_{45} would be slightly greater than r_0 and r_{90} . This is suggested but not clearly demonstrated by the measured r -values.

In summary, the plastic anisotropy of the Ti-6Al-4V sheet is characterized by approximate isotropy within the plane of the sheet (normal anisotropy) with an average r -value of approximately 0.6.

Strain hardening behavior - bar. Since the Ti-6Al-4V sheet material used in this investigation strain hardens very little, the strain hardening behavior of the annealed bar will be examined first. The method of analysis will be the same as that used for the 2024-0 aluminum in sec. 5.

A plot of $\log \gamma$ vs. $\log \sigma$ for the 25°C specimen of Table 10 is shown in Fig. 23. The shape of the curve is clearly of the same form as those obtained for 2024-0 aluminum. Again, $\log \gamma$ decreases linearly with $\log \sigma$ at large stress. Reference to the stress-strain curve indicates that this linear portion begins at approximately 2 percent strain. The straight line fit to this portion of the $\log \gamma$ vs. $\log \sigma$ data is also shown in Fig. 23. Using the parameter for this line and the stress-strain data, the Swift equation for the large strain portion of the tensile stress-strain curve is

$$\sigma \text{ (MPa)} = 1239 (-0.008 + \epsilon)^{0.035} \quad (6.2)$$

It is emphasized that this equation only holds at 25°C and a strain rate of 10^{-2} sec^{-1} . The strain rate dependence at 25°C has not been investigated. The stress-strain curve and Swift equation fit are shown in Fig. 24. The predicted uniform strain $n-\epsilon_0 = 0.043$ agrees closely with the measured value of $\epsilon_{unif} = 0.045$.

The portion of the $\log \gamma$ vs. $\log \sigma$ plot corresponding to strains from approximately 0.005 to 0.020 ($\log \gamma = 0.5$ to 1.0) can also be fit by a straight line. The strain hardening exponent for this portion is $n = 0.06$. For strains less than 0.005, the $\log \gamma$ vs. $\log \sigma$ data rises above this straight line due to a transient strain contribution.

The strain hardening behavior of the Ti-6Al-4V bar was also investigated for the elevated temperature runs in terms of $\log \gamma$ vs. $\log \sigma$.

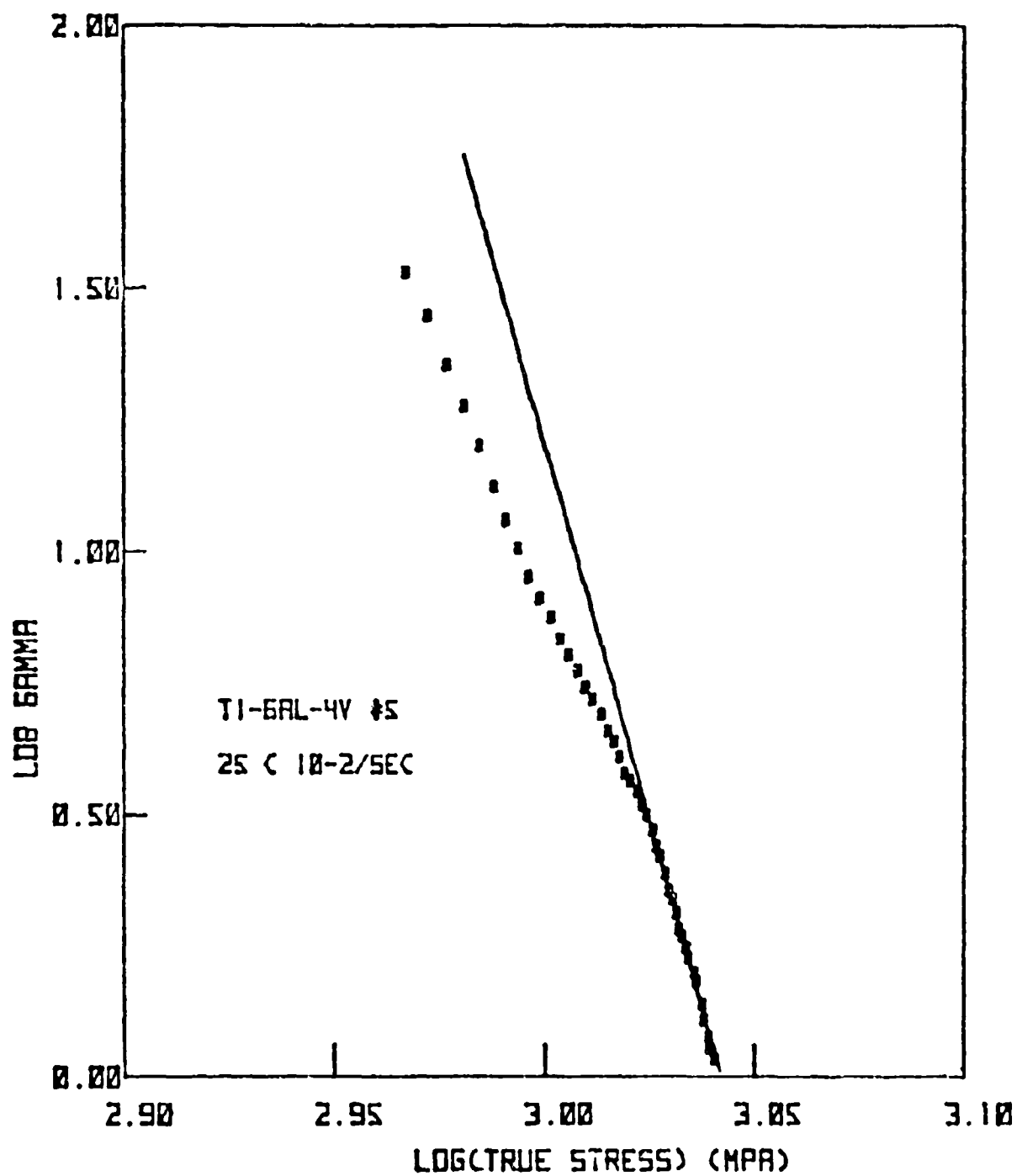


FIGURE 23. STRAIN HARDENING BEHAVIOR PRESENTED AS LOG γ vs. LOG σ FOR Ti-6Al-4V BAR AT 25°C AND 10^{-2} sec $^{-1}$

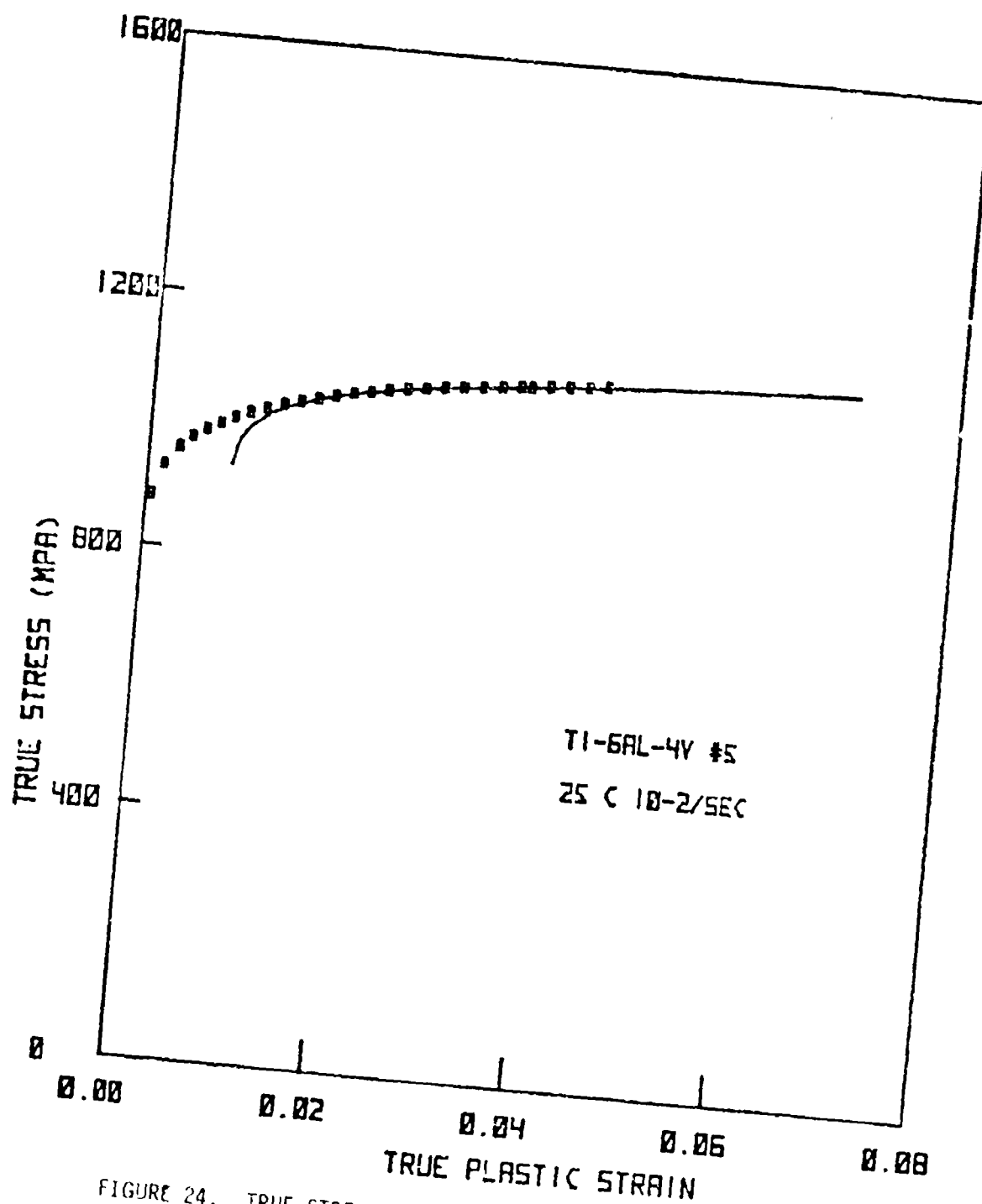


FIGURE 24. TRUE STRESS - TRUE STRAIN CURVE WITH SWIFT EQUATION
FIT FOR Ti-6Al-4V BAR AT 25°C AND 10⁻² sec⁻¹

Although these plots had generally the same shape as that for 25°C, it was more difficult to identify a high stress linear portion. This is illustrated by the plot for the 500°C tensile test in Fig. 25. Since the identification of a straight line segment is not clear, the modeling procedure for the high temperature data will not be reported.

It is significant that the strain hardening behavior characterized by a linear dependence of $\log \gamma$ on $\log \epsilon$ has been observed for both 2024-0 aluminum and Ti-6Al-4V, alloy systems with significantly different structure and properties.

Strain hardening behavior - sheet. It was possible to analyze the strain hardening behavior for the Ti-6Al-4V sheet material in terms of $\log \gamma$ vs. $\log \epsilon$ for those tensile tests that exhibited a maximum load. These results will be summarized for the four L specimens tested at strain rates of 10^{-5} to 10^{-2} sec^{-1} .

The $\log \gamma$ vs. $\log \epsilon$ plot for the test run at 10^{-4} sec^{-1} is shown in Fig. 26. It is essentially a straight line over the entire range of stresses. The points begin at a strain $\epsilon = 0.015$ chosen to avoid the region of minimum stress which follow the yield point. Straight lines were fit to the $\log \gamma$ vs. $\log \epsilon$ data corresponding to strains greater than 2 percent (1.5 percent for the 10^{-2} sec^{-1} test). The stress-strain curve and the Swift equation fit for the 10^{-4} sec^{-1} test is shown in Fig. 27. The fit is excellent over the entire range of strain.

The Swift equation parameters for the four L specimens are summarized in Table 12. The n values are nearly independent of strain rate with an average value $n=0.106$. This is higher than either the low strain (0.06) or high strain (0.035) values for the annealed bar. The ϵ_0 values increase with strain rate so as to account for the decrease in uniform strain. Again, the agreement between calculated and measured uniform strains is very good. The k values generally increase with strain rate.

In summary, the strain hardening behavior of the Ti-6Al-4V sheet can be described by a single Swift equation over the entire range of strain past the initial yield point. Although an average n value could be used, the ϵ_0 and k values depend upon strain rate.

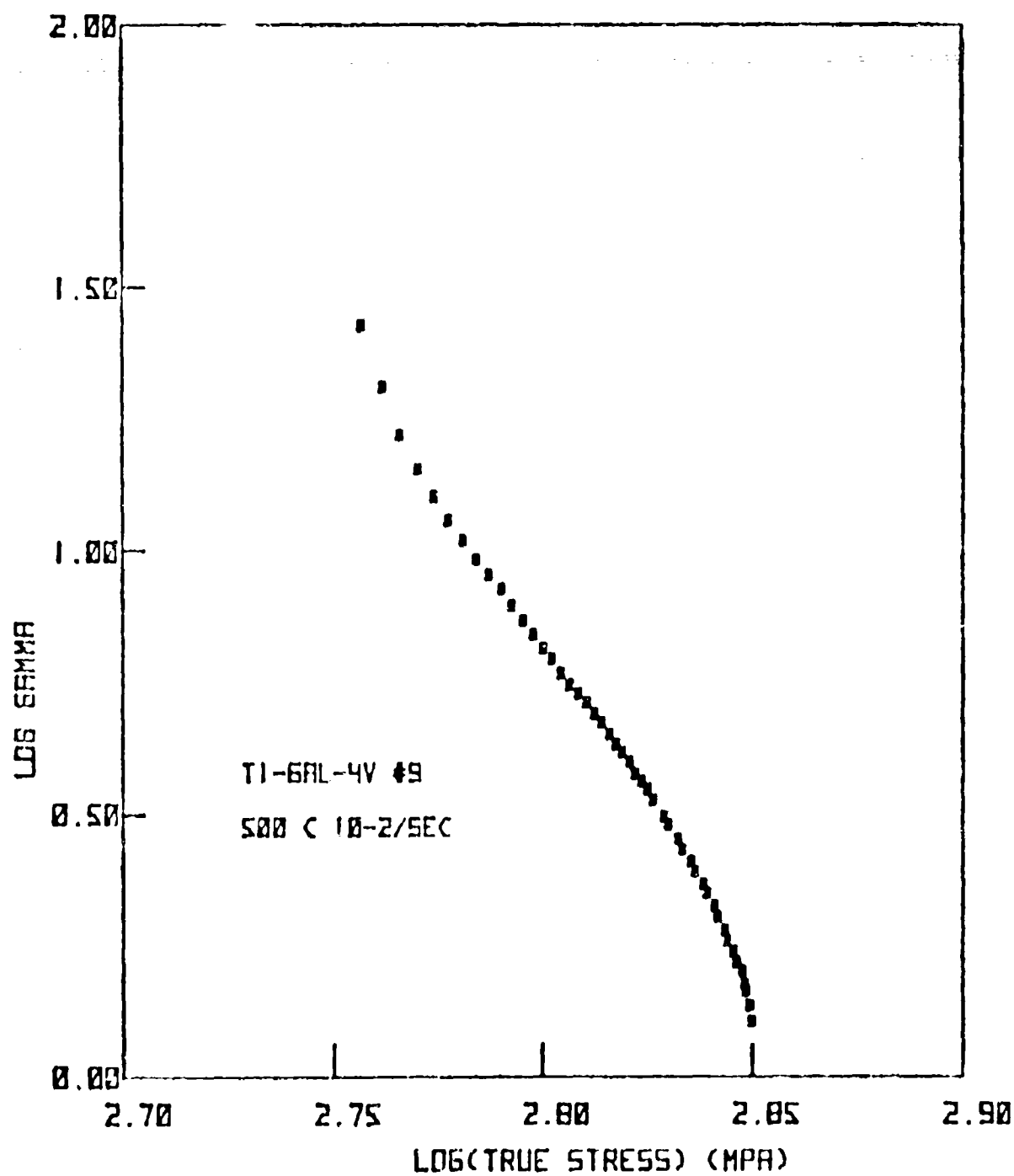


FIGURE 25. STRAIN HARDENING BEHAVIOR PRESENTED AS LOG ϵ vs. LOG σ FOR Ti-6Al-4V BAR AT 500°C AND 10^{-2} sec $^{-1}$

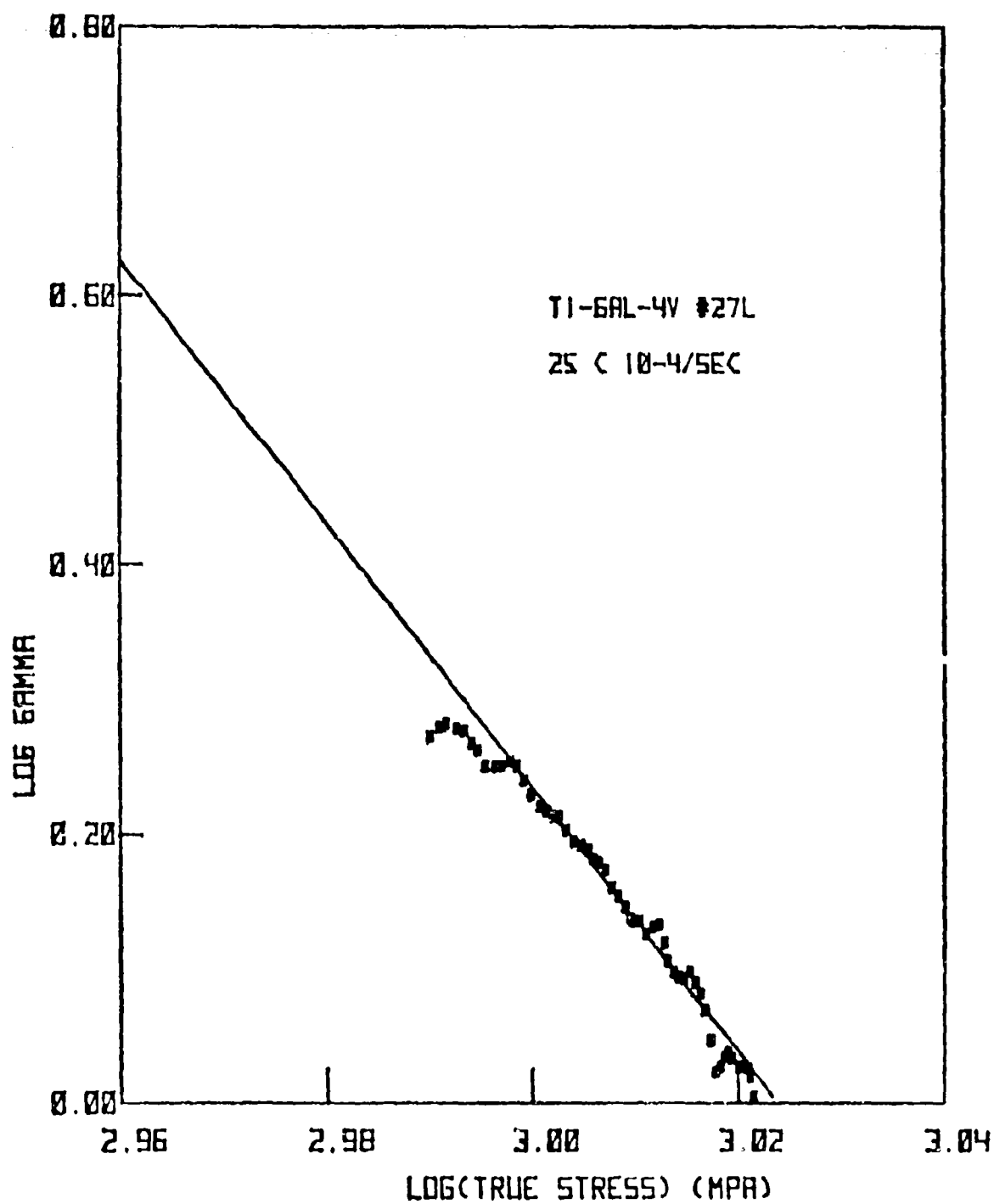


FIGURE 26. STRAIN HARDENING BEHAVIOR PRESENTED AS LOG γ vs. LOG σ FOR Ti-6Al-4V SHEET AT 25°C AND 10⁻⁴ sec⁻¹

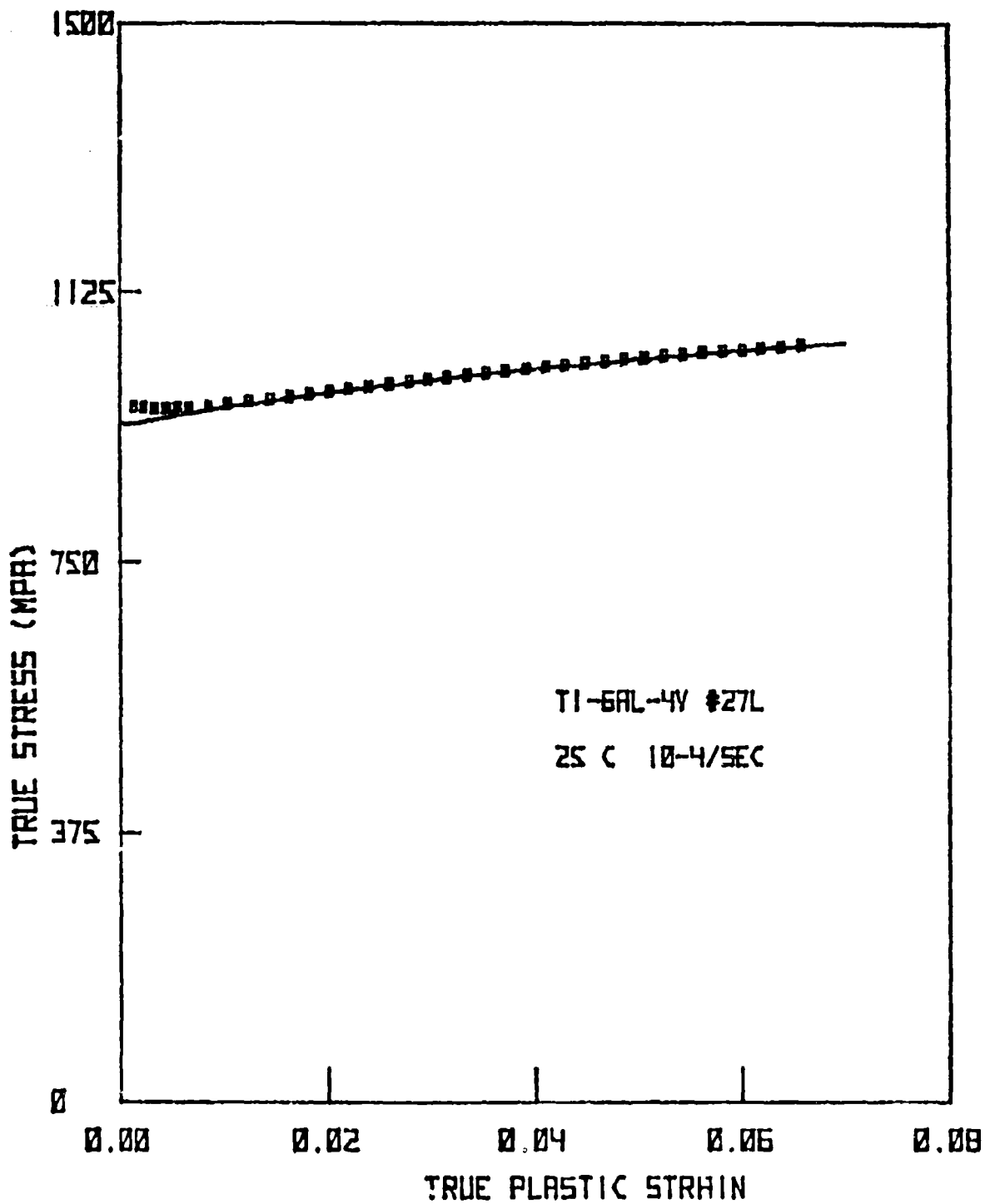


FIGURE 27. TRUE STRESS - TRUE STRAIN CURVE WITH SWIFT EQUATION FIT
FOR Ti-6Al-4V SHEET AT 25°C AND 10⁻⁴ sec⁻¹

TABLE 12. SWIFT EQUATION PARAMETERS FOR
Ti-6Al-4V SHEET AT 25°C.

Specimen	Rate (sec ⁻¹)	n	ϵ_0	k(MPa)	n- ϵ_0	ϵ_{unif}
25L	10 ⁻²	0.093	0.073	1310	0.020	0.025
26L	10 ⁻³	0.121	0.063	1367	0.058	0.053
27L	10 ⁻⁴	0.102	0.033	1334	0.069	0.069
28L	10 ⁻⁵	0.106	0.031	1322	0.075	0.070

6.2 Load Relaxation Tests.

Variation with temperature - bar. Load relaxation tests have been performed to determine the dependence of the flow stress and strain rate sensitivity on strain rate and temperature for the annealed bar material. Six load relaxation tests were performed on a single specimen at decreasing temperatures of 500°, 425°, 350°, 275°, 200°, and 25°C. The hardness curves are shown in Fig. 28 and the four runs at the intermediate temperatures are shown on a more expanded scale in Fig. 29. These hardness curves illustrate the change from low temperature to high temperature grain matrix deformation behavior suggested by Hart [15]. For the strain rates sampled, the transition occurs at 350°C. At temperatures below 350°C, the strain rate sensitivity is small and increases with increasing strain rate at each temperature. A typical value would be $v = 0.01$ at 25°C and 10^{-4} sec⁻¹. At temperatures above 350°C, the strain rate sensitivity is large at low strain rates and decreases with increasing strain rate. At 500°C and 10^{-5} sec⁻¹, it is $v = 0.10$. At 350°C the strain rate sensitivity passes through a minimum value of $v = 2 \times 10^{-3}$ at a strain rate of 10^{-5} sec⁻¹. It is expected that each of the hardness curves in Fig. 28 could be fit by Eq. (2-6) for constant values of λ and M . The parameters σ^* and σ^0 would increase as strain is accumulated from run to run and σ^* would carry the major temperature dependence.

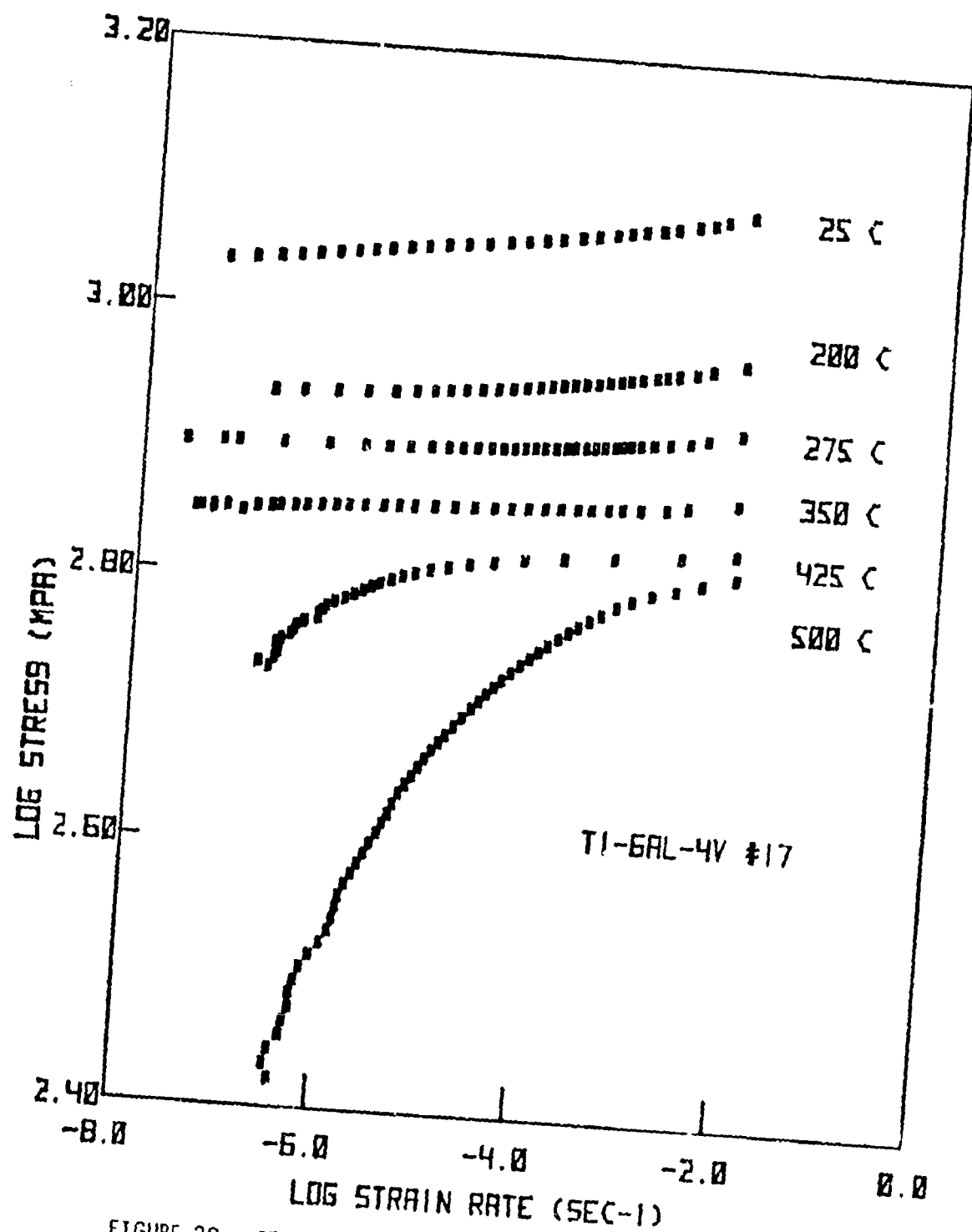


FIGURE 28. STRESS RELAXATION HARDNESS CURVES vs. TEMPERATURE
(25°C - 500°C) FOR Ti-6Al-4V BAR

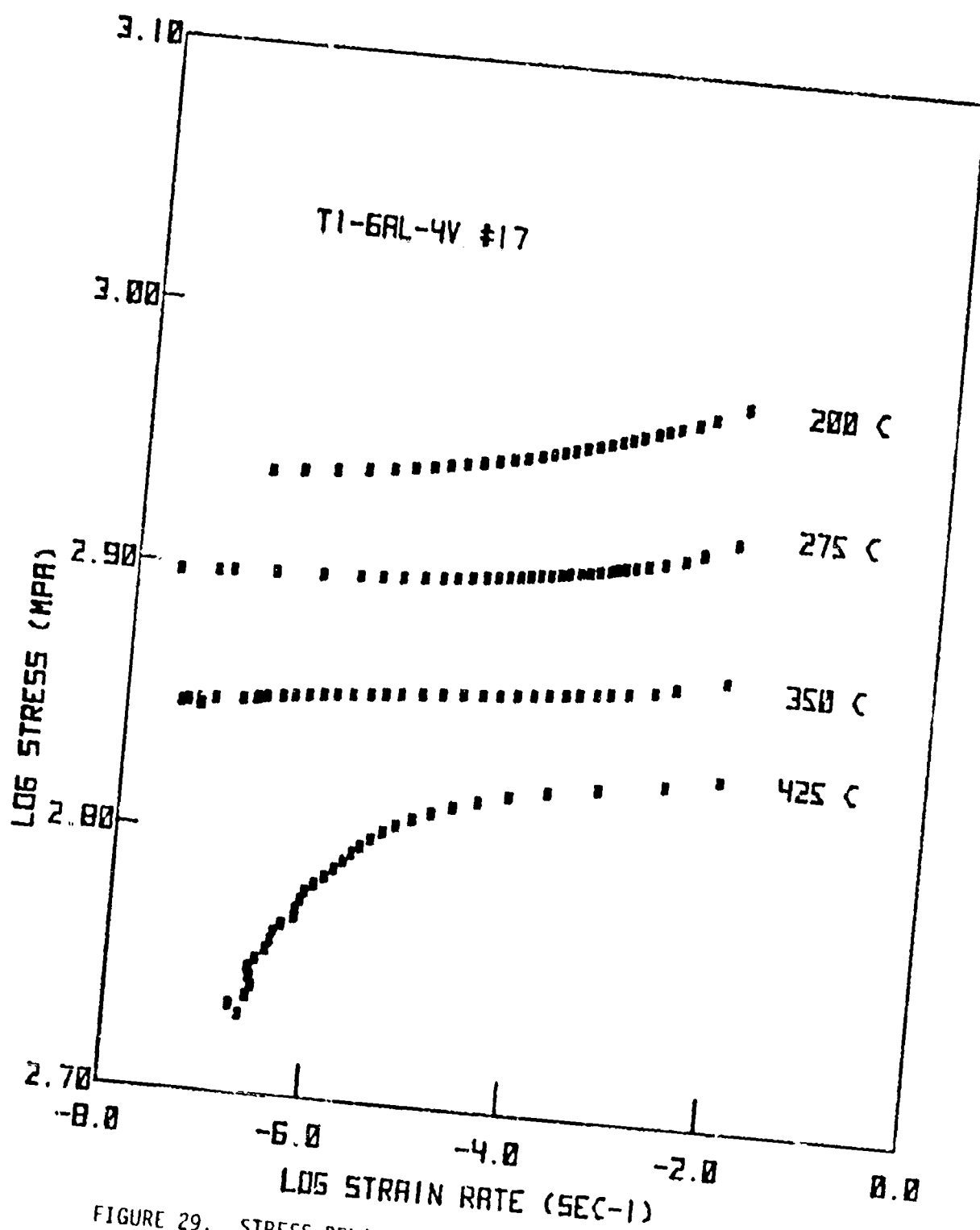


FIGURE 29. STRESS-RELAXATION HARDNESS CURVES vs. TEMPERATURE
(200°C - 425°C) FOR Ti-6Al-4V BAR

Variation with strain - bar. Two load relaxation tests were performed on another specimen, both at 25°C, at true strains of 0.015 and 0.051. The hardness curves are shown in Fig. 30.

At 25°C, Hart's equation Eq. (2-6) relating flow stress to strain rate can be approximated by

$$\sigma = \sigma^* + \sigma_0 \dot{\epsilon}^{1/M}. \quad (6-2)$$

This equation was fit to the two hardness curves in Fig. 30. A value $M=30$ was selected by trial and error, and σ^* and σ_0 were then determined by linear regression. These are shown in Table 13. The value of M should be considered approximate. Its choice affects the absolute values of σ^* and σ_0 but not the change from test to test. It is seen that σ^* increases with strain but σ_0 is almost constant.

TABLE 13. HARDNESS CURVE PARAMETERS
FOR Ti-6Al-4V AT 25°C.

Specimen	Test No.	M	σ^* (MPa)	σ_0 (MPa-sec ^{1/M})
# 2 (Bar)	1	30	683.6	418.3
# 2 (Bar)	2	30	740.5	428.6
#39L (Sheet)	1	30	611.1	490.9

Comparison of load relaxation and constant extension rate tests - sheet. A single load relaxation test was performed on a Ti-6Al-4V sheet specimen at 25°C. The specimen was loaded at an initial strain rate of $4 \times 10^{-3} \text{ sec}^{-1}$ and the relaxation began at a strain of 0.016 and a stress level nearly equal to the yield point stress σ_y . Since the sheet material strain hardens so little, a repeat test on the same specimen is not of interest.

The hardness curve for this test is shown in Fig. 31 along with the fit of Eq. (6-2) for $M=30$. The σ^* and σ_0 values are included in Table 13.

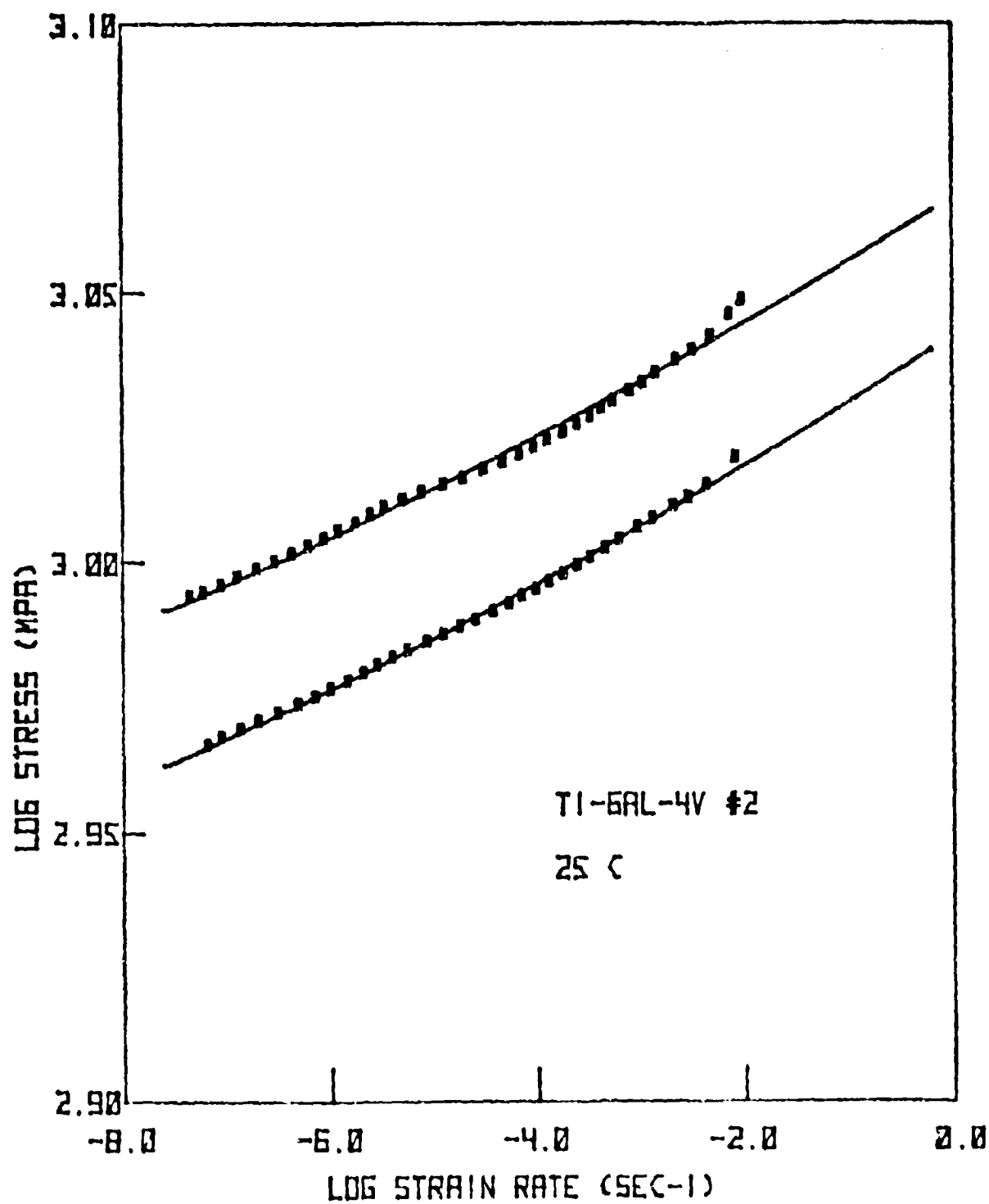


FIGURE 30. STRESS-RELAXATION HARDNESS CURVES WITH HART'S LOW TEMPERATURE EQUATION FIT FOR Ti-6Al-4V BAR AT 25°C

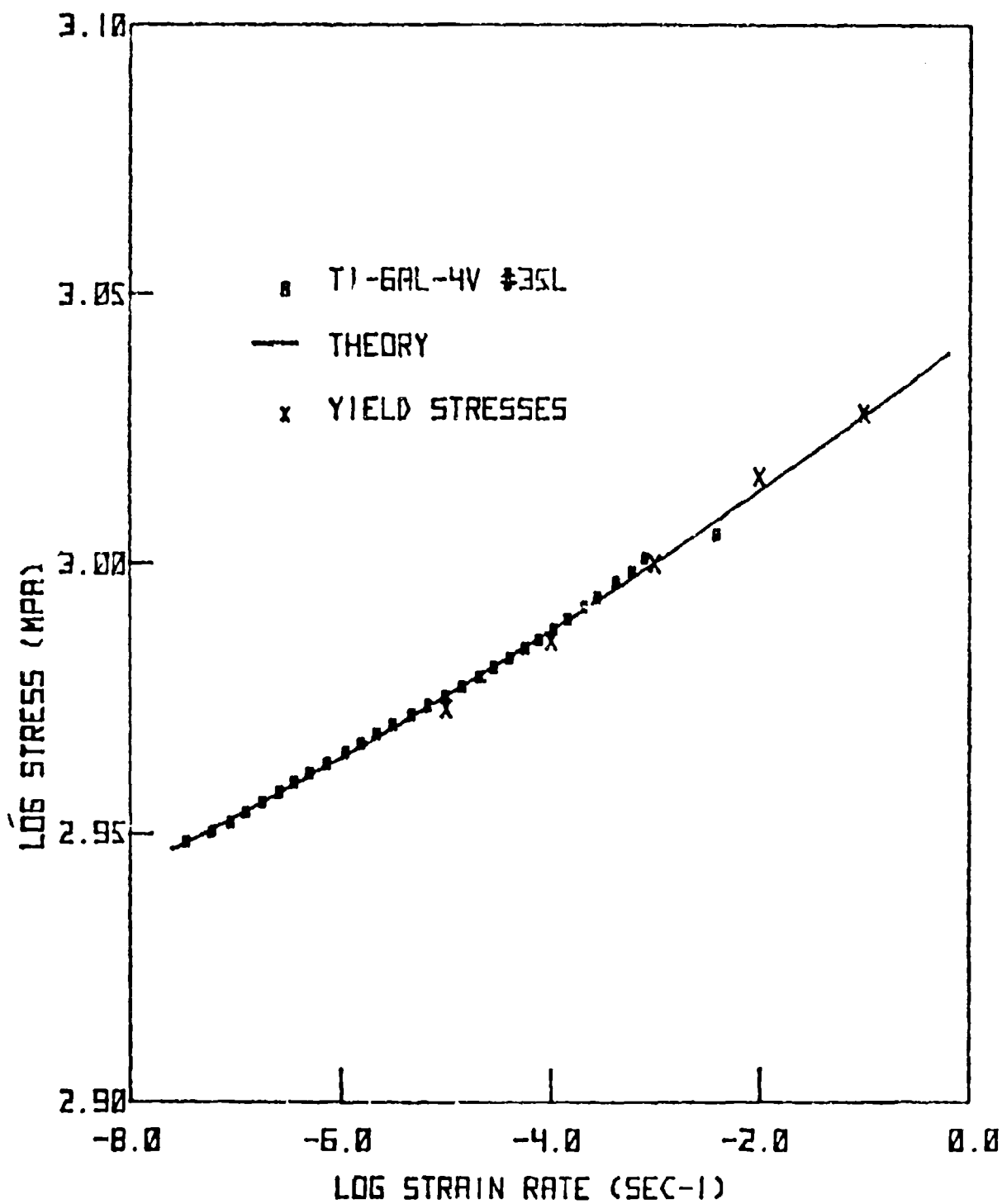


FIGURE 31. STRESS-RELAXATION HARDNESS CURVE WITH HART'S LOW TEMPERATURE EQUATION FIT AND COMPARISON TO RATE DEPENDENT YIELD STRESSES FOR Ti-6Al-4V SHEET AT 25°C

It is seen that σ^* is smaller and σ_0 larger than those for either test on the bar specimen. Thus it is σ_0 rather than σ^* which correlates with relatively high yield point stress of the sheet material.

The dependence of flow stress on strain rate from the load relaxation tests can also be compared to the strain rate dependence determined from the constant extension rate tests. For this comparison, the yield point stresses σ_y from Table 9 were converted to true stresses and plotted vs. initial strain rate in Fig. 31. It is seen that the load relaxation results, including the extrapolation to 10^{-1} sec^{-1} , agree extremely well with the yield point stresses from the constant extension rate tests at all five initial strain rates. It is believed that this close agreement is due to the fact that the strain hardening rate is small and nearly independent of strain rate.

For the Ti-6Al-4V sheet material, it appears that an approximate strain and strain rate dependent constitutive equation can be obtained by combining Eq. (6-2) with the Swift equation. A possible form would be

$$\sigma = \sigma^* \left(1 + \frac{\epsilon}{\epsilon_0}\right)^{0.106} + \sigma_0 \dot{\epsilon}^{1/M} \quad (6-3)$$

where σ^* and σ_0 are taken from Table 13, ϵ_0 from Table 12. The equation would only be valid for strains from 0 to $(0.106 - \epsilon_0)$.

7. COMPARISON OF THEORETICAL AND EXPERIMENTAL FORMING LIMITS

For 2024-O Aluminum at 25°C. Both in-plane and out-of-plane FLD's have been obtained for the 2024-O aluminum at room temperature by ALCOA [4]. The out-of-plane FLD was obtained using a modification of Hecker's [19] method, and the in-plane FLD was based on both standard parallel-sided and notched tensile specimens. For the notched tensile specimens, a special square grid of 100 lines/inch was used to determine the strains. The FLD's are shown in Fig. 32 for two different lots of 2024-O aluminum, the standard Reynolds lot and an ALCOA lot. The ALCOA lot is considerably more formable than the Reynolds lot, and for both lots, the in-plane forming limit is well below the out-of-plane forming limit. Possible reasons for this latter discrepancy have been discussed in Section 3.

The Hill FLC was calculated for the Reynolds lot 2024-O using the average Swift equation parameters from Table 7 and an average $\bar{r} = 0.73$. The FLC is shown in Fig. 33 along with the in-plane and out-of-plane FLD's for the Reynolds lot (converted to true strains) from Fig. 32. The agreement between the FLC and in-plane FLD is very good. This is due in part to the fact that the strain rate sensitivity of 2024-O aluminum at room temperature is very low (Section 5.2) and its neglect by using the Hill theory is a good approximation. It is not surprising that the FLC agrees with the in-plane rather than out-of-plane FLD since the FLC was determined from parameters measured under plane stress conditions. The calculated FLC for 2024-O aluminum at 25°C is discussed in more detail by Nagpal et al. [38].

For 2024-O Aluminum at 163°C. From the Swift equation parameters in Table 8 it can be determined that the calculated Hill FLC for 163°C would fall below that for 25°C. The plane strain intercept for 163°C would be 0.122 (assuming $\bar{r} = 0.73$) vs. 0.155 at 25°C. This is clearly not realistic as we expect considerably more formability at 163°C than at 25°C, so the FLC is not presented. It does illustrate that the increase in formability with temperature would be a strain-rate effect.

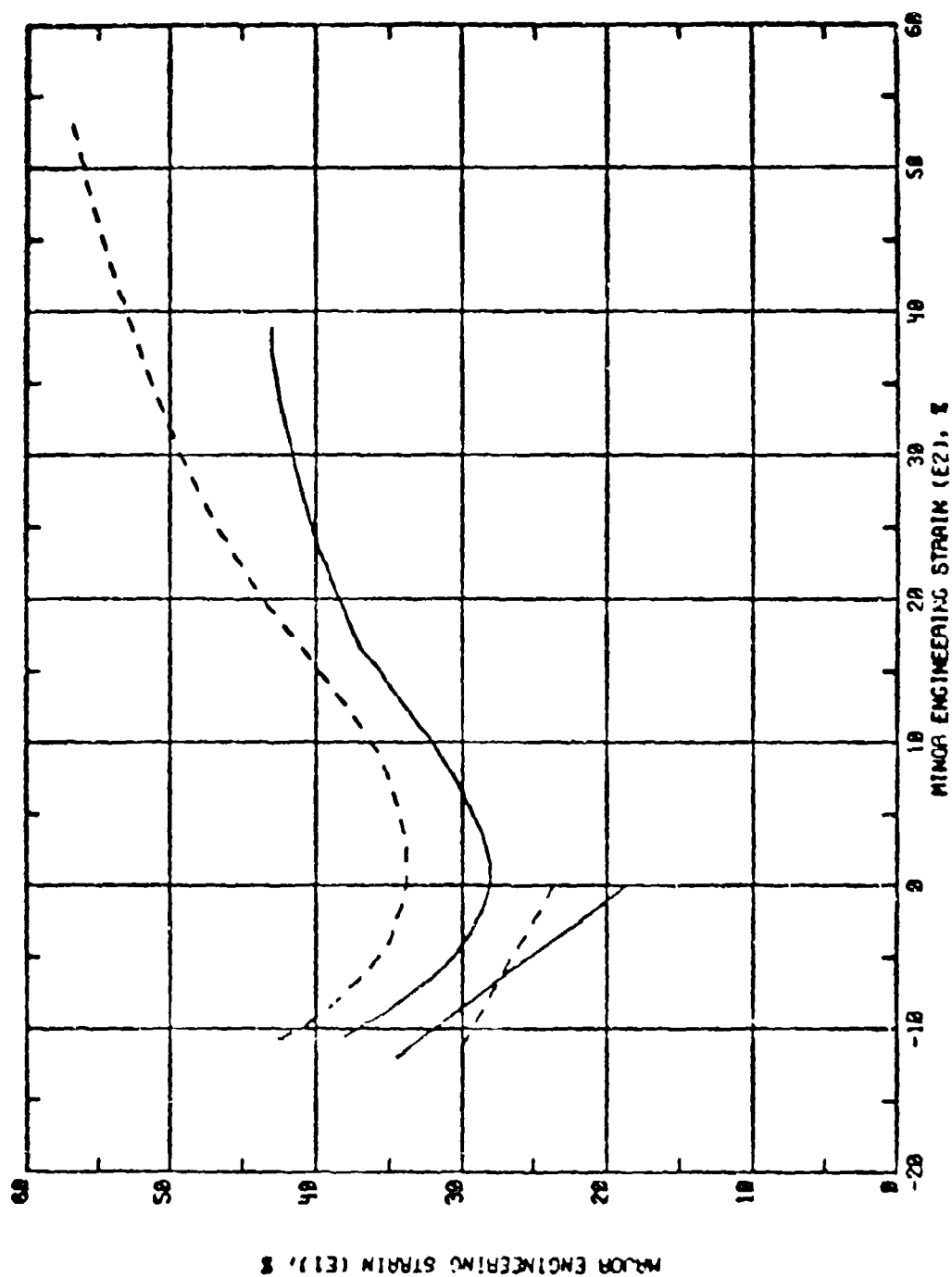


FIGURE 32. IN-PLANE AND OUT-OF-PLANE FLD's FOR 2024-O ALUMINUM AT 25°C
 --- REYNOLDS LOT. --- ALCOA LOT. FROM [4]

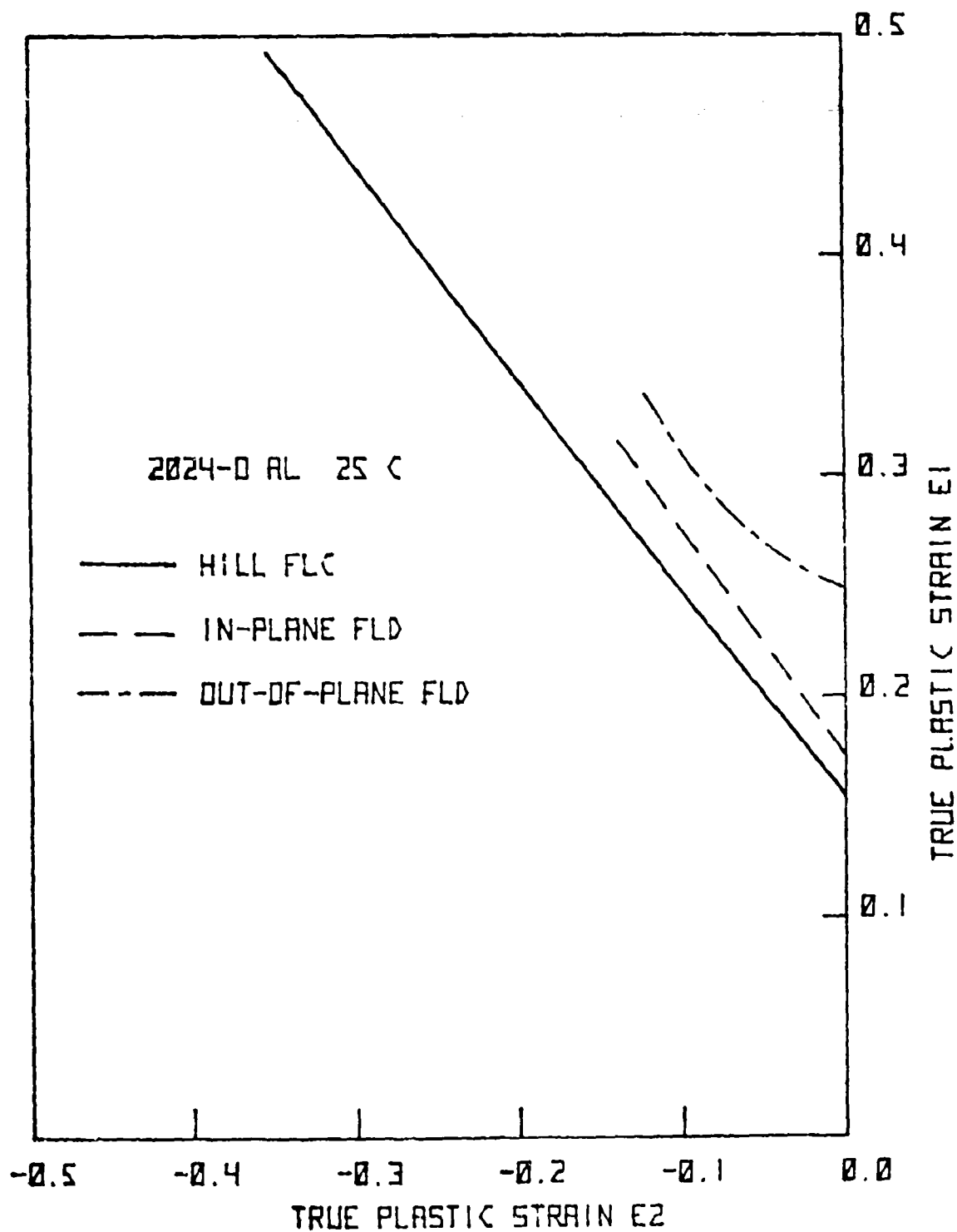


FIGURE 33. THEORETICAL HILL FLC FOR 2024-O ALUMINUM AT 25°C
WITH COMPARISON TO EXPERIMENTAL FLD's

For Ti-6Al-4V. Both in-plane and out-of-plane FLD's were determined for Ti-6Al-4V at 24°C, 538°C (1000°F), and 677°C (1250°F) by the University of Kentucky [4]. The results are shown in Fig. 34. For these tests, the in-plane and out-of-plane FLD's agreed very closely. It is seen that the minimum limit strain at 24°C is about 0.13 and the formability increases with temperature.

If a Hill FLC were calculated based on the Swift equation parameters in Table 12, the overall level would depend upon strain rate. The effective strain rate for the FLD can be estimated from the crosshead speed to be $\geq 10^{-2} \text{ sec}^{-1}$. Using the 10^{-2} sec^{-1} parameters would give a plane strain intercept of approximately 0.02. Again, this indicates that the formability of the Ti-6Al-4V is mainly strain rate dependent, and the Hill FLC will not predict the forming limits.

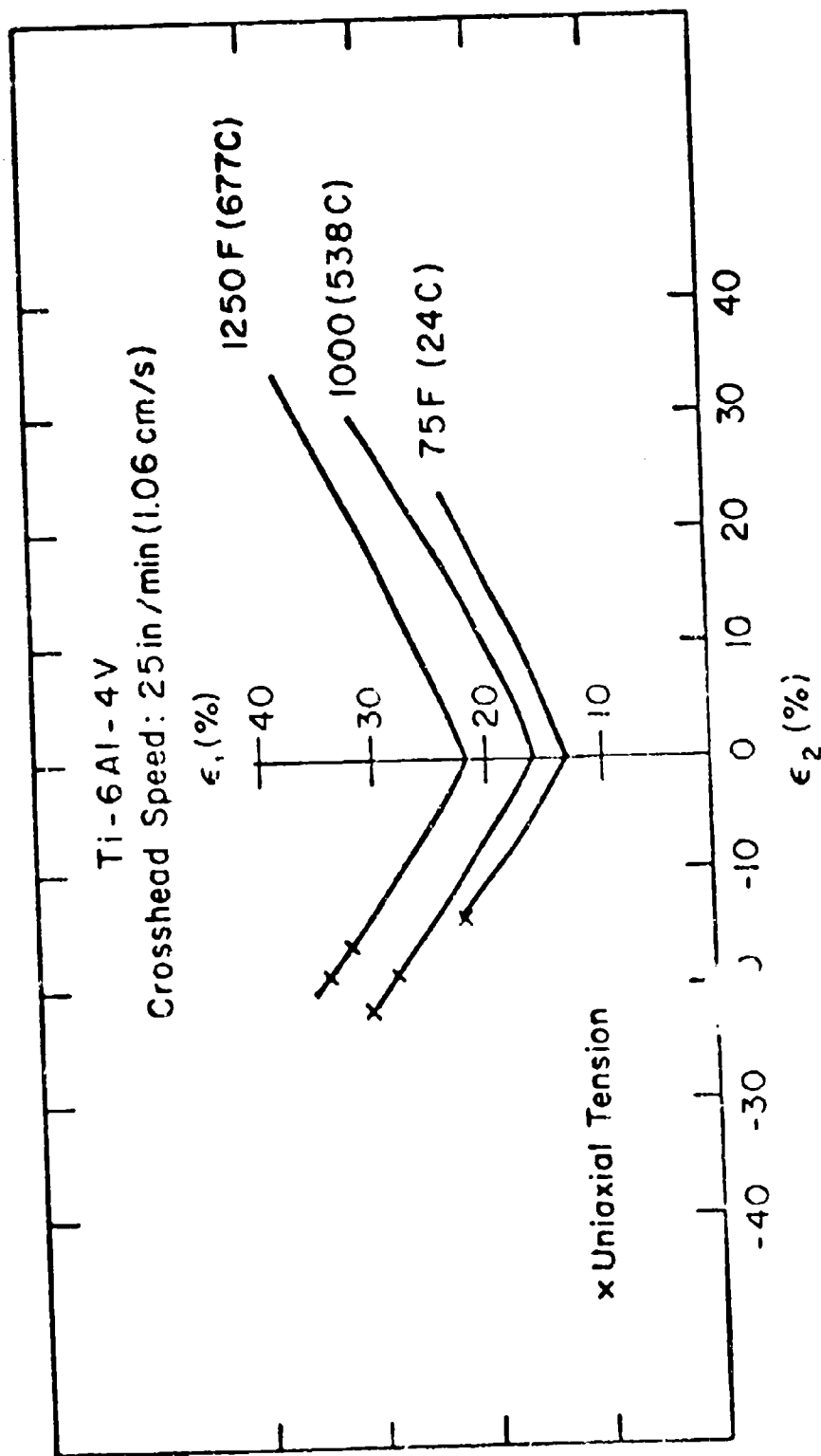


FIGURE 34. EXPERIMENTAL FLD'S FOR Ti-6Al-4V AT 24°C, 538°C, AND 677°C. FROM [4]

8. CONCLUSIONS

1. The results of this program suggest that sheet metal formability can be predicted from theoretical forming limit curves based on constitutive equation parameters determined from uniaxial tension tests. Success of this approach requires careful modeling of strain hardening behavior and the consideration of strain rate sensitivity. Further work to incorporate strain rate effects into calculated FLC's is required.

2. A new method of investigating strain hardening behavior based upon the dependence $\gamma = \gamma(\sigma)$ is proposed. The method assures that the slope of the stress-strain curve, which directly effects formability, will be accurately modelled.

3. Analysis of the stress dependence of the strain hardening coefficient $\gamma(\sigma)$ has shown that the strain hardening behavior of 2024-0 aluminum at 25°C and 163°C and of Ti-6Al-4V at 25°C can be modelled by the Swift equation for large strains ($\epsilon \geq 0.05$ for 2024-0 Al and $\epsilon \geq 0.02$ for Ti-6Al-4V). Excellent agreement is obtained between measured and calculated uniform strains. For 2024-0 Al at 25°C, good agreement is obtained between the extrapolated Swift equation and hydraulic bulge test data to strains of ~ 0.4 .

4. The strain rate dependence $\sigma(\dot{\epsilon})$ from load relaxation tests at 25°C can be modeled by an equation suggested by Hart for low homologous temperatures. For 2024-0 Al at 25°C, the strain rate sensitivity is small enough to be neglected. For Ti-6Al-4V at 25°C, good agreement is obtained for $\sigma(\dot{\epsilon})$ determined from both load relaxation tests and constant extension rate flow stress vs. strain rate.

5. The strain rate dependence of the flow stress $\sigma(\dot{\epsilon})$ at elevated temperatures (to 225°C for 2024-0 Al; to 500°C for Ti-6Al-4V) shows the transition from low temperature to high temperature behavior suggested by Hart. For 2024-0 Al at 163°C (325°F), it appears that the strain rate dependence is effected by grain boundary sliding.

6. The orientation dependence of the flow stress of 2024-0 aluminum sheet at 25°C can be interpreted using Hill's theory of planar anistropy

and measured r -values. The agreement with effective stress-strain determined from the hydraulic bulge test is reasonable.

7. For 2024-0 Al at 25°C, the theoretical FLC based on Hill's theory of localized necking (strain-rate independent) is in good agreement with the experimental in-plane forming limit diagram. However, both are significantly lower than the standard out-of-plane FLD determined by punch-stretch tests.

8. For 2024-0 aluminum at 163°C and Ti-6Al-4V at 25°C, the forming limits calculated using Hill's theory of localized necking would be too small due to the neglect of strain rate dependence. Development of a strain rate dependent model for the calculated FLC is required.

9. REFERENCES

1. J.F. Thomas, Jr., H.L. Gegel, and L.J. Teutonico, "Analytical Simulation of Material Behavior for Sheet Metal Forming," in Proceedings NAMRC-V, Society of Manufacturing Engineers, Dearborn, MI, 1977, pp. 147-151.
2. S.H. Lee and S. Kobayashi, "The Effects of Strain Paths on the Stretching Limit Strains of Sheet Metal with Planar Anisotropy," in Proceedings NAMRC-III, Society of Manufacturing Engineers, Dearborn, MI, 1975, pp. 277-290.
3. R. Hill, "On Discontinuous Plastic States, with Special Reference to Localized Necking in Thin Sheets," *J. Mech. Phys. Solids*, 1952, Vol. 1, pp. 19-30.
4. V. Nagpal and I. Altan, "Mathematical Modeling of Sheet Metal Formability Indices and Sheet Metal Forming Processes," AFML-TR-78-140 U.S. Air Force Materials Laboratory, October, 1978.
5. B. Shabel and V. Nagpal, "Biaxial Stress-Strain Behavior in 2024-0 Sheet," private communication.
6. J.H. Holloman, "Tensile Deformation," *Trans. AIME*, 1945, Vol. 162, pp. 268-290.
7. P. Ludwik, Elemente der Technologischen Mechanik, Julius Springer, Berlin, 1909.
8. H.W. Swift, "Plastic Instability Under Plane Stress," *J. Mech. Phys. Solids*, 1952, Vol. 1, pp. 1-18.
9. E. Voce, "The Relationship Between Stress and Strain for Homogeneous Deformation," *J. Inst. Metals*, 1948, Vol. 74, pp. 537-562.
10. E. Voce, "A Practical Strain Hardening Function," *Metallurgia*, 1955, Vol. 51, pp. 219-226.
11. U.F. Kocks, "Laws for Work-Hardening and Low-Temperature Creep," *ASME J. Eng. Mat. Tech.*, 1976, Vol. 98, pp. 76-85.
12. R.F. Reed-Hill, W.R. Cribb, and S.N. Monteiro, "Concerning the Analysis of Tensile Stress-Strain Data Using $\log d\epsilon/d\epsilon_p$ Versus $\log \sigma$

- Diagrams," Met. Trans., 1973, Vol. 4, pp. 2665-2667.
13. E.W. Hart, "A Phenomenological Theory for Plastic Deformation of Polycrystalline Metals," Acta Met., 1970, Vol. 18, pp. 599-610.
 14. E.W. Hart, C. -Y. Li, H. Yamada, and G.L. Wire, "Phenomenological Theory: A Guide to Constitutive Relations and Fundamental Deformation Properties," in Constitutive Equations in Plasticity, A.S. Argon, Ed., MIT Press, 1975, pp. 149-197.
 15. E.W. Hart, "Constitutive Relations for the Nonelastic Deformation of Metals," ASME J. Eng. Mat. Tech., 1976, Vol. 98, pp. 193-202.
 16. S.P. Keeler, "Determination of Forming Limits in Automotive Stampings," Society of Automotive Engineers, 1965, Paper No. 650535.
 17. G.M. Goodwin, "Application of Strain Analysis to Sheet Metal Forming Problems in the Press Shop," Society of Automotive Engineers, 1968, Paper No. 680093.
 18. M. Azrin and W.A. Backofen, "The Deformation and Failure of a Biaxially Stretched Sheet," Met. Trans., 1970, Vol. 1, pp. 2857-2865.
 19. S.S. Hecker, "A Cup Test for Assessing Stretchability," Metals Eng. Quarterly, 1974, Vol. 14, No. 4, pp. 30-36.
 20. A.K. Ghosh and S.S. Hecker, "Stretching Limits in Sheet Metals: In-Plane vs. Out-of-Plane Deformation," Met. Trans., 1974, Vol. 5, pp. 2161-2164.
 21. A.K. Ghosh "Plastic Flow Properties in Relation to Localized Necking in Sheets," in Mechanics of Sheet Metal Forming, ed. by D.P. Koistinen and N. M. Wang, Plenum Press, 1978, pp. 287-312.
 22. Z. Marciniak and K. Kuczynski, "Limit Strains in the Processes of Stretch-Forming Sheet Metal," Int. J. Mech. Sci., 1967, Vol. 9, pp. 609-620.
 23. J.W. Hutchinson and K.W. Neale, "Sheet Necking II. Time - Independent Behavior," and "Sheet Necking - III. Strain-Rate Effects," in Mechanics of Sheet Metal Forming, ed. by D.P. Koistinen and N.-M. Wang, Plenum Press, 1978, pp. 127-153, 269-285.

24. S. Stören and J.R. Rice, "Localized Necking in Thin Sheets," J. Mech. Phys. Solids, 1975, Vol. 23, pp. 421-441.
25. R. Sowerby and J.L. Duncan, "Failure in Sheet Metal in Biaxial Tension," Int. J. Mech. Sci., 1971, Vol. 13, pp. 217-229.
26. Z. Marciniak, K. Kuczynski, and T. Pokora, "Influence of the Plastic Properties of a Material on the Forming Limit Diagram for Sheet Metal in Tension," Int. J. Mech. Sci., 1973, Vol. 15, pp. 789-805.
27. R. Hill, Mathematical Theory of Plasticity, Oxford University Press, 1967, pp. 317-340.
28. L. Teutonico, Private Communication.
29. J.F. Thomas, Jr., "Determination of Constitutive Equations for Titanium Alloys Applicable to Sheet Metal Formability," Report WSU-550F, Wright State University, 1978.
30. E.O. Hall, Yield Point Phenomena in Metals and Alloys, Plenum Press, 1970, pp. 171-200.
31. R. Pascual, "Acoustic Emission and Dislocation Multiplication During Serrated Flow in Aluminum Alloys," Scripta Met., 1974, Vol. 8, pp. 1461-1466.
32. A.K. Ghosh, "A Numerical Analysis of the Tensile Test for Sheet Metals," Met. Trans., 1976, Vol. 8A, pp. 1221-1232.
33. K. Yoshida, K. Yoshii, H. Komorida, M. Usuda, and H. Watanabe, "Mechanical Significance of γ Value in Sheet Metal and Workhardening Exponent $[n]$ Under Equibiaxial Tension, and their Applications to the Assessment of Formability," Sci. Papers I.C.P.R., 1970, Vol. 64, pp. 24-37.
34. D.J. Lloyd, B.D. McLaughlan, and H. Sang, "The Stress-Strain Behavior of Aluminum Alloys at Large Strains," Scripta Met., 1977, Vol. 11, pp. 297-300.
35. E.W. Hart, "Theory of the Tensile Test," Acta Met., 1967, Vol. 15, pp. 351-355.

36. D. A. Woodford, "Load Relaxation Testing of a Superplastic Superalloy," Met. Trans., 1976, Vol. 7A, pp. 1244-1246.
37. E.W. Hart, "A Theory of Flow for Polycrystals," Acta Met., 1967, Vol. 15, pp. 1545-1549.
38. V. Nagpal, B.S. Shabel, J.F. Thomas, Jr., and H.L. Gege1 "Formability Models for 2024-O Aluminum Sheet Metal," to be published in Proceedings NAMRC-VII, Society of Manufacturing Engineers, 1979.

8. APPENDIX A: SUMMARY OF SOME ANISOTROPIC PLASTICITY RELATIONSHIPS

Hill [27] has extended the Von Mises yield function to account for plastic anisotropy. The resulting yield function $f(\sigma_{ij})$ and effective stress $\bar{\sigma}$ are defined by

$$\begin{aligned} 2 f(\sigma_{ij}) &= F(\sigma_y - \sigma_z)^2 + G(\sigma_z - \sigma_x)^2 + H(\sigma_x - \sigma_y)^2 \\ &\quad + 2 L \tau_{yz}^2 + 2 M \tau_{zx}^2 + 2 N \tau_{xy}^2 \\ &= (2/3)(F + G + H) \bar{\sigma}^2 \end{aligned} \quad (A1)$$

where F, G, H, L, M, N are the anisotropy parameters. For the case of planar stress with $\sigma_z = \tau_{yz} = 0$, Eq. (A1) reduces to

$$2f(\sigma_{ij}) = (G + H) \sigma_x^2 - 2H \sigma_x \sigma_y + (F + H) \sigma_y^2 + 2N \tau_{xy}^2 = 2k_A \bar{\sigma}^2 \quad (A2)$$

where $k_A = (F + G + H)/3$. For application to the deformation of a thin sheet, the \hat{x} direction is taken parallel to the rolling direction.

Lee and Kobayashi [2] have presented the corresponding expressions for an applied stress system defined with respect to orthogonal axes (1,2) which are rotated by an angle θ with respect to the axes (x,y). For principal stresses ($\tau_{12} = 0$), the result is

$$2f(\sigma_{ij}) = A\sigma_1^2 - 2B\sigma_1\sigma_2 + C\sigma_2^2 = 2K_A\bar{\sigma}^2 \quad (A3)$$

where $A = F\sin^2\theta + G\cos^2\theta + H - \delta\sin^2\theta\cos^2\theta$

$$B = H - \delta\sin^2\theta\cos^2\theta$$

$$C = G\sin^2\theta + F\cos^2\theta + H - \delta\sin^2\theta\cos^2\theta$$

$$\delta = F + G + 4H - 2N.$$

The normal plastic strain increments are derived from the yield function according to

$$d\epsilon_1 = \frac{d\bar{\epsilon}}{2k_A\bar{\sigma}} \frac{\partial f}{\partial \sigma_1}, \quad (A4)$$

$$d\epsilon_2 = \frac{d\bar{\epsilon}}{2k_A\bar{\sigma}} \frac{\partial f}{\partial \sigma_2}. \quad (A5)$$

The normal strain increment $d\epsilon_3$ can be obtained from the condition for constant volume

$$d\epsilon_1 + d\epsilon_2 + d\epsilon_3 = 0. \quad (A6)$$

It is important to note that the shear strain increment $d\gamma_{12}$ is not necessarily zero even for a stress system with $\tau_{12} = 0$. In fact, the principal axes of stress and strain will only coincide if one of the principal stress axes lies along the rolling direction [2].

In the following we denote the ratio of principal stresses $\sigma_2/\sigma_1 = \alpha$, and the corresponding ratio of plastic strain increments $d\epsilon_2/d\epsilon_1 = \beta$. For the case of proportional straining, β is a constant, and $\beta = \epsilon_2/\epsilon_1$. Eqs. (A4) and (A5) can be used to relate α and β ,

$$\beta = (C\alpha - B)/(A - B\alpha), \quad (A7)$$

and inverting,

$$\alpha = (A\beta + B)/(B\beta + C). \quad (A8)$$

We also denote the ratio of plastic strain increments $d\epsilon_2/d\epsilon_3 = r$. Eqs. (A6) and (A7) can be used to relate r to α and β ,

$$r = -\beta/(1+\beta) = (B-C\alpha)/[A-B + (C-B)\alpha]. \quad (A9)$$

Thus the r -value measured in a tensile test ($\alpha = 0$) for a specimen cut from a sheet at an angle θ to the rolling direction is given by

$$r_\theta(\alpha=0) = B/(A-B). \quad (A10)$$

For the usual case of specimens cut at 0° , 90° , and 45° to the rolling direction, Eq. (A10) gives the relations between the measured r -values and the anisotropy parameters

$$r_0 = \frac{H}{G}, \quad r_{90} = \frac{H}{F}, \quad r_{45} = \frac{N}{F+G} - \frac{1}{2}, \quad (A11)$$

or, inverting,

$$\frac{G}{H} = \frac{1}{r_0}, \quad \frac{F}{H} = \frac{1}{r_{90}}, \quad \frac{N}{H} = \left[\frac{1}{r_0} + \frac{1}{r_{90}} \right] \left[r_{45} + \frac{1}{2} \right]. \quad (A12)$$

It is now possible using Eqs. (A3) and (A12) to write down the relations between the effective stress $\bar{\sigma}$ and the measured stress for certain simple test configurations in terms of the measured r -values. For a uniaxial tensile

test ($\sigma_1 = \sigma_T$, $\sigma_2 = 0$) with a specimen cut at an angle $\theta = 0^\circ$, 90° , or 45° to the rolling direction we have

$$\theta = 0^\circ: \quad \frac{\bar{\sigma}}{\sigma_T} = \left[\frac{3(r_{90} + r_0 r_{90})}{2(r_0 + r_{90} + r_0 r_{90})} \right]^{1/2}, \quad (A13)$$

$$\theta = 90^\circ: \quad \frac{\bar{\sigma}}{\sigma_T} = \left[\frac{3(r_0 + r_0 r_{90})}{2(r_0 + r_{90} + r_0 r_{90})} \right]^{1/2}, \quad (A14)$$

$$\theta = 45^\circ: \quad \frac{\bar{\sigma}}{\sigma_T} = \left[\frac{3(r_0 + r_{90})(r_0 + 1)}{4(r_0 + r_{90} + r_0 r_{90})} \right]^{1/2}. \quad (A15)$$

For a hydraulic bulge test, assuming balanced biaxial stress at the pole ($\sigma_1 = \sigma_2 = \sigma_B$),

$$\frac{\bar{\sigma}}{\sigma_B} = \left[\frac{3(r_0 + r_{90})}{2(r_0 + r_{90} + r_0 r_{90})} \right]^{1/2}. \quad (A16)$$

Also, using Eqs. (A4) or (A5), the relation between the effective strain increment $d\bar{\epsilon}$ and the measured strain increment can be obtained. For the tensile test,

$$d\bar{\epsilon}/d\epsilon_1 = (\bar{\sigma}/\sigma_T)^{-1}, \quad (A17)$$

and for the bulge test,

$$d\bar{\epsilon}/d\epsilon_3 = (\bar{\sigma}/\sigma_B)^{-1}. \quad (A18)$$

Thus the inverse of the factors in Eqs. (A13) to (A16) relate effective and measured strain increments.

Finally, we consider the special case of normal anisotropy, i.e., isotropy within the plane such that r_θ ($\theta = 0$) is independent of θ . From Eq. (A12) the isotropy conditions are

$$G/H = F/H = N/H - 2 = 1/r, \quad (A19)$$

and the parameters A, B, C in Eq. (A3) become independent of θ . By choosing $H = r/(1+r)$, Eq. (A3) becomes

$$2f(\sigma_{ij}) = \sigma_1^2 - \frac{2r}{1+r} \sigma_1 \sigma_2 + \sigma_2^2 = 2k_1 \bar{\sigma}^2 \quad (A20)$$

where $k_1 = (2+r)/3(1+r)$. Also, k_1 replaces k_A in Eqs. (A4) and (A5). For normal anisotropy, the ratio of the effective stress to the uniaxial tension

yield stress is

$$\frac{\bar{\sigma}}{\sigma_T} = \left[\frac{1}{2k_1} \right]^{1/2} = \left[\frac{3(1+r)}{2(2+r)} \right]^{1/2}. \quad (A21)$$

Thus, $\bar{\sigma}$ can be thought of as the uniaxial tension yield stress for an isotropic specimen ($r = 1$). For the hydraulic bulge test, Eq. (A16) or Eq. (A20) gives

$$\frac{\bar{\sigma}}{\sigma_B} = \left[\frac{3}{2+r} \right]^{1/2}. \quad (A22)$$

Eqs. (A21) and (A22) combine to give the familiar result

$$\frac{\sigma_B}{\sigma_T} = \left[\frac{1+r}{2} \right]^{1/2}. \quad (A23)$$

In some treatments, Eq. (A20) is written in the slightly different form

$$\sigma_1^2 - \frac{2r}{1+r} \sigma_1 \sigma_2 + \sigma_2^2 = \lambda^2. \quad (A24)$$

In this case, λ is simply a tensile yield stress and differs from the effective stress $\bar{\sigma}$ defined here by the factor $(2k_1)^{1/2}$.

11. APPENDIX B. AUTOMATIC DATA ACQUISITION

SYSTEM CONTROL PROGRAMS

```

0: "DVM RUN":
1: "-----":
2: dim I$(256),
  S$(300), D$(3000)
3: dim C$(50),
  J$(32)
4: dim Z(5)
5: "PCD,; ISPO">
  C$
6: 0+P+r13+r14
7: 1+r10+r11
8: cll 'init'
9: oni 7, "CSI0"
10: wrt "dvm",
  "F1R3T2M3H000000"
11: fmt 8, "-----"
  "-----"
12: "mloop":sps
  5;wrt 16.8
13: asb "IDENT"
14: sps 2;wrt
  16.8;prt "Settings:"
15: asb "SETTING
  S"
16: wrt 16.8
17: dsp "Hit
  continue when
  ready to start."
18: sto
19: -2+T
20: eir 7;wrt
  "clk", "P001E1SR"
21: "ptest":eir
  7
22: if r17#0;
  sto "clock"
23: if r13<1e6;
  sto "pwait"
24: asb "print"
25: "pwait":if
  r17#0;sto "clock"
26: if D#1;sto
  "ptest"
27: 1e6+r13
28: if P#1;sto
  "ptest"
29: beep
30: ent "Print
  out all data?",
  J$
31: if cap(J$)="
  Y";asb "rtall"
32: "mtape":beep
33: ent "Store
  on tape?", J$
34: if cap(J$)#"
  Y";sto "mstop"
35: enr "track
  #", Y
36: enr "file
  #", X
37: trk Y;fdf X
38: idf Z(1),
  Z(2), Z(3), Z(4),
  Z(5)
39: if Z(2)#0;
  ent "Overwrite
  file?", J$
40: if Z(2)#0;
  if cap(J$)#"Y";
  sto "mtape"
41: if Z(4)<3600
  ;beep;ent "File
  too small", J$;
  sto "mtape"
42: rcf X, I$, S$,
  D$
43: prt "file
  stored"
44: "mstop":prt
  "Done";sps 5;
  sto
45: sto "mloop"
46: "clock":r17+
  X;0+r17
47: wrt "clk",
  "T100E1DR"
48: fmt "P", f3.0
  , "E", f1.0, "SR"
49: wrt "clk",
  r16, X
50: eir 7
51: sto "ptest"
52: "CSI0":
53: T+1+T
54: fmt fired
  "dvm", A
55: r7+0
56: "CSI":
57: if r2>=r5;
  if r1<=0;sto
  "csifin"
58: if r2<=r4;
  sto "csiscn"
59: if r1>0;r1-
  1+r1;r3+r2;sto
  "CSI"
60: r2+r4+r3
61: "csinew":
62: if r4>r5;
  sto "csifin"
63: if S$(r4,
  r4)="i";sto ",,"
64: r4+1+r4;sto
  "csinew"
65: "csiscn":
66: pos(C$, S$(r2
  , r2))+r6;r2+
  1+r2
67: if r6>0;sto
  "csiex"
68: prt "CSI
  ERROR";dsp "ERR
  OR!"
69: prt "r1-r6
  =:", r1, r2, r3,
  r4, r5, r6
70: "csifin":1+0
  ;ret
71: "csiex":
72: jmp r6
73: sto "R"
74: sto "C"
75: sto "D"
76: sto ",,"
77: sto "i"
78: sto "space"
79: sto "I"
80: sto "S"
81: sto "P"
82: sto "O"
83: "R":
84: asb "NUM"
85: X-1+r1
86: r2+r3
87: sto "CSI"
88: "C":
89: asb "NUM"
90: cll 'scn1' (X
  )
91: X+r7
92: 1+r7/100+Y
93: Y*1e62+Y
94: fts (Y)+D$(r
  10, r10+3)
95: r10+4+r10
96: sto "CSI"
97: "D":
98: fmt "Channel
  (", f2.0, ") =
  ", f8.5
99: wrt 0, C, A
100: sto "CSI"

```

```

101: "":iret
102: "":eto
"CSI"
103: "space":eto
"CSI"
104: "I":
105: red "clk",U
106: if r14=0;-
1→U;1→r14
107: esb "NUM"
108: X*1e3+r8+r1
3
109: int(log(r8)
)→X
110: r8/10↑X+r8
111: r8*100+r8;
X-2→X
112: fmt "P",
f3.0,"E",f1.0,
"SR"
113: r8+r16;X+r1
7
114: 10*r8+X+Y;
1+Y/10000→Y
115: Y*1e61→Y
116: fts (Y)→D#[
r10,r10+3]
117: fts (U+1)→D
#[r10+4,r10+7]
118: fts (T)→D#[
r10+8,r10+11]
119: r10+12→r10
120: 0→T
121: iret
122: "S":
123: fts (A)→D#[
r10,r10+3]
124: r10+4→r10
125: eto "CSI"
126: "P":
127: fts (1e63)→
D#[r10,r10+3]
128: r10+4→r10
129: eto "CSI"
130: "0":
131: fts (2e63)→
D#[r10,r10+3]
132: r10+4→r10
133: eto "CSI"
134: "NUM":
135: if S#[r2,
r2]#"(";eto
"numerr"
136: r2+1→r2
137: sfa 14;val(
S#[r2,r4]→X
138: for J=r2
to r4

```

```

139: if S#[J,
J]=")";eto "num
ret"
140: next J
141: "numerr":
142: prt "num
error!";dsp
"ERROR!"
143: prt "r1-
r6",r1,r2,r3,
r4,r5,r6
144: 1→D
145: "numret":
146: J+1→r2
147: ret
148: "SETTINGS":
149: " "→S#
150: prt
151: 0→r1→r4→r6→
D→X
152: 1→r2→r3→r5
153: ent "Enter
Setting Command
s:",S#[r5]
154: prt S#
155: eto +2
156: "setloop":e
no "line =",
S#[r5]
157: if S#[r5,
r5]="$";spc ;
prt "len S#=",
r5;eto "setend"
158: len(S#)+
1→r5
159: ";"→S#[r5,
r5];r5+1→r5
160: eto "setloo
p"
161: "setend":sp
c ;prt "S#",S#;
spc 2;ret
162: "init":
163: if p0=0;
rem 7;clr 7
164: fmt 9,f;
dev "clk",710→p
8,"ctr",725→p9,
"dm",722→p10,
"ptr",715→p11
165: dev "scn",
709→p12,"scn1",
710→p13,"scn2",
711→p14,"scn3",
712→p15
166: dev "svm",
724→p16;8→p7

```

```

167: wtb p07;
rds(7,p3,p4,
p5)→p6;r0+2↑(p7
-8)bit(2,p5)→r0
;1+p7→p7
168: if p7<17;
eto -1
169: wtb "ptr.9"
;27,69
170: ret
171: "scn1":
172: fmt f3.0;
wrt "scn",p1
173: ret
174: "print":
175: if r11+3>=r
10;1→P;ret
176: stf(D#[r11,
r11+3])→Y
177: r11+4→r11
178: int(log(Y))
→X
179: Y/10↑X→Y
180: if X=63;
eto "pfls"
181: if r12=0;
ret
182: if X<60;
fxd 6;prt Y*
10↑X;ret
183: if X=61;
eto "int"
184: if X=62;
eto "chn1"
185: ret
186: "int":
187: fxd 0
188: prt "Clock
ticks=",stf(D#[
r11,r11+3])
189: prt "#Inter
rupts=",stf(D#[
r11+4,r11+7])
190: r11+8→r11
191: Y-1→Y
192: 1000*Y→Y
193: int(Y)→X
194: (Y-X)*10→Y
195: X*10↑Y→Y
196: flt 3;spc 2
197: prt "Int.
=",Y
198: spc
199: ret
200: "chn1":
201: fxd 0
202: Y-1→Y
203: Y*100→Y

```



```

204: spc 2;prt
    "Channel #",Y
205: ret
206: "pflg":
207: prt "print"
208: if Y=1;prt
    "on";1→r12
209: if Y=2;prt
    "off";0→r12
210: ret
211: "IDENT":
212: ""→I$;" "→J$
    ;1→X
213: ent "Enter
    run I.D.";J$
214: prt "Run
    I.D."
215: sto +4
216: "idloop":
217: ""→J$
218: ent "line:"
    ,J$
219: if len(J$)>
    16;dsp "line
    too long";beep;
    wait 3000;sto -
    2
220: prt J$
221: if len(J$)>
    0;if len(J$)<16
    ;J$&" "→J$;jmp
    0
222: J$[1,16]→I$
    [X];len(I$)+1→X
223: if len(J$)>
    0;sto "idloop"
224: wrt 16.8
225: ret
226: "prtall":
227: wrt 16.8;
    prt "Data Set:"
    ;spc 3
228: 0→P;1→r11
229: if P#1;1→r1
    2;asb "print"
230: if P#1;sto
    -1
231: ret

```

```

0: "DVM DATA":
1: "-----":
2: dim I$(256),
   S$(300),D$(3000)
3: dim N$(50)
4: "RCD,; ISPO">
   N$
5: dim C$(2,2360)
6: dim J$(5),
   Z(5)
7: dim T(5),P(5)
   ,Q(5)
8: spc 3
9: prt "*****
*****"
10: prt "DM2"

11: prt "*****
*****"
12: spc 2
13: 1→A→8
14: 0→r1→r4→r6→r
   7→r13
15: 1→r2→r3
16: 0→C
17: 1→Q(1)→Q(2)
18: enp "Tape
   track #",T
19: enp "Data
   File #",F
20: trk T;ldf F,
   I$,S$,D$
21: len(S$)→r5
22: enp "Load
   Channel :",P(1)
23: enp "Other
   channel :",P(2)
24: prt "-----
-----"
25: prt "File
   ID"
26: prt "-----
-----"
27: spc ;prt "-----
-----"
28: prt I$
29: prt "-----
-----";spc
   2
30: ""→C$(1)→C$(
   2)
31: 0→T(1)→T(2)→
   T(3)→T(4)→T(5)
32: prt "CSI"

```

```

33: "CSI":
34: if r2>=r5;
   if r1<=0;eto
   "csifin"
35: if r2<=r4;
   eto "csiscn"
36: if r1>0;r1-
   1→r1;r3→r2;eto
   "CSI"
37: r2→r4→r3
38: "csinew":
39: if r4>r5;
   eto "csifin"
40: if S$(r4,
   r4)=";";eto ","
41: r4+1→r4;eto
   "csinew"
42: "csiscn":
43: pos(N$,S$(r2
   ,r2))→r6;r2+
   1→r2
44: if r6>0;eto
   "csiex"
45: prt "CSI
   ERROR";dsp "ERR
   OR!"
46: prt "r1-r6
   =:",r1,r2,r3,
   r4,r5,r6
47: eto "csifin"
48: "csiex":
49: jmp r6
50: eto "R"
51: eto "C"
52: eto "D"
53: eto ","
54: eto ";"
55: eto "space"
56: eto "I"
57: eto "S"
58: eto "P"
59: eto "O"
60: "NUM":
61: if S$(r2,
   r2)="#"(;"eto
   "numerr"
62: r2+1→r2
63: sfs 14;val(S
   $(r2,r4))→X
64: for J=r2 to
   r4
65: if S$(J,J)="
   ";eto "numret"
66: next J
67: "numerr":

```

```

68: prt "num
   error!";dsp
   "ERROR!"
69: prt "r1-r6",
   r1,r2,r3,r4,r5,
   r6
70: "numret":
71: J+1→r2;ret
72: "DATA":
73: if A>len(D$)
   ;eto "outerr"
74: stf(D$(A,A+
   3))→D
75: A+4→A
76: if D=0;0→Z;
   eto +2
77: int(log(abs(
   D)))→Z
78: D/10↑Z→Y
79: ret
80: "R":
81: asb "NUM"
82: X-1→r1
83: r2→r3
84: eto "CSI"
85: "C":
86: asb "NUM"
87: 0→L
88: if X=P(1);
   1→L
89: if X=P(2);
   2→L
90: asb "DATA"
91: if Z#62;eto
   "Cerr"
92: Y-1→Y
93: Y*100→Y→C
94: if C#X;eto
   "Cerr"
95: eto "CSI"
96: "Cerr":
97: prt "Channel
   Error"
98: prt "Command
   =",X
99: prt "Data
   =",Y
100: eto "CSI"
101: "I":
102: asb "DATA"
103: if Z#61;
   eto "Ierr"
104: Y-1→Y
105: Y*1000→Y
106: int(Y)→Z
107: (Y-Z)*10→Y

```

```

108: Z=10*Y+Y
109: Y/1e6+Y
110: #zb "NUM"
111: X/1e3+X
112: Y+r12
113: if X#Y;eto
    "terr"
114: #zb "DATA"
115: D+r8
116: #zb "DATA"
117: D+r9
118: if r8=r9;
    eto "intgood"
119: "terr":
120: fxd 2
121: prt "Timing
    error!"
122: prt "clock
    ticks =",r8
123: prt "interr
    upts =",r9
124: prt "Interv
    al #",r10
125: prt "start
    time:",T[4]
126: prt "End
    time:",T[1]
127: prt "# time
    increments:",
    T[3]
128: prt "new
    int.(msec) =",
    r12*1e3
129: prt "**
    Note!"prt "Tim
    ing based on #
    of interrupts"
130: "intgood":
131: prt "-----
    -----"
132: prt "interv
    al",r12;r12+Y
133: prt "-----
    -----"
134: spc
135: 0+r11
136: T[4]+(r9-
    2)*T[2]+.15+T[1]
137: if T[5]=0;
    1+T[5];0+T[1]
138: T[1]+T[4]
139: Y+T[2]
140: 0+T[3]
141: r10+1+r10
142: eto "CSI"
143: "S":
144: if r13=0;
    1+r13;0+T[1]

```

```

145: #zb "DATA"
146: if Z>60;
    eto "Serr"
147: if L=0;eto
    "Dprint"
148: fts (T[1])+
    C*[L,Q[L]]
149: fts (D)+C*[
    L,Q[L]+4]
150: Q[L]+8+Q[L]
151: eto "Dprint"
    "
152: "Serr":
153: prt "Data
    Exponent"
154: prt ">60"
155: prt "Serr"
156: stop
157: eto "CSI"
158: "Dprint":
159: if r11=0;
    1+r11;prt "C
    Time Data"
160: fnt 8,f1.0,
    e9.2,f6.3
161: wrt 16.8,C,
    T[1],D
162: eto "CSI"
163: ",":
164: T[1]+T[2]+T
    [1]
165: T[3]+1+T[3]
166: eto "CSI"
167: "D":
168: "I":
169: "space":
170: "P":
171: "O":
172: eto "CSI"
173: "csifin":
174: beepient
    "Store on tape?
    ",J$
175: if cap(J$)#
    "Y";eto "nstop"
176: end "Track
    #",Y
177: end "File
    #",X
178: trk Y;fdf X
179: idf Z[1],
    Z[2],Z[3],Z[4],
    Z[5]
180: if Z[2]#0;
    ent "Overwrite
    file?"J$

```

```

181: if Z[3]#0;
    if cap(J$)#"Y";
    eto "csifin"
182: if Z[4]<500
    0;beepient "Fil
    e too small".
    J$;eto "csifin"
183: rcf X,C$
184: prt "file
    stored"
185: "nstop":prt
    "Done"ispc 3;
    stop
+2734

```